

Influence of natural convection on melting of phase change materials

Von der Fakultät Energie-, Verfahrens- und Biotechnik der Universität Stuttgart
zur Erlangung der Würde eines Doktor-Ingenieurs (Dr.-Ing.) genehmigte
Abhandlung

Vorgelegt von

Julian Vogel

aus Karlsruhe

Hauptberichter:

Prof. Dr. André Thess

Mitberichter:

Prof. Dr. Oleg Zikanov

Tag der mündlichen Prüfung:

11. Dezember 2018

Institut für Gebäudeenergetik, Thermotechnik und Energiespeicherung der
Universität Stuttgart

2019

Eidesstattliche Erklärung

Ich versichere, dass ich die vorliegende Arbeit selbständig verfasst und keine anderen als die angegebenen Quellen und Hilfsmittel benutzt habe; aus fremden Quellen entnommene Passagen und Gedanken sind als solche kenntlich gemacht.

Declaration of Authorship

I hereby certify that this dissertation is entirely my own work except where otherwise indicated. Passages and ideas from other sources have been clearly indicated.

Kurzfassung

Latentwärmespeicher können in Zukunft zum Ausgleich der Diskrepanz zwischen der Versorgung und dem Bedarf an erneuerbaren Energien beitragen. Mangels geeigneter Validierungsexperimente sind die für die Speicherauslegung benötigten numerischen Modelle für das Aufschmelzen unter Berücksichtigung natürlicher Konvektion jedoch noch nicht ausreichend validiert.

In einem neu entwickelten Validierungsexperiment wird das Modell-Phasenwechselmaterial n-Octadekan durch Beheizung von zwei gegenüberliegenden vertikalen Seiten aufgeschmolzen. Der Phasenzustand und die Geschwindigkeiten in der flüssigen Phase werden anhand von Schattenbildern und der Strömungsmessmethode Particle Image Velocimetry ermittelt. Temperaturen im Material und an dessen Rändern werden mit Thermoelementen gemessen. Die durchgeführten Experimente liefern räumlich und zeitlich aufgelöste Daten der relevanten Größen einschließlich Fehleranalyse.

Zwei numerische Modelle zur Simulation des Aufschmelzens werden mit dem kommerziellen Strömungslöser ANSYS Fluent umgesetzt: Ein erstes detailliertes Modell mit variablen Materialwerten ermöglicht die Volumenausdehnung des Phasenwechselmaterials in eine Luftphase mit Hilfe der Volume-of-Fluid-Methode. Ein zweites vereinfachtes Modell nimmt konstante Materialwerte an und modelliert den Auftrieb mit der Boussinesq-Approximation. Aufgrund ähnlicher Ergebnisse wird das vereinfachte Modell ausgewählt, um das Experiment in einer 3D-Simulation einschließlich mechanischer und thermischer Randeinflüsse nachzubilden. Die in der Simulation auftretenden Geschwindigkeiten sind zwar höher als im Experiment, aber die für die Auslegung relevanteren Größen Phasenzustand und Temperaturen stimmen gut überein.

In einer numerischen Parameterstudie wird das vereinfachte Modell dazu verwendet das Aufschmelzen in rechteckigen Behältern mit verschiedenen Abmessungen zu untersuchen. Der Einfluss natürlicher Konvektion wird durch das Verhältnis aus dem tatsächlichen Wärmestrom zu einem fiktiven Wärmestrom durch Wärmeleitung bemessen. Messdaten aus dem Experiment mit verschiedenen treibenden Temperaturdifferenzen ergänzen die Studie. Daraus abgeleitete Korrelationen in dimensionsloser Form schätzen ähnliche Aufschmelzvorgänge in einem weiten Parameterbereich ab. Dies ermöglicht die Berücksichtigung des Einflusses natürlicher Konvektion in der Auslegung von Latentwärmespeichern ohne zeit- und kostenaufwändige Simulationen.

Abstract

Latent heat storage could play an important role in bridging the gap between supply and demand of sustainable energy sources. However, the numerical models for natural convection dominated melting that are needed for storage system design are not sufficiently validated, due to a lack of suitable experiments.

A novel validation experiment for the melting of a model phase change material (n-octadecane) by heating from two vertical opposite sides was developed. The phase state and the velocities in the liquid phase were measured using shadowgraphy and Particle Image Velocimetry. Interior and boundary temperatures were measured with thermocouples. The performed experiments delivered space and time-resolved data of the relevant quantities including an error analysis.

Two numerical models for natural convection dominated melting were developed with the commercial fluid flow solver ANSYS Fluent: a first detailed model with variable material properties allows volume expansion of the phase change material into an air phase with the volume of fluid method. A second simplified model assumes constant material properties and models buoyancy with the Boussinesq approximation. Due to similar results, the simplified model was selected to reproduce the experiment in a 3D simulation including mechanical and thermal boundary effects. The simulated velocities were found to be higher as in the experiment, but the liquid phase fraction and temperatures, which are more relevant to the design process, agreed well.

In a numerical parameter study, the simplified model was used to investigate melting in rectangular enclosures with various dimensions. The influence of natural convection on heat transfer was assessed with the introduced convective enhancement factor, which was defined as the ratio of the actual heat flux to a hypothetical heat flux by conduction. The study was extended with experimental data for three different values of driving temperature difference. Correlations for the liquid phase fraction in dimensionless form were derived to predict similar melting processes for a large parameter range. This enables the consideration of natural convection in the design of latent heat storage systems without expensive and time-consuming numerical analyses.

Preface

This thesis was written during my time as a researcher at the Institute of Engineering Thermodynamics at the German Aerospace Center (DLR) in Stuttgart. I already wrote three research articles on the same topic that have been published or submitted for publication. In this thesis, my research on melting governed by natural convection in rectangular enclosures is joined and presented as a whole.

Several students assisted my research and contributed to the findings presented in this work. The first student on this topic was Jonina Felbinger, who performed a numerical parameter study on natural convection dominated melting in her Bachelor's thesis. Lisa Böhm assisted in the assembly, setup and testing of the experimental test bench during her Bachelor's thesis. Janina Hagedorn assisted in the setup of optical measurement techniques and also performed numerical simulations in her Bachelor's thesis. Vanessa Schönfelder performed a comprehensive measurement campaign, optimized the PIV evaluation and performed an error analysis on measured data during her Master's thesis.

Acknowledgments

First of all, I want to thank my supervisors Markus Eck, Stefan Zunft and Dan Bauer for guiding me through the challenging task of research and writing a PhD thesis. Special thanks go to André Thess for instructing me more than you would expect regarding his many responsibilities. Our in-deep discussions about my research topic inspired me and his valuable and entertaining talks were always a source of motivation. I also want to thank Oleg Zikanov for welcoming me to a wonderful research stay at the University of Michigan, where I gained a deeper understanding of numerical simulation.

I am also very thankful to my colleague Maike Johnson, who instructed me at the beginning, which paved the way for a great collaboration throughout my whole time at DLR. I want to thank Matthias Hempel for the many discussions on the modeling of latent heat storage systems, which gave me a lot of insight into the topic. I also want to thank Duncan Gibb for his help with translation and for having a good time together in our office, and Andrea Gutierrez for keeping the mood up with her many visits to our office. I also want to thank Chris Willert from DLR in Cologne for providing me with a testing license of PIVview which enabled a high quality evaluation of experimental velocity measurements.

Exceptional thanks go to Jonina Felbinger. Our many discussions, her fantastic mood, her enthusiasm and her scientific skills shaped my work in a special way. But most importantly I would not want to miss our friendship that evolved over the last couple of years. And, of course, I am also thankful for her correction of this thesis. I am also very grateful for my friendship with Stefano Ruberto and Stefan Brack, our weekly lunch, where we almost never talked about work, and our weekend nights out to distract ourselves from the daily grind.

Last but not least, I want to thank my father Wolfgang Vogel for sparking my scientific curiosity through our hour lasting discussions on physics or technology and I want to express my deepest gratitude to my mother Cornelia Vogel for supporting me in every possible way at all times.

Contents

Nomenclature	vii
1 Introduction	1
1.1 Motivation	1
1.2 Melting and solidification in latent heat storage	3
1.3 Objectives and outline	5
2 Experiments for validation	7
2.1 State of research	7
2.2 A novel validation experiment	8
2.2.1 Generic benchmark test case	9
2.2.2 Test bench design and operation	10
2.2.3 Material properties	14
2.2.4 Test runs	16
2.3 Measurement techniques	17
2.3.1 Shadowgraph imaging	17
2.3.2 Particle image velocimetry	19
2.3.3 Thermocouple measurements in the PCM	23
2.4 Results and discussion	23
2.4.1 Visualization of the transient melting process	24
2.4.2 Measurement and evaluation errors	30
2.4.3 Measured boundary conditions	32
2.4.4 Quantitative results for validation	35
2.5 Conclusions	38
3 Numerical modeling and validation	41
3.1 State of research and objectives	41

3.2	Numerical modeling	43
3.2.1	Model simplifications	43
3.2.2	Modeling of material properties	44
3.2.3	Governing equations	46
3.2.4	2D domains, initial and boundary conditions (V-2D, B-2D)	50
3.2.5	3D Boussinesq model with boundary effects (B-3D)	52
3.2.6	Discretization	54
3.3	Results and discussion	55
3.3.1	Comparison of the 2D models V-2D and B-2D	55
3.3.2	Comparison of the 3D Boussinesq model (B-3D) with the experiment	61
3.4	Conclusions	67
4	Heat transfer enhancement due to natural convection	69
4.1	State of research and objectives	69
4.2	Numerical parameter study on enclosure dimensions	71
4.2.1	Material properties	72
4.2.2	Geometry and parameter variation	72
4.2.3	Comparison of the phase front shape	74
4.2.4	Liquid phase fractions over time	76
4.2.5	Scaling of the melting process	77
4.2.6	The impact of natural convection on heat transfer	78
4.3	Experimental parameter study on driving temperature differences	82
4.4	Conclusions	84
5	Summary and outlook	85
5.1	Summary	85
5.2	Outlook	87
5.2.1	Temperature measurement with high spatial resolution	87
5.2.2	High temperature experiments with nitrate salts	88
5.2.3	Efficient simulation of highly resolved 3D domains	88
5.2.4	Modeling of natural convection with enhanced thermal conductivity for large scale models	89
5.2.5	Melting in finned shell and tube systems	91
	References	95

Nomenclature

Latin letters

A	aspect ratio
a	thermal diffusivity, $[a] = \text{m}^2/\text{s}$
B	momentum source term coefficient, $[B] = \text{Pa s}/\text{m}^2$
b_1, b_2	curve-fit function parameters
C	mushy region or mushy zone constant, $[C] = \text{Pa s}/\text{m}^2$
c_p	specific isobaric heat capacity, $[c_p] = \text{J}/(\text{kg K})$
D	depth, $[D] = \text{m}$
d	diameter, $[d] = \text{m}$
$\hat{\mathbf{e}}_y$	unit vector in y -direction
\mathbf{F}_b	buoyancy term in momentum equation, $[\mathbf{F}_b] = \text{Pa}/\text{m}$
Fo	Fourier number
f_l	liquid phase fraction
g	gravity constant, $[g] = \text{m}/\text{s}^2$
H	height, $[H] = \text{m}$
h	specific enthalpy, $[h] = \text{J}/\text{kg}$
\mathbf{I}	unit tensor
k	thermal conductivity, $[k] = \text{W}/(\text{m K})$
\dot{m}	volumetric mass flow between phases in VOF model, $[\dot{m}] = \text{kg}/(\text{m}^3 \text{s})$
p	pressure, $[p] = \text{Pa}$
\dot{Q}	heat transfer rate, $[\dot{Q}] = \text{W}$
q	constant in momentum source term coefficient B
L	latent heat, $[L] = \text{kJ}/\text{kg}$
Ra	Rayleigh number
Re	Reynolds number

Nomenclature

S_h	source term in the energy equation, $[S_h] = \text{W/m}^3$
\mathbf{S}_u	source term in the momentum equation, $[\mathbf{S}_u] = \text{Pa/m}$
St	Stokes number
Ste	Stefan number
T	temperature, $[T] = ^\circ\text{C}$
t	time, $[t] = \text{s}$
\tilde{t}	scaled time
Pr	Prandtl number
U	bulk velocity, $[U] = \text{m/s}$
\mathbf{u}	velocity vector, $\mathbf{u} = (u, v, w)^\top$
u, v, w	x, y, z -velocity, $[u, v, w] = \text{m/s}$
W	width, $[W] = \text{m}$
x, y, z	coordinates, $[x, y, z] = \text{m}$

Greek letters

α	volume fraction in VOF model
β	thermal expansion coefficient, $[\beta] = 1/\text{K}$
δ	distance of free surface from max. height, $[\delta] = \text{m}$
ε	convective enhancement factor
μ	dynamic viscosity, $[\mu] = \text{Pa}\cdot\text{s}$
ν	kinematic viscosity, $[\nu] = \text{m}^2/\text{s}$
ζ	half melting range in melting point model, $[\zeta] = ^\circ\text{C}$
ρ	density, $[\rho] = \text{kg/m}^3$
σ	surface tension, $[\sigma] = \text{N/m}$
τ	characteristic time, $[\tau] = \text{s}$
$\boldsymbol{\tau}$	stress tensor, $[\boldsymbol{\tau}] = \text{Pa/m}$

Subscripts

0	initial value
bf	backflow
cond	heat conduction
conv	heat convection
crit	critical value for the onset of natural convection

exp	experimentally measured values
f	flow
g	gravitational
l	liquid
lat	latent heat content
m	melting point
max	maximum
min	minimum
p	particle
rad	radiation
ref	reference
s	solid
sens	sensible heat content
w	wall

Symbols and operators

∇	nabla operator: $\nabla = \left(\frac{\partial}{\partial x}, \frac{\partial}{\partial y}, \frac{\partial}{\partial z} \right)$
Δ	finite difference

Abbreviations

CAD	Computer Aided Design
CFD	Computational Fluid Dynamics
ETC	enhanced thermal conductivity
FFT	fast Fourier transform
HTF	heat transfer fluid
LHS	latent heat storage
PCM	phase change material
PIV	particle image velocimetry
PWM	pulse width modulation
SIMPLE	Semi-Implicit Method for Pressure Linked Equations
UDF	user defined function
VOF	volume of fluid

Chapter 1

Introduction

This introduction into the topic firstly gives a motivation for the presented research on melting governed by natural convection in latent heat storage. Secondly, the processes of melting and solidification during charging and discharging of a latent heat storage are explained. Finally, the objectives and outline of this thesis are stated. References to the state of research are brief during this introduction, because each of the following three main chapters 2-4 contain an additional state of research section that focuses on the particular topic of the chapter.

1.1 Motivation

Experts have been warning of the consequences of anthropogenic climate change for several decades. The Intergovernmental Panel on Climate Change states: "Warming of the climate system is unequivocal, and since the 1950s, many of the observed changes are unprecedented over decades to millennia. The atmosphere and ocean have warmed, the amounts of snow and ice have diminished, and sea level has risen" [1]. One of the most promising contributions to counteract climate change is the increased use of sustainable energy sources free of greenhouse gas emissions, such as wind and solar energy. However, these sustainable energy sources are not constantly available and energy storage is needed to increase their use. Thermal energy storage can thereby play an important role in different application scenarios [2].

Latent heat storage (LHS) with a solid-liquid phase change material (PCM) can have advantages over sensible heat storage due to its high energy density in a small temperature range. An overview of materials and applications was

composed by Mehling and Cabeza [3] and Bauer et al. [4]. Latent heat storage is most efficient in combination with a heat transfer fluid (HTF) that changes phase as well, e.g. boiling or condensation of water. Then, low overall temperature differences can be achieved, which leads to high exergetic efficiency [5]. Recent industrial applications with a demand for high temperature LHS include solar thermal power plants with direct steam generation [6], facilities with process heat or steam [7, 8] or electricity storage using pumped thermal energy storage [9, 10].

Although LHS has advantages over other storage technologies, it has been barely used in industrial applications. The main reason is the extensive design of heat exchangers needed to overcome the low thermal conductivity of common storage materials. Different heat exchangers have already been successfully tested [11, 12]. The remaining problem is that the geometry always has to be adjusted to the specific application. Numerical modeling thereby becomes increasingly important, because simulations allow to optimize storage systems without extensive experimental testing. However, solid-liquid phase change requires detailed transient modeling. And this is especially challenging when natural convection in the liquid phase is the dominant heat transfer mode. Then, a coupled equation system for heat transfer, phase change and fluid flow has to be solved.

A large amount of numerical models suitable for solid-liquid phase change governed by natural convection were developed and collected in several reviews [13–17]. However, their validation is still an issue and the modeling accuracy for specific applications is often unknown. Detailed experiments of solid-liquid phase change are rare and mostly not fully suitable for validation of numerical models. As stated by Kadri et al. [18], there is a general need for more validation experiments. Moreover, there are hardly any specific validation experiments for the geometry and boundary conditions found in latent heat storage. Finally, the velocity field due to natural convection in the liquid phase has not yet been measured throughout the transient melting process.

A validated numerical model can finally be used to analyze storage designs. But still, due to complex geometries, detailed simulations of latent heat storage systems need large amounts of time and computational effort. Therefore, to increase the speed and efficiency of the design process, analytical correlation equations in dimensionless form are needed. Many researchers reported correlations from their experiments and also a theoretical analysis was derived [19]. But, as in the case of validation experiments, correlations were not necessarily developed for the geometry and boundary conditions found in latent heat storage.

In conclusion, numerical modeling is crucial in the design process of latent heat storage, but more experiments with detailed measurements are required. And, to facilitate the design process of latent heat storage systems, correlated analytical equations for the phase change process have to be derived.

1.2 Melting and solidification in latent heat storage

An example of a latent heat storage system with flat plate design developed by Johnson et al. [20] is depicted in Figure 1.1. In this case, the HTF flows inside of vertical hollow plates while the PCM is filled into the spaces between the plates.

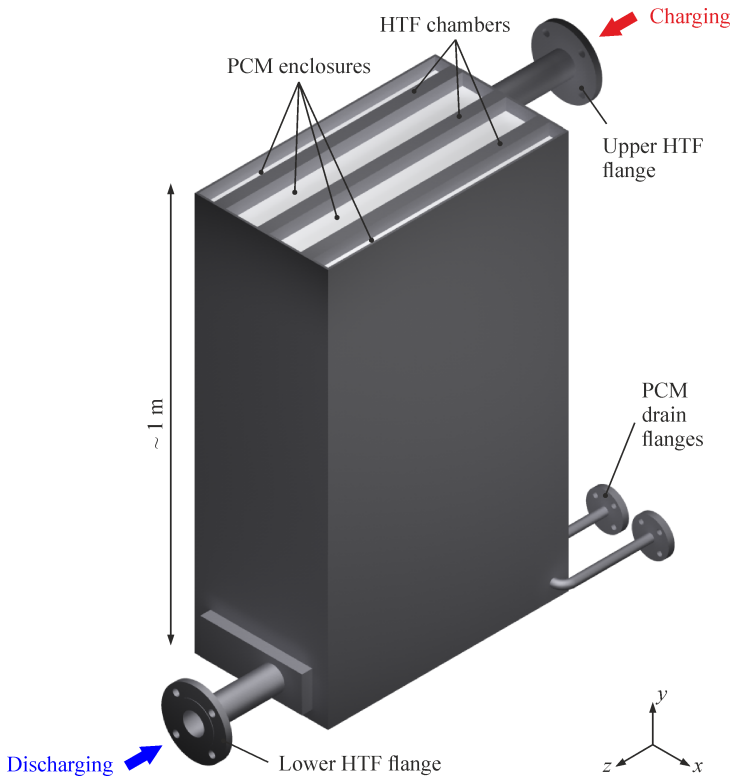


Figure 1.1: Flat plate latent heat storage: the HTF flows through vertical hollow plates and the PCM is enclosed in the spaces between the plates [21].

Phase change processes governed by natural convection have been described by many researchers in the past. One of the earliest investigations was a solidification experiment by Szekely and Chhabra [22] and a melting experiment by Hale and Viskanta [23]. To give a better understanding of the operation of a LHS system, the charging and discharging processes are illustrated in Figure 1.2.

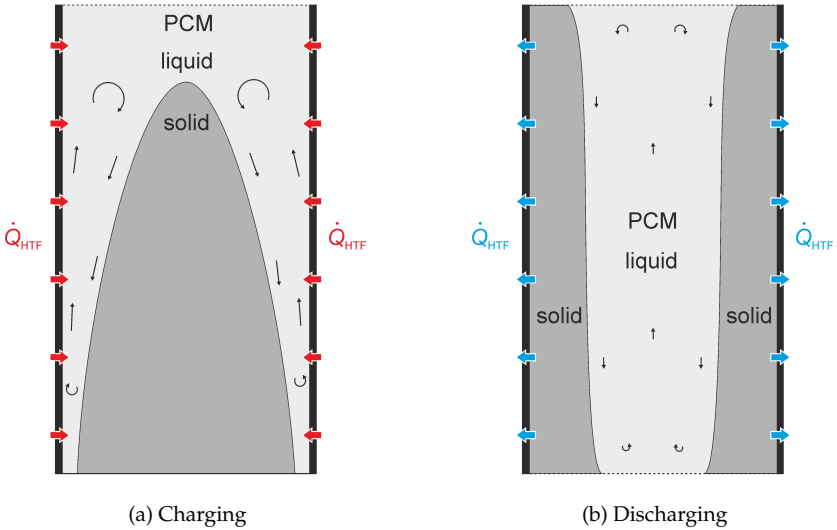


Figure 1.2: Operation modes of a latent heat storage system.

While charging the storage, heat is transferred from the HTF into the PCM, which heats up and melts. Initially, heat is transferred by heat conduction with a maximum rate at the beginning. But the heat transfer rate decreases with the growing size of the liquid layer between the wall and the phase front. However, with increasing liquid layer width, natural convection is likely to occur, which improves the heat transfer rate over heat conduction. The driving temperature difference between the hot wall and the phase front leads to a density gradient in the liquid that drives an upward flow at the heated walls and a downward flow at the colder phase front. The occurrence and strength of this natural convection thereby depends on material properties, dimensions and boundary conditions. While discharging, heat is transferred from the PCM to the HTF; the PCM cools down and solidifies. However, the driving temperature difference between the cold wall and the phase front now occurs over a solid layer that prevents fluid

flow. Only weak natural convection is observed in the liquid layer behind the phase front and only as long as the liquid is still superheated. Consequently, the heat transfer rate during solidification is hardly affected by natural convection.

1.3 Objectives and outline

This thesis contributes to three research objectives, which are addressed in separate chapters: Chapter 2 presents a novel validation experiment of the melting of n-octadecane by symmetric heating from two vertical sides in a rectangular enclosure using optical measurement techniques to obtain phase state and velocities with high spatial and temporal resolution. Solidification experiments are not included due to the minor impact of natural convection. Chapter 3 is about the development, comparison and validation of numerical models for solid-liquid phase change governed by natural convection using the commercial software package ANSYS Fluent. Chapter 4 shows results from a parameter study on enclosure dimensions and driving temperature differences. A scaling analysis is performed to derive simplified analytical correlation equations in dimensionless form that facilitate the design process of latent heat storage systems.

Chapter 2

Experiments for validation

A novel experiment for the validation of numerical models is presented. The experiment was specifically designed for latent heat storage geometries and boundary conditions. The phase state, velocities in the liquid phase and temperatures were measured with high detail and accuracy and an error analysis was performed for all the measured quantities. But before this validation experiment is explained in detail, the state of research on similar validation experiments is examined more closely.

2.1 State of research

The melting in rectangular enclosures was typically investigated with an isothermally heated side wall and an opposing side that was either isothermally cooled [18, 23–30] or insulated [31, 32]. The bottom was an insulated wall and the top was either a wall [23, 25, 27–31] or a free surface [18, 24, 26, 33]. The PCM was initially in the solid state with a temperature below and near the melting point and was then melted by raising the temperature of the heated wall to a constant value above the melting point. Organic materials with low melting temperatures, such as paraffins [18, 30], n-octadecane [23, 24, 26, 31], n-heptadecane [33], lauric acid [32] or metals such as gallium [25, 28, 29] or tin [27] were used. To reduce heat losses to the environment, the housing was insulated in all of the experiments and some of them additionally used a system of active trace heating to raise the temperature in a surrounding casing to the melting temperature of the PCM [23, 25]. Researchers reported the formation of gas filled cavities during solidification that lead to bubbles rising throughout

the melting process. The reason is that the investigated materials have a higher density in the solid phase than in the liquid phase and ambient air or other gases solved in the liquid phase fill the resulting cavities. To reduce this problem, it was suggested to vibrate the cell [23] or solidify only small layers of material at once [26, 32]. To allow photographic observation of the phase state of materials that are transparent in the liquid form, front and back walls made of transparent acrylic glass were used [18, 23, 24, 26, 30–33]. For opaque materials, the pour-out and probing method [25, 27] and the x-Ray radioscopy [28] were used to measure the phase front. Both the phase front and the velocities in the liquid phase in one direction at distinct positions were measured by ultrasonic Doppler velocimetry (UDV) [29]. Velocities in the liquid phase of the PCM were measured with high spatial but low temporal resolution using Particle Image Velocimetry [30]. Temperature measurements in the PCM using thermocouples were done by many researchers [18, 23–26, 28, 29, 31, 32]. With Interferometry, additional information about temperature isotherms and heat transfer at the heated wall and the solid-liquid interface was gained [33].

Despite the presented research, there has been a general interest in more experiments [18]. And more specifically, regarding the topic of this thesis, the following experimental features or results are still missing in the state of research: the phase state during symmetric melting of a PCM between two isothermally heated vertical sides, while all other sides are adiabatic, has not been measured, although this is a commonly used arrangement in latent heat storage [20, 34]. Boundary effects have not been assessed, because temperatures or heat flow rates at the boundaries have not been recorded. An analysis of measurement errors has not been performed in any of the mentioned validation experiments. Finally, there have not been transient measurements of flow velocities in the liquid phase with high spatial and temporal resolution.

2.2 A novel validation experiment

A novel validation experiment was developed specifically for a LHS system with symmetric heating from two opposite vertical side walls. An application-oriented storage system would have a complex geometry with heat transfer structures for increased power. However, a complicated geometry would restrict the measurement techniques; especially optical access to the PCM would not be possible. Therefore a simplified geometry was chosen while the principal

topology of the LHS system was kept. The simplest suitable geometries are the rectangular, cylindrical and spherical enclosure. The decision fell in favor of the rectangular enclosure, because it allows undistorted optical visibility of the phase front during melting and because it is common in latent heat storage systems. The result is a generic benchmark test case with optimal measurement conditions that inherits the boundary conditions of a LHS system. A model material (n-octadecane) with a low-temperature melting point and well-known material properties was used to reduce heat exchange with the environment and to gain accurate results.

2.2.1 Generic benchmark test case

The generic benchmark test case is illustrated in Figure 2.1: a PCM is isothermally heated from two opposing vertical sides in a symmetric rectangular enclosure of height H and half width W . The bottom side is an adiabatic wall and the top side is an adiabatic free surface. The PCM is initially solid at a temperature T_0 slightly below the melting point T_m of the PCM. At time t_0 the temperature at the heated walls is raised to a temperature $T_w = T_m + \Delta T$ and melting starts as soon as the melting point is reached.

The relevant dimensionless numbers of the melting process are the Rayleigh number Ra_H , the Stefan number Ste , the time dependent Fourier number $Fo_H(t)$, the Prandtl number Pr and the aspect ratio A :

$$\begin{aligned} Ra_H &= \frac{g\beta_1\Delta TH^3}{\nu_1 a_1}, & Ste &= \frac{c_{p,l}\Delta T}{L}, \\ Fo_H(t) &= \frac{a_1 t}{H^2}, & Pr &= \frac{\nu_1}{a_1}, & A &= \frac{H}{W}. \end{aligned} \quad (2.1)$$

Thereby, g is the gravity constant and β_1 is the thermal expansion coefficient in the liquid state. The kinematic viscosity is denoted by ν_1 , the thermal diffusivity by a_1 and the specific isobaric heat capacity by $c_{p,l}$. Finally, L is the latent heat.

Melting is initially dominated by heat conduction, but natural convection sets in as soon as the liquid layer reaches a critical size, so that the buoyancy forces due to temperature gradients can overcome the viscous forces due to boundary layers at the walls and at the liquid-solid interface. A criterion for the transition from the pure conduction regime to a convection affected regime was derived by Batchelor [35]. The correlation is given here with the height used as characteristic length instead of the originally used width. The flow is dominated by natural

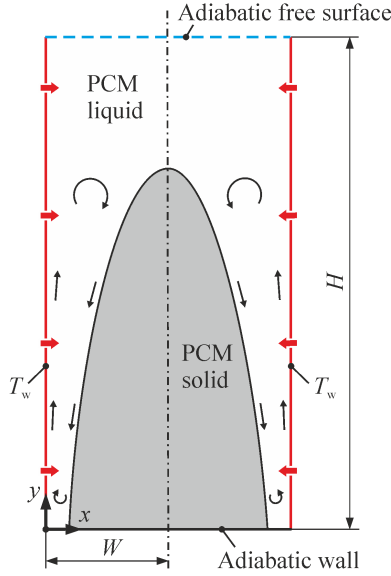


Figure 2.1: Definition of the generic benchmark test case.

convection, if

$$\frac{Ra_H}{A^4} \geq 500. \quad (2.2)$$

The onset of turbulence was studied by Elder [36]. The correlation is also given with the height as characteristic length instead of the originally used width. The flow is characterized to be laminar for

$$Ra_H < 10^{10}. \quad (2.3)$$

2.2.2 Test bench design and operation

The experimental setup is shown in Figure 2.2: a transparent enclosure made of acrylic glass PLEXIGLAS® contained heaters made of Steel 1.4301 and the PCM n-octadecane. Ambient air filled the remaining space to allow for volume change of the PCM.

The half width of the test section was $W = 25$ mm. The height of the heaters and the initial fill height of the PCM in the liquid state were $H_1 = 105$ mm. The fill height was specifically chosen to achieve an average height $H = 100$ mm during

2.2 A novel validation experiment

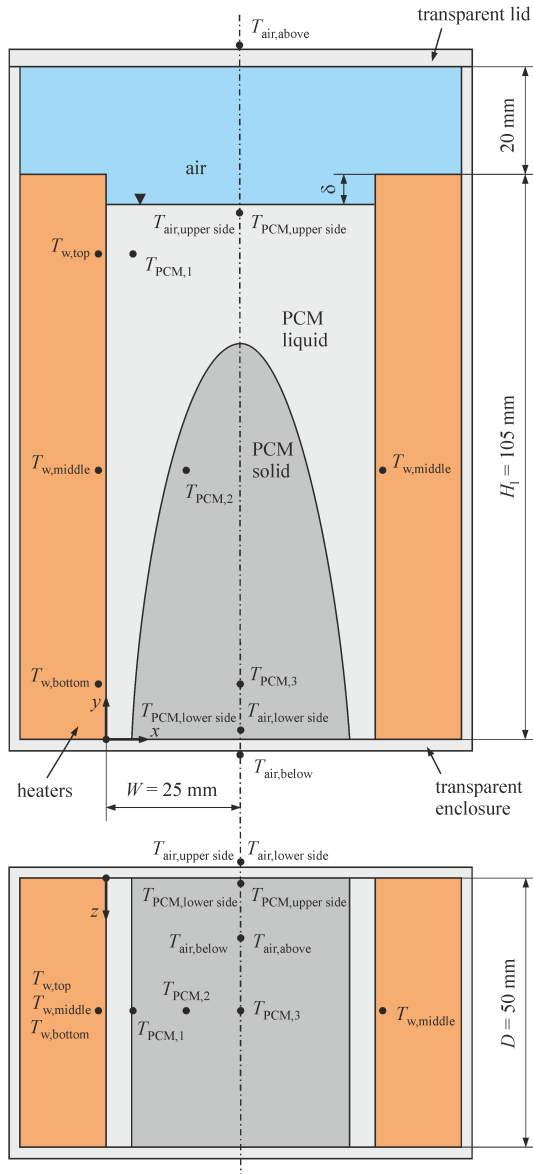


Figure 2.2: Experimental setup: front view (upper image) and top view (lower image). Thermocouple positions are shown with filled circles.

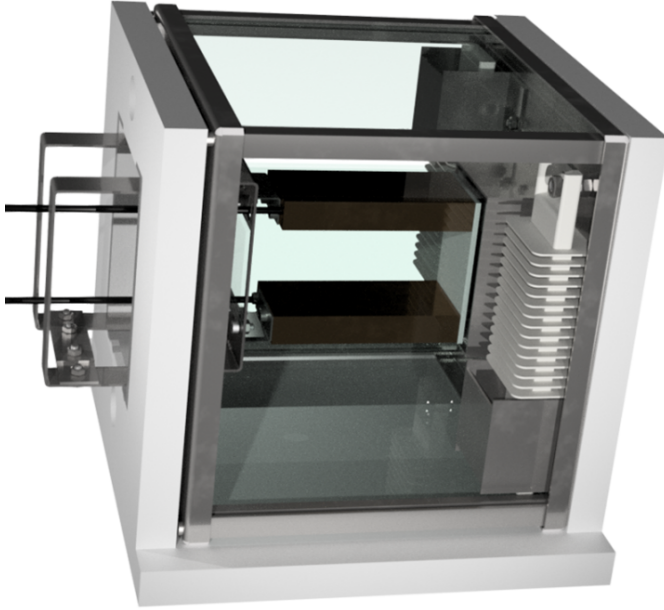
the melting process. During solidification, the height decreased by the length δ due to a higher density in the solid state. After solidification, the decline was $\delta \approx 10$ mm and the solid fill height was $H_s \approx 95$ mm. The depth of the test volume $D = 50$ mm was large enough to neglect boundary effects at the mid-plane induced by the front and back walls and it was small enough to ensure a good quality of optical measurements.

To heat up the PCM, two custom built electric heaters made of stainless steel 1.4301 were used. They were designed for temperatures up to 300 °C for later high temperature test runs. Each one was made of two plates that were welded together. A meandering path was milled into one of the plates to leave space for a heating coil with 330 W power that heats the plates uniformly. To measure and control the wall temperatures of the two heaters at mid-height $T_{w,middle}$ two T-type thermocouples with 0.7 mm diameter were used. The thermocouples were positioned 1 mm inside the heating plates at the center of the heater wall. To test the temperature uniformity of the steel plates, the temperatures at the top $T_{w,top}$ and bottom $T_{w,bottom}$ of one of the heating plates were additionally measured over a complete melting process. The heaters were fixed onto a lid construction for the transparent enclosure that also featured two fused silica top windows for insulation and optical access. The transparent enclosure with the heaters and lid construction was placed into an outer chamber equipped with temperature controlled trace heaters to heat up the air and thus reduce heat losses to a minimum. A CAD drawing and a photograph of the test chamber are shown in Figure 2.3.

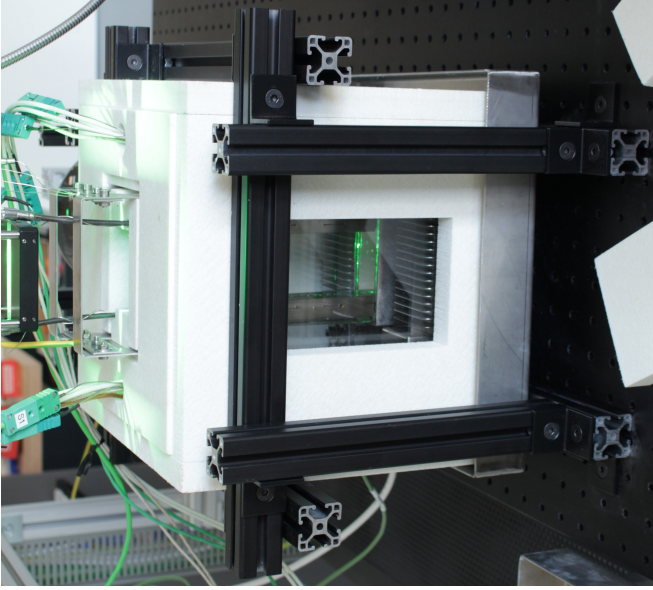
The casing of the outer chamber was also made of stainless steel 1.4301, in which fused silica windows were inserted at the sides. The outside faces were covered with an insulation material of 20 mm thickness and a thermal conductivity of $k = 0.05$ W/(m K). Cutouts can be removed at the front and back sides and at the top to allow optical access, see Figure 2.3 (b).

The outer chamber was used to heat up the air at the outside of the transparent enclosure to the same temperature as the PCM inside the enclosure to achieve near-adiabatic boundary conditions. The Temperatures in the PCM at the enclosure boundaries were measured with T-type thermocouples of 0.35 mm and 0.5 mm diameter, and in the air at the enclosure boundaries with thermocouples of 0.7 mm diameter. The thermocouples were placed at six different positions, which are shown in Figure 2.2.

The PCM temperatures at the upper side of the enclosure $T_{PCM,upper\ side}$ and at the lower side $T_{PCM,lower\ side}$ were used as set points for three independent



(a) CAD drawing of test chamber design



(b) Photography of the test bench implementation

Figure 2.3: Test chamber design with inner transparent enclosure that is placed into an outer chamber to reduce heat losses and actively control the surrounding air temperature to achieve near-adiabatic boundary conditions.

trace heater control loops. A first loop controlled the air temperature at the bottom boundary below the enclosure $T_{\text{air, below}}$ with a temperature controlled coil heater in a steel plate that was inserted below the PCM enclosure with an air gap in between. The second and the third loop controlled the temperatures of the air at the side boundaries of the enclosure $T_{\text{air, upper side}}$ and $T_{\text{air, lower side}}$ with four temperature controlled finned strip heaters. Two of the finned strip heaters were mounted at the bottom (visible in Figure 2.3) and two at the top of the outer chamber. This way, thermal stratification in the air could be controlled to be similar as in the PCM, which led to low heat exchange. The temperature at the top boundary $T_{\text{air, above}}$ was not actively controlled, because heat conduction through the air layer at this boundary is significantly smaller than at the other boundaries and it was not possible to optimally control all the boundary temperatures.

The power of all heaters was controlled with five separate PID loops implemented in LabVIEW® and ran on a compact RIO platform with a thermocouple module and a digital output module. The controller outputs were transformed into pulse width modulated (PWM) signals that ran the heaters with solid states relays. For each of the three air heaters, two cascaded PID loops were used, because of the large reaction time of air heating. The set point of an outer controller was the PCM temperature at an enclosure boundary, e.g. $T_{\text{PCM, lower side}}$, and the plant value was the air temperature at the same boundary, e.g. $T_{\text{air, below}}$. The output of the outer controller and the setpoint for the inner controller was the required heater temperature. The plant value of the inner controller was the measured heater temperature and the output was the heater power as PWM signal. This way, a fast reacting inner loop controlled the heater temperature and a slow reacting outer loop controlled the desired air temperatures at the enclosure boundaries.

The liquid PCM was filled into the enclosure in multiple layers that solidified subsequently to reduce the formation of air filled cavities. The whole system was then preheated to the designated initial Temperature T_0 of the PCM. When the PCM and boundary temperatures deviated by less than 0.1 K from T_0 , a steady state was declared and the melting process was started.

2.2.3 Material properties

For low temperature experiments, n-octadecane, which melts at a temperature of $T_m = 28^\circ\text{C}$, was used. It is transparent in the liquid state, which allows the use of

optical measurement techniques, and its material properties are well-known. A thorough data set was provided by Galione et al. [37], from which the properties given in Table 2.1 were adapted. The surface tension was measured by Jasper [38].

Table 2.1: Thermophysical material properties of n-octadecane in the solid (s) and liquid (l) state [37, 38].

Property	Unit	$T \leq T_m$	$T > T_m$
ρ_s		863	-
ρ_l	kg/m ³	778.466	$1010.07 - 0.80587 \cdot (T + 273.15) + 0.00012463 \cdot (T + 273.15)^2$
$c_{p,s}$	J/(kg K)	1942	-
$c_{p,l}$		2214.08	$2137.1456 + 2.7186 \cdot T$
k_s	W/(m K)	0.3362	-
k_l		0.151215	$0.156427 - 0.0001841779 \cdot T$
μ_l	Pa s	-	$0.02966723 - 8.533286 \cdot 10^{-5} \cdot (T + 273.15)$
β_l	1/K	-	$8.9 \cdot 10^{-4}$
σ_l	N/m	-	$0.02998 - 8.428 \cdot 10^{-5} \cdot T$
T_m	°C	28	-
L	kJ/kg	242.454	-

Properties depending on temperature T and liquid phase fraction f_l are the density ρ , the heat capacity c_p and the thermal conductivity k . Constant values are given for the solid state $T < T_m$, which was sufficiently accurate due to the low subcooling of 1 K in this experiment. The value in the liquid state at melting temperature $T = T_m$ is also given. Temperature-dependent values are given for the liquid phase with $T > T_m$. The dynamic viscosity μ_l is only specified in the liquid phase and the expression by Galione et al. [37] was linearized for the temperature region of this investigation. The surface tension σ_l is also only specified in the liquid state. Furthermore, the melting temperature T_m and the latent heat L are given. The thermal expansion coefficient β_l was derived from a

mean density $\bar{\rho}$ between the solid and liquid state and the density ρ_1 in the liquid region:

$$\beta = -\frac{1}{\bar{\rho}} \frac{\partial \rho_1}{\partial T} \Big|_{T_m}. \quad (2.4)$$

The thermophysical properties of the steel heaters used to heat up the PCM, the PLEXIGLAS[®] enclosure, in which the PCM is filled, and the properties of ambient air are given in Table 2.2.

Table 2.2: Thermophysical properties of enclosure materials and ambient air.

Property	Unit	Steel 1.4301	PLEXIGLAS [®]	Air
ρ	kg/m ³	7900	1180	1.225
c_p	J/(kg K)	500	1470	1006
k	W/(m K)	15	0.19	0.0242
μ	Pa s	-	-	$1.791 \cdot 10^{-5}$

2.2.4 Test runs

The initial temperature was $T_0 = 27^\circ\text{C}$, which was 1 K below the melting point $T_m = 28^\circ\text{C}$ of the PCM. Three different experiments with driving temperature differences of 5 K, 10 K and 20 K were conducted. The corresponding values of the dimensionless numbers are given in Table 2.3. The material properties were taken at the average liquid temperature $T_m + \Delta T/2$. The Fourier number is given at the instant of completed melting $Fo_H(t_m)$.

With the criterion given by Equation 2.2, the flow was expected to be dominated by natural convection, at least after a certain liquid phase fraction was reached. And, the flow was laminar due to the criterion Equation 2.3.

Table 2.3: Dimensionless numbers for the three different experiments: i.e. Rayleigh number, Stefan number, Fourier number at time of completed melting, Prandtl number and aspect ratio.

Number	$\Delta T = 5 \text{ K}$	$\Delta T = 10 \text{ K}$	$\Delta T = 20 \text{ K}$
Ra_H	$1 \cdot 10^8$	$2 \cdot 10^8$	$4 \cdot 10^8$
Ste	0.046	0.092	0.19
Fo_m	0.23	0.11	0.048
Pr	55.1	52.2	46.5
A	4	4	4

2.3 Measurement techniques

To measure the relevant quantities of the described validation experiment, several measurement techniques were used: the phase state of the PCM was measured with shadowgraph imaging and the velocities in the liquid phase were examined with Particle Image Velocimetry (PIV). The data were acquired with high temporal and spatial resolution. Temperatures were measured with thermocouples. In addition to internal temperatures, boundary temperatures were measured to investigate thermal boundary effects.

2.3.1 Shadowgraph imaging

To get high-resolution data of the liquid phase fraction, shadowgraph images were digitally recorded and evaluated. As the phase state changes slowly over time, it was sufficient to take a shadowgraph measurement every minute during the experiment, which takes about three hours. The optical setup that was used for both the shadowgraph and the light sheet images (for PIV evaluation) is illustrated in Figure 2.4.

The test chamber was illuminated from one side with white light emitted from a high power LED CBT-140 by Luminus Devices. The LED was driven by an LED pulsing system (LPS) from Intelligent Laser Applications (ILA) GmbH. The diverging light emitted from the LED was condensed to nearly parallel light with a plano-convex spherical lens with 150 mm diameter and 300 mm focal length. To get a more uniform lighting, a white square diffusor plate with 200 mm edge length was placed in the optical path near to the test section.

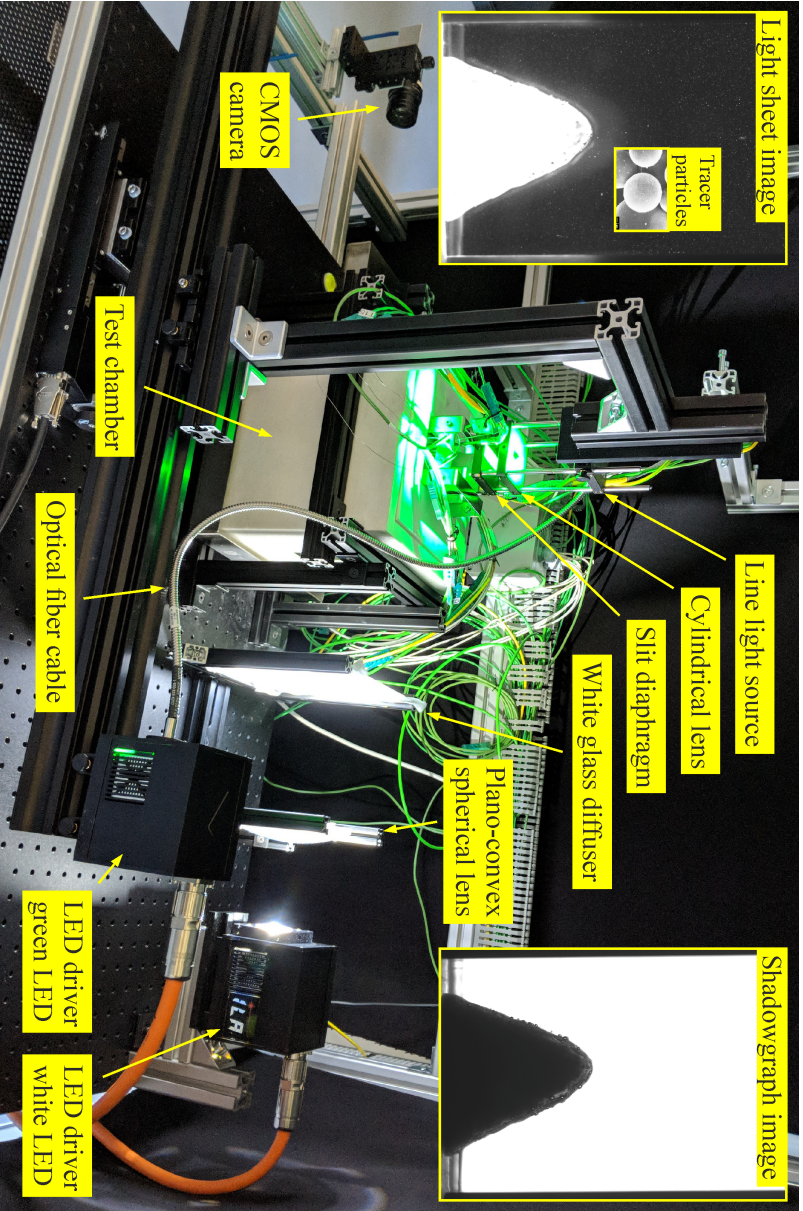


Figure 2.4: Optical setup for the illumination and recording of shadowgraph images and light sheet images (for PIV).

On the other side of the test section, an industrial monochrome camera (Blackfly USB3 by Point Grey) recorded the shadowgraph. It featured a 1/1.2" CMOS sensor Sony IMX249 with a resolution of 1200 x 1920 pixels at a maximum rate of 41 frames per second. A KOWA lens LM50HC with 50 mm focal length was used to project the image on the sensor. With this lens and the sensor positioned at a working distance of about 500 mm, a field of view of 52 mm x 107 mm, which was slightly larger than the test section dimensions, was obtained.

The image was read and cropped to the test section region by an acquisition program written in LabVIEW[®]. The conversion factor from image data to the physical space was determined to be 17.4 pixel/mm with the help of a calibration target. The liquid phase fraction at a certain time was calculated by summing up all of the pixel values in the backlight image, see Figure 2.5 (a), and dividing the result by its maximum possible value, which occurred at the end of the experiment when all PCM was melted.

2.3.2 Particle image velocimetry

Flow velocities were measured with high resolution in a two-dimensional plane using Particle Image Velocimetry (PIV). In PIV, tracer particles are used to visualize fluid flow and velocities are obtained by evaluating the displacement of particles in successive recordings. The theory behind this technique was described by Raffel et al. [39] and Adrian and Westerweel [40].

Uncoated hollow glass spheres were successfully tested in n-octadecane. The particles, which were provided by TSI inc, had a mean diameter of $d_p = 10 \mu\text{m}$ and a density of $\rho_p = 1100 \text{ kg/m}^3$. Although the particle density did not fully match the density of the PCM, the diameter was small enough to ensure good tracing behavior. The sinking (rising) velocity U_g of a particle in a quiescent fluid with density ρ_1 and viscosity μ_1 due to gravity can be approximately calculated from the Stokes equation, as stated by Raffel et al. [39]:

$$U_g = \frac{d_p^2 g (\rho_p - \rho_1)}{18 \mu_1}. \quad (2.5)$$

This equation is valid for a small particle Reynolds number

$$Re_p = \frac{\rho_1 U_r d_p}{\mu_1} \ll 1, \quad (2.6)$$

which was about $Re_p \approx 1 \cdot 10^{-2}$ in this case. The uncoated hollow glass spheres sank in n-octadecane with a velocity of $U_g = 5 \cdot 10^{-3} \text{ mm/s}$. This value was

sufficiently small in comparison to measured fluid velocities of up to 3 mm/s and indicates steady tracing ability. To also obtain dynamic tracing behavior, the Stokes number should be small,

$$St = \frac{\tau_p}{\tau_f} \ll 1. \quad (2.7)$$

The particle response time was calculated according to Raffel et al. [39], $\tau_p = 2 \cdot 10^{-6}$ s, and the characteristic time of the flow problem was estimated to be about $\tau_f \approx 1$ s. This results in a very low Stokes number of $St \approx 2 \cdot 10^{-6}$, which underlines the good tracing ability of the particles.

The tracer particles were illuminated with a light sheet parallel to the x - y -plane, see Figure 2.2. Green light with 525 nm wavelength was emitted by a high power LED (PT-121 by Luminus devices) that was mounted in a second LED driver of the LPS system. To form a light sheet, the light was coupled into an optical fiber cable connected to a line light source. A cylindrical lens with 40 mm height and 50 mm focal length focused the diverging light from the line light source onto a slit diaphragm with 50 mm length and 1 mm width. This way, most of the diffrused light due to incoherence, light source size and optical aberrations was cut off. A sharp light sheet was formed that illuminated a plane with 2 mm to 3 mm thickness over the whole height of the test section. The light sheet could be offset along the z -axis, see Figure 2.2, with a linear translation stage to measure in various planes parallel to the x - y -plane. The light was reflected by the tracer particles onto the same CMOS camera used for shadowgraphy. However, the two different light sources could not be used at the same time, since the shadowgraph illumination would outshine the scattered light from the particles with lower intensity. The other way around, the light sheet would illuminate the solid phase inhibiting proper shadowgraph images. The LabVIEW[®] program automatically controlled alternating shadowgraph and lightsheet illumination, camera configuration, image acquisition and data storage.

A PIV measurement was taken every minute directly after the shadowgraph measurement. At every measurement, a series of 40 images was recorded over 10 s to obtain transient and average data. Approximately 200 of these measurement sets were taken in every experiment to obtain a temporal resolution of the whole melting process. A camera frame rate of 4 frames/s (250 ms exposure distance) was chosen to measure velocities, which were below 3 mm/s. The frame rate was adjusted to allow a maximum particle travel of 25 % within a PIV evaluation window between two successive frames, because this has been often stated

as optimum value [39]. An exposure time of 30 ms was long enough for sufficient light intensity and short enough to avoid motion blur of the particles. However, the camera sensor had to be driven with nearly maximum gain.

The evaluation of velocities was done with the commercial software PIVview conceived by C. Willert, PIVtec GmbH. The underlying algorithms have been described by Raffel et al. [39]. The software also provided algorithms for preprocessing, such as image filters, background removal and masking, and for post-processing, such as calibration and data validation.

Regions that were not to be evaluated, such as the solid phase of the PCM, had to be masked to get proper results from the PIV evaluation. However, in the case of PCM melting, a manual masking for every measurement, which was necessary due to movement of the phase front, would have been inefficient. Instead, the shadowgraph images, which were taken before every series of light sheet images, were used to automatically create masks. In Figure 2.5 (a) an original shadowgraph image is shown. Several algorithms from the LABVIEW[®] Vision Development module, e.g. black and white conversion or closing of holes were used to gain suitable mask images, see Figure 2.5 (b). The software PIVview was operated from a windows command prompt, which made it directly accessible from LabVIEW[®] so that mask images could be assigned to PIV image pairs automatically.

To enhance the contrast and remove unwanted features in the images, a background removal was performed. As background image, the mean image of the 40 successive light sheet images recorded over 10 s was used, as shown in Figure 2.5 (c). Finally, the light sheet images were filtered with a high pass filter with Gaussian weighing and a kernel size of 1.5 pixels. A final preprocessed light sheet image is shown in Figure 2.5 (d).

For PIV evaluation, evaluation windows of 12 pixels in x -direction and 48 pixels in y -direction with a step size of 8 pixels in x -direction and 48 pixels in y -direction were used. This led to a vector grid with 112 vectors in x -direction and 39 vectors in y -direction. The larger window and step size in y -direction accounted for higher velocities in this direction and improved visibility of the resulting larger vectors. In contrast, the smaller window and step size in x -direction accounted for smaller velocities in this direction and better resolved the boundary layers at the heated vertical walls and the phase front of the PCM.

A fast Fourier transform (FFT) correlation with two repeated correlations and multiplication of correlation planes was used. A multiple-pass interro-

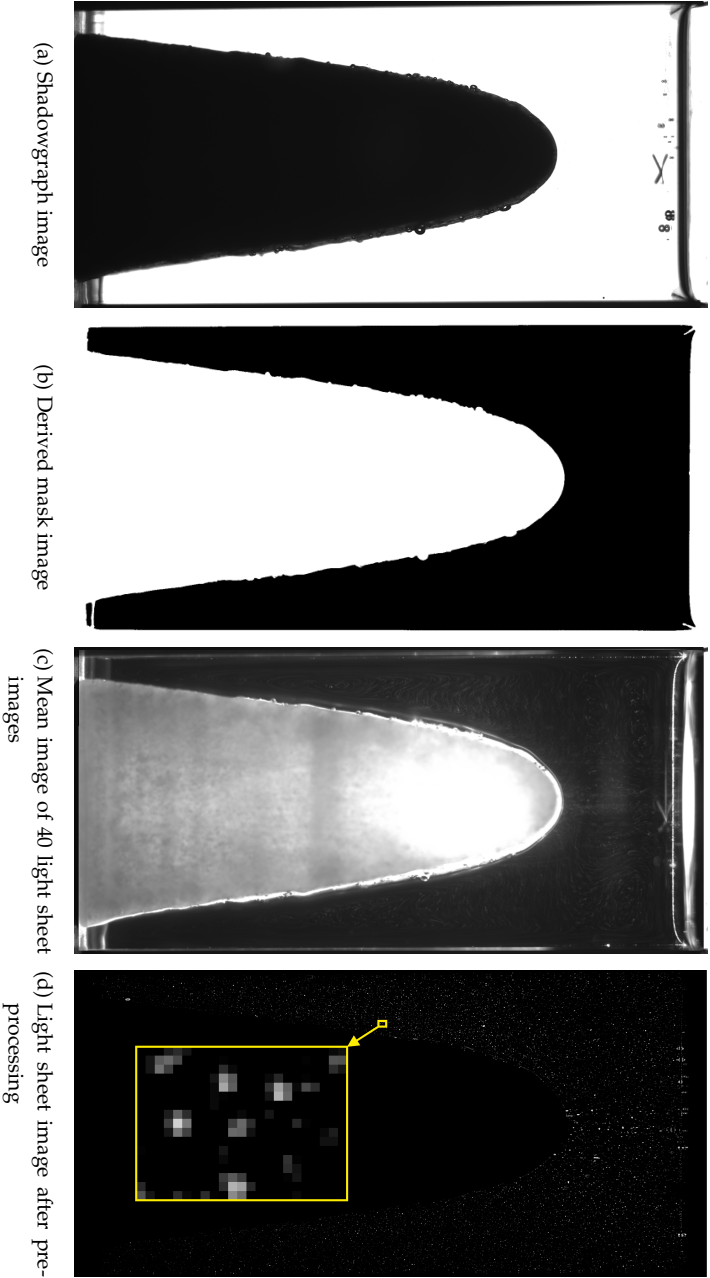


Figure 2.5: Preprocessing of light sheet images for PIV evaluation.

gation method with three passes and sub-pixel image shifting with B-spline interpolation of third order and least squares Gauss sub-pixel peak fit was done.

Finally, for validation of the resulting velocity vectors, a normalized median test and a signal-to-noise ratio test were performed to detect outliers. The detected outliers were either replaced with vectors calculated from the second largest correlation peak or interpolated from neighboring valid vectors.

A last measure to increase reliability and accuracy of the velocity data was to evaluate all the 39 image pairs out of the 40 recorded single images over 10 s and then calculate the average velocity. This filters remaining outliers or false measurements and does not significantly change the solution of the quasi-steady flow field.

2.3.3 Thermocouple measurements in the PCM

Temperatures during the melting process were measured with K-type thermocouples of 0.35 mm diameter at three distinct points $T_{\text{PCM},1}$, $T_{\text{PCM},2}$ and $T_{\text{PCM},3}$ in the test volume, as illustrated in Figure 2.2. The thermocouples passed through the heating plates from the back side and lied horizontally in the PCM. The positions of the tips of the thermocouples, where the temperatures were measured, are given in Table 2.4 with respect to the coordinate system shown in Figure 2.2.

Table 2.4: Measurement positions of thermocouples in the PCM used to measure temperatures during the melting process.

Thermocouple →	PCM,1	PCM,2	PCM,3
x -coordinate / mm	5	15	25
y -coordinate / mm	90	50	10
z -coordinate / mm	25	25	25

2.4 Results and discussion

Several test runs were successfully conducted and evaluated with the previously presented validation experiment using the described measurement techniques. Experiments with three different driving temperature differences

of $\Delta T = 5\text{ K}$, 10 K and 20 K were performed. The corresponding dimensionless numbers were already given in section 2.2.4. The melting process in the experiment with $\Delta T = 10\text{ K}$ is visualized showing the phase state and velocity vectors in section 2.4.1. This experiment was also repeated four times as similar as possible to check reproducibility and to calculate statistical errors. After performing an error assessment in section 2.4.2 and analyzing the actually measured boundary temperatures in section 2.4.3, the quantitative results of liquid phase fractions, velocity extrema and temperatures are presented in section 2.4.4.

The experimental data were stored on two different hard drives that are associated to this thesis. The measurement raw data are found in the folder `\DATA_B\Versuchsstand\Daten\MK2\`. The evaluated data are stored in the folder `\DATA_A\Evaluation\experiment\`. There are different measurement sets named after the date they were recorded. The measurement data sets evaluated in this thesis are given in Table 2.5.

Table 2.5: Measurement data sets used for evaluation.

ΔT	Data set
10 K	20170816
	20170822
	20170825
	20170831
5 K	20170905
20 K	20170922

2.4.1 Visualization of the transient melting process

The transient melting process is visualized in Figure 2.6 at time $t = 1800\text{ s}$ and in Figure 2.7 at time $t = 3600\text{ s}$ showing the average of 40 light sheet images taken over 10 s in the background. The solid phase of the PCM appears in white and light grey shades and the liquid phase in black. On top of that, the evaluated velocities are shown with vectors colored by velocity magnitude. The continuing melting process is further visualized in Figure 2.8 at $t = 5400\text{ s}$ and in Figure 2.9 at $t = 7200\text{ s}$. But in these figures shadowgraph images are shown in the background, where the solid phase appears in black and the liquid phase in white.

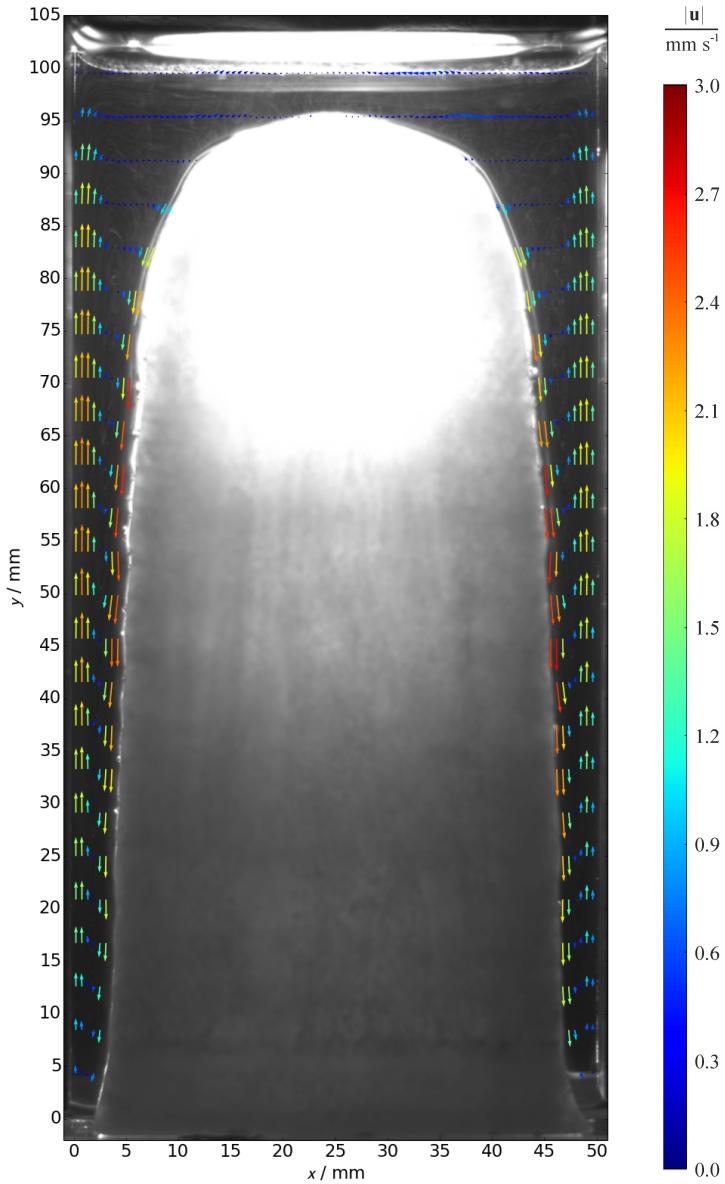


Figure 2.6: Visualization of the phase state with averaged light sheet images and the velocities in the liquid phase with colored vectors at $t = 1800$ s.

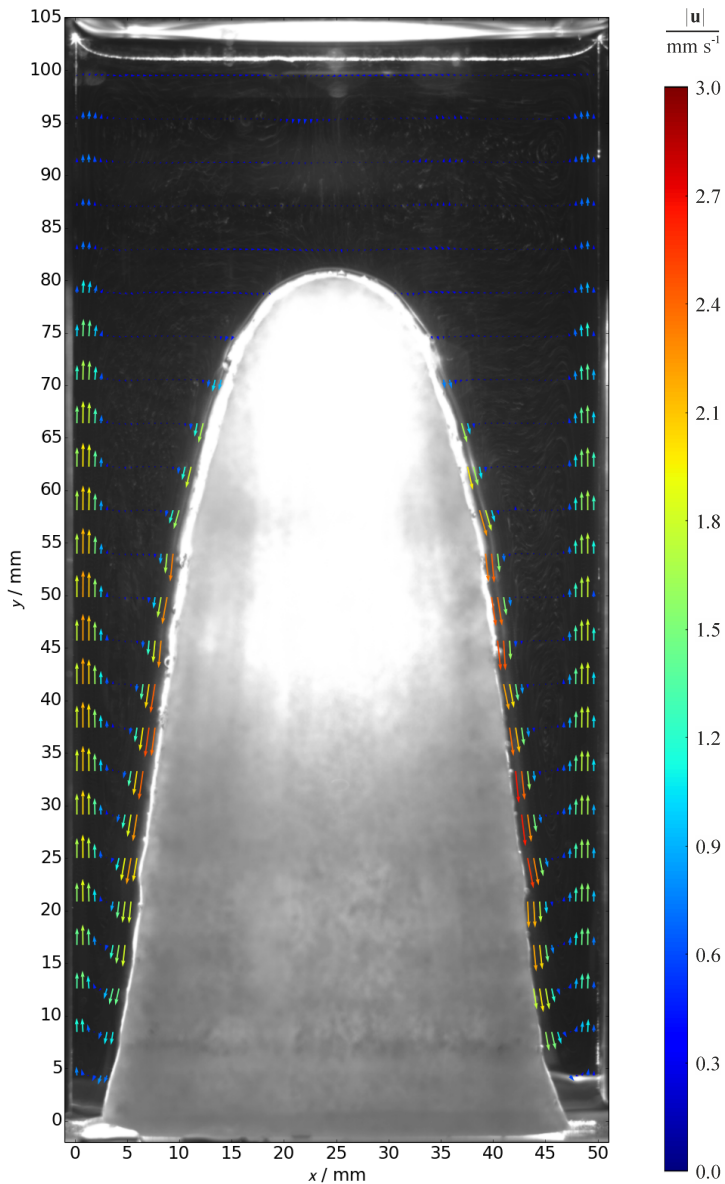


Figure 2.7: Visualization of the phase state with averaged light sheet images and the velocities in the liquid phase with colored vectors at $t = 3600$ s.

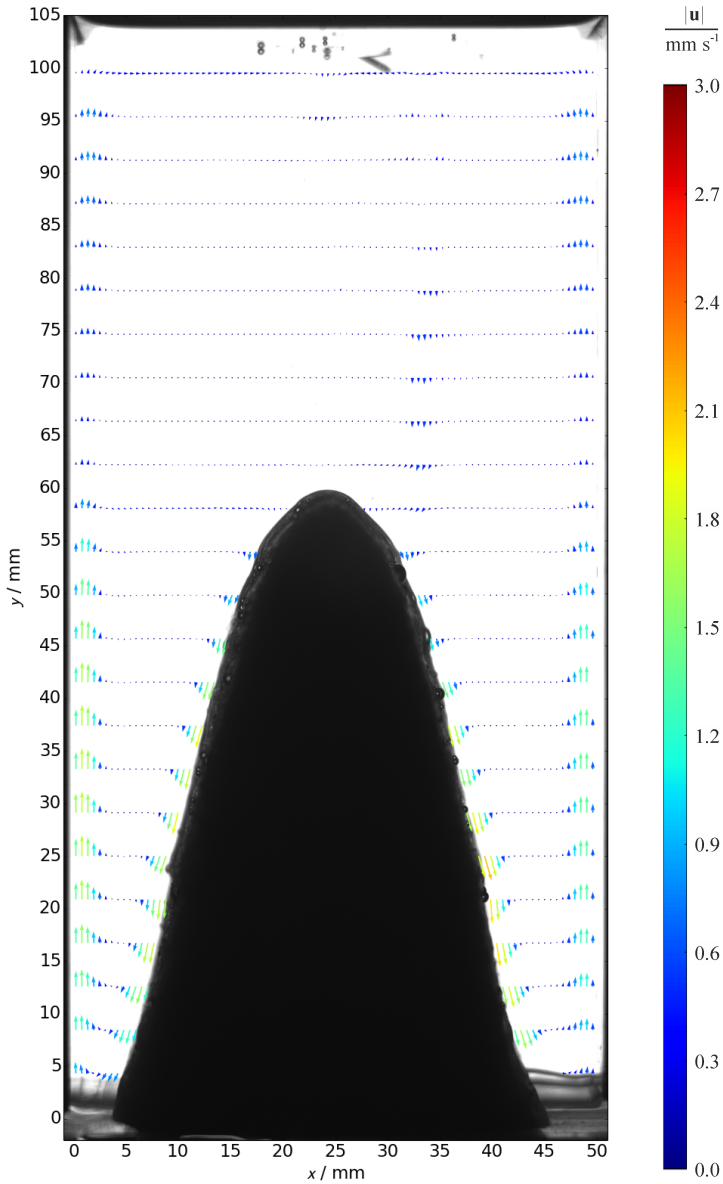


Figure 2.8: Visualization of the phase state with back light images and the velocities in the liquid phase with colored vectors at $t = 5400$ s.

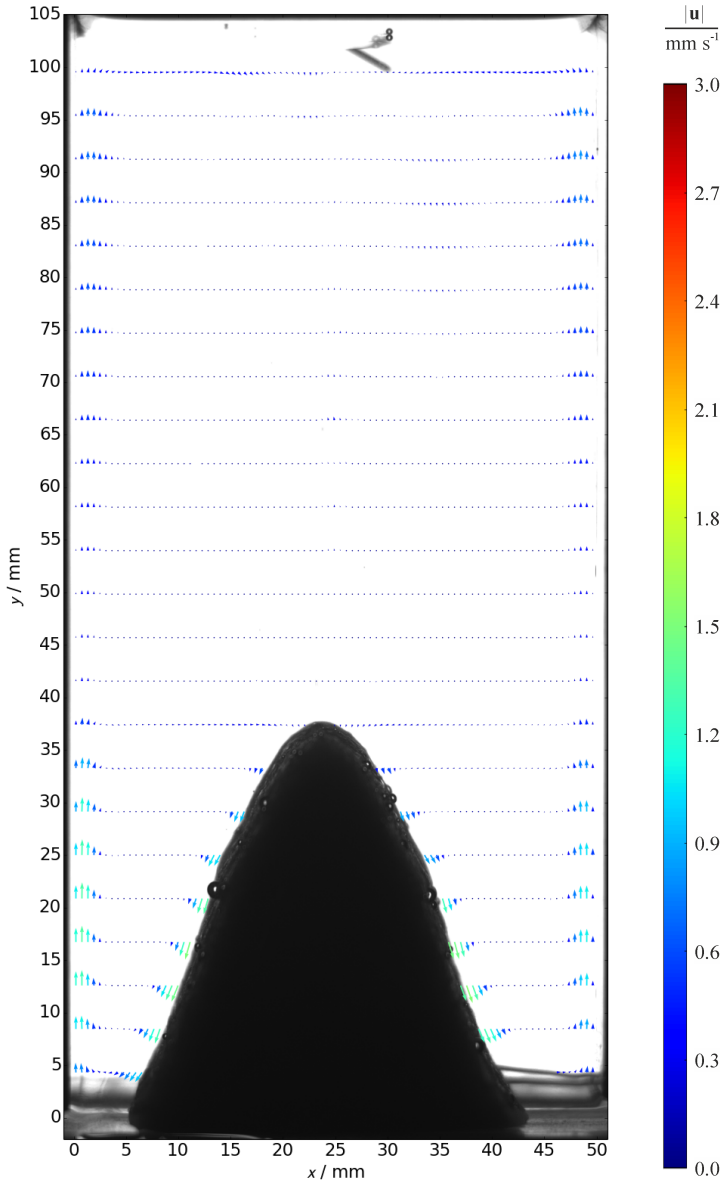


Figure 2.9: Visualization of the phase state with back light images and the velocities in the liquid phase with colored vectors at $t = 7200$ s.

Melting was dominated by natural convection in evidence of the curved phase front shape. Melting by heat conduction would occur with a phase front parallel to the heated walls. But thermal stratification due to natural convection led to increased melting at the top. The boundary layer of the upward flow at the heated walls and the boundary layer of the inclined downward flow at the colder solid phase were clearly observed. The maximum velocity magnitudes were larger in the downward flow at the cold solid phase as in the upward flow at the heated plates.

Furthermore, the maximum velocity magnitudes were larger at the left wall than at the right wall. At first sight, this is unexpected regarding the symmetry of the problem. But in an experiment a perfect symmetry cannot be ensured, either. The temperature of the heated wall on the left side was probably higher than on the right side. Although both plates were controlled to the same temperature, measurement uncertainties could have allowed slightly different temperatures. Conclusively, already a small temperature difference may lead to a visible asymmetry in the flow field. Nevertheless, the phase front remained symmetric and therefore the flow field asymmetry seemed to have only a minor impact on the melting process.

During melting, gas bubbles originated from the solid material and rose to the top surface. The filling of the PCM in many layers with subsequent solidification reduced the amount of cavities in the solid, but it could not prevent them completely. Fortunately, the rising bubbles did not significantly decrease the PIV measurement accuracy, because their velocities were out of the range captured by PIV evaluation. However, the rising gas bubbles probably entrained fluid along and could thus have adversely affected the ideally stated melting problem. To completely prevent cavities in the solid, the PCM would have to be solidified in a vacuum environment, so that no air can diffuse into the cavities formed by shrinking of the solid during solidification. Nevertheless, the formation of shrinkage cavities is a natural phenomenon that also occurs in real latent heat storage systems.

In conclusion, due to highly resolved velocities from PIV measurements, the whole flow field was visualized, which gave detailed insight into the process of natural convection during melting of a PCM.

2.4.2 Measurement and evaluation errors

The estimation of systematic and statistical measurement errors is crucial to judge measurement accuracy. Errors were analyzed for the measurement of the phase state by shadowgraphy, the measurement of velocity by PIV and the measurement of temperatures by thermocouples. The aim was to include the most important systematic error sources. To gain statistical errors, the same experiment was repeated four times.

Liquid phase fraction measurement

The liquid phase fraction, which is a dimensionless value $0 \leq f_l \leq 1$, was obtained from the shadowgraph images, as explained in section 2.3.1. The systematic errors were mainly caused by optical distortions, perspective and obstacles in the optical path, e.g. thermocouples. These errors were assumed to be well below two percent, which led to an absolute error range of ± 0.02 .

The statistical analysis of four repeated measurements of the liquid phase fraction over 11 700 s at 19 time steps of 600 s revealed 95 % confidence intervals with a size of ± 0.0066 and ± 0.034 . Conclusively, the total systematic and statistical errors were between ± 0.027 and ± 0.054 .

Velocity measurement and PIV evaluation

The velocity was measured by optical imaging of particle movement illuminated by a light sheet and optical imaging to a camera sensor. The data was evaluated by a PIV software. The following possible systematic measurement and evaluation errors were identified: 1) distortions in the optical imaging and calibration procedure from image to physical space, 2) long exposure motion blur of particle images, 3) particle inertia or sinking of particles due to density mismatch with the fluid and 4) the PIV evaluation algorithms.

As stated by Adrian and Westerweel [40], distortion errors are often negligibly small. Since there were no curved surfaces in the optical path and the focal length of the camera lens was not exceptionally wide, distortion errors were neglected. The calibration from the image to physical space was done by measuring the known physical distance of 100 mm on a calibration target in pixel values. Assuming this distance was measured with a precision of 10 pixels, the total error in the conversion factor was 0.1 pixel /mm. This induced an error of $\pm 1.7 \cdot 10^{-2}$ mm/s on the maximum velocity with magnitude $|\mathbf{u}| = 3$ mm/s.

The exposure time of the light source was selected in that manner that a particle only traveled a maximum distance of one pixel during exposure to avoid excessive motion blur. Nevertheless, the resulting error was estimated to be ± 0.1 mm/s.

As described in section 2.3.2, the Stokes number for the tracer particles in the fluid was $St = 2 \cdot 10^{-6}$, which indicated negligible dynamic tracing error. But the small static sinking velocity of $U_g = -5 \cdot 10^{-3}$ mm/s was still included in the systematic error.

As stated by Adrian and Westerweel [40], the PIV evaluation error is mostly between 0.1 and 0.2 pixels. In this study, a value of 0.2 pixels is assumed. However, due to averaging of velocities from 39 evaluations of 40 subsequent images, this value could be reduced to 0.03 pixels. Converted to physical space, this corresponded to a velocity error of $\pm 7 \cdot 10^{-3}$ mm/s.

The sum of the systematic errors was ± 0.15 mm/s. The statistical analysis of four repeated measurements of the maximum and minimum velocities in x - and y -direction over 11 400 s at 19 time steps with a step size of 600 s revealed confidence intervals between ± 0.02 mm/s and ± 0.2 mm/s in x -direction and between ± 0.05 mm/s and ± 0.7 mm/s in y -direction. The resulting sums of systematic and statistical errors lay between ± 0.2 mm/s and ± 0.4 mm/s in x -direction and between ± 0.2 mm/s and ± 0.5 mm/s in y -direction.

Temperature measurement

The thermocouples of type K used for measuring temperatures had a specified absolute accuracy of ± 1.5 K. However, the phase change temperature of three different materials was measured with multiple thermocouples with a deviation below 0.5 K. Furthermore, temperature measurements from all the installed thermocouples lay within 0.1 K in thermal equilibrium. In conclusion, the systematic measurement error was at most ± 0.5 K.

The statistical analysis of three repeated measurements of temperatures at 40 time steps over 12 000 s with a step of 300 s revealed confidence intervals between ± 0.005 K and ± 6.6 K. The larger confidence intervals only occurred over a short period of time during melting in the vicinity of the thermocouple, which resulted in a large temperature gradient and therefore a large variation between measurements. Most of the time, the confidence interval was much smaller. The resulting sums of systematic and statistical errors lay between ± 0.5 K and ± 7.1 K.

2.4.3 Measured boundary conditions

In the test case definition in section 2.2.1, ideal boundary conditions were specified. The initial temperature was $T_0 = 27^\circ\text{C}$ and the wall temperature was raised to $T_w = 38^\circ\text{C}$ at time $t_0 = 0$ s. All non-heated walls would have to be adiabatic in the ideal case. However, these ideal conditions could not be perfectly realized in an experiment. To analyze the experimental boundary conditions, temperatures were measured at all the different boundaries during the melting experiment and the heat loss and gain were roughly estimated.

Boundary temperatures

The wall temperatures at three different heights of one of the heating plates measured during a melting experiment are shown in Figure 2.10. The measurement positions can be found in Figure 2.2. Every plotted value is a mean value from four repeated measurements. The temperature in the middle was used for PID-control and therefore settled at the designated temperature of $T_w = 38^\circ\text{C}$ after a short overshoot. The time average of this middle temperature was also about $\bar{T}_{w,\text{middle}} \approx 38^\circ\text{C}$.

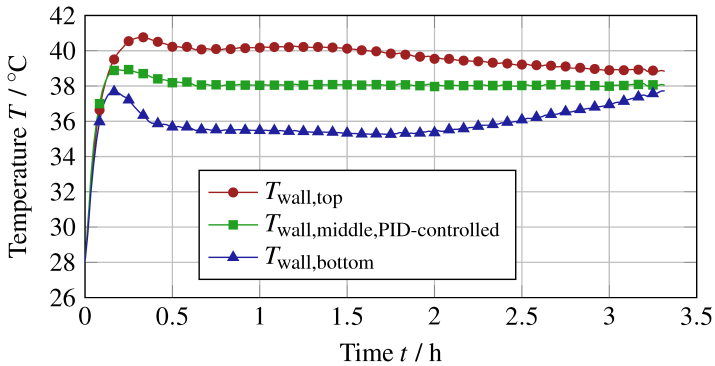


Figure 2.10: Temperatures measured during a melting experiment at the top, middle and bottom of one of the heated side walls. The temperature at the middle location was used for PID-control of the wall temperature.

The thermal stratification in the PCM due to natural convection and the finite thermal conductivity of the stainless steel heating plates, which was still about 100 times higher than that of the liquid PCM, lead to a temperature variation over the height of the heated wall. The variation over time mainly depended on the heat transfer rate from the heater into the PCM. During the melting process with strong natural convection, the heating plates could not compensate the thermal stratification in the PCM. Only in the pure conduction regime at the very beginning and after completed melting at the end, the heating plates had a uniform temperature over the height. The time averaged value of the top temperature was $\bar{T}_{w,top} = 39.5^\circ\text{C}$ and that of the bottom temperature was $\bar{T}_{w,bottom} = 35.9^\circ\text{C}$.

This temperature variation over the height was clearly a deviation of the experiment from the originally stated ideal case. But the impact on the results has yet to be analyzed, e.g. in a numerical comparison study of ideal and real wall boundary conditions. Nevertheless, the mean values of the time-averaged temperatures at the three height levels was $\bar{T}_w = 37.8^\circ\text{C}$, which is close to the designated $T_w = 38^\circ\text{C}$ and therefore ensured the ideal wall temperature in a mean sense.

The temperatures measured at six locations of the remaining quasi-adiabatic walls are shown in Figure 2.11; for the locations refer to Figure 2.2. At one of the side walls, temperatures were measured at an upper and a lower location both in the PCM at the inside of the enclosure and in the air at the outside of the enclosure. Also, air temperatures were measured above the enclosure at the lid window and directly below the enclosure.

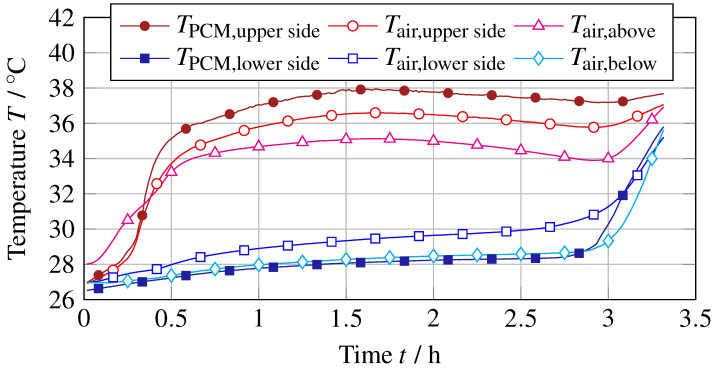


Figure 2.11: Temperatures measured at six locations of the quasi-adiabatic walls.

At the upper position of the enclosure side wall, the temperature in the air is lower than that in the PCM. At the lower position of the enclosure side wall, the temperature in the air is higher than that in the PCM. This is due to the control algorithm which controls both air temperatures to both PCM temperatures in a mean sense. Since the air has different material properties than the PCM, the thermal stratification is different in both materials and a better agreement is not achievable. The air temperature above the enclosure was not actively controlled and is a result of this control strategy. It is lower than the air temperature at the side, because the enclosure side walls are also heated by the main heaters and, as a result, the air heaters lower their power to not introduce too much heat. Together with heat losses at the top, this results in a lower air temperature above the PCM enclosure. The air temperature below the enclosure matches the PCM temperature at the lower position. The air volume below the enclosure can be well controlled, because it is separated and insulated from the rest of the air in the outer enclosure.

Conclusively, we can see that the quasi-adiabatic control strategy leads to low differences between air and PCM temperatures at the enclosure boundaries.

Boundary heat loss and gain

To estimate the influence of the remaining heat flow over the quasi-adiabatic boundaries on the melting process, the heat flow rates through the boundaries were estimated and compared to the power of the heating plates that heat up the PCM.

The heat flow rates at the three different boundaries (below, sides and above) were approximately calculated from the difference of the measured temperatures between the PCM and the surrounding air shown in Figure 2.11. For the sides and bottom boundaries, heat conduction through the enclosure walls is calculated. An enhanced thermal conductivity model with a Nusselt correlation [41] was used to calculate natural convection in the air layer above the PCM. Heat radiation through this air layer is also approximately calculated. All the boundary heat flow rates were summed up to obtain a total boundary heat flow rate. For comparison, the heat flow rate that is transferred by the heating plates into the PCM was approximately calculated by the power rating of the heaters and the duty cycle of the PWM signal.

The result is that in total, relative to the heating power, 3.4 % of heat was lost and 1.9 % was gained through the boundaries. This confirms a minor influence of

the boundaries on the melting process and with it the effectiveness of the quasi-adiabatic control of boundary temperatures.

2.4.4 Quantitative results for validation

Finally, the quantitative results for the purpose of numerical model validation are presented. The relevant quantities are the liquid phase fraction, the velocities in the liquid phase of the PCM and the temperatures at distinct positions in the PCM.

Liquid phase fractions over time

The liquid phase fractions were calculated from shadowgraph images taken every 60 s during the experiment, see section 2.3.1. The temporal evolutions of liquid phase fractions for three different experiments with driving temperature differences $\Delta T = 5$ K, 10 K and 20 K are plotted in Figure 2.12. For the experiment with $\Delta T = 10$ K, error bars are given. They show the sum of the systematic error and the statistical confidence interval from four repeated measurements at selected times, as calculated in section 2.4.2.

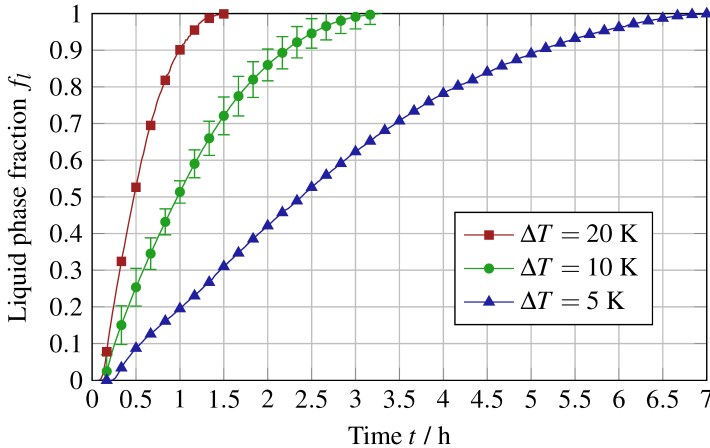


Figure 2.12: Liquid phase fractions over time of three different experiments with driving temperature differences $\Delta T = 5$ K, 10 K and 20 K.

The curves show a usual shape with a rate of melting that increases with the driving temperature difference more than proportional. The melting times were $t_m(\Delta T = 20 \text{ K}) = 5460 \text{ s}$, $t_m(\Delta T = 10 \text{ K}) = 11880 \text{ s}$ and $t_m(\Delta T = 5 \text{ K}) = 25560 \text{ s}$.

Velocity extrema over time

The full velocity field, as illustrated in figures 2.6-2.9, contains many data points and is hard to quantify. Therefore, the maximum and minimum velocities in both the x - and y - direction are evaluated. The results are plotted over time in Figure 2.13. Error bars show again the sum of the systematic error and the statistical confidence interval from four repeated measurements at selected times calculated in section 2.4.2.

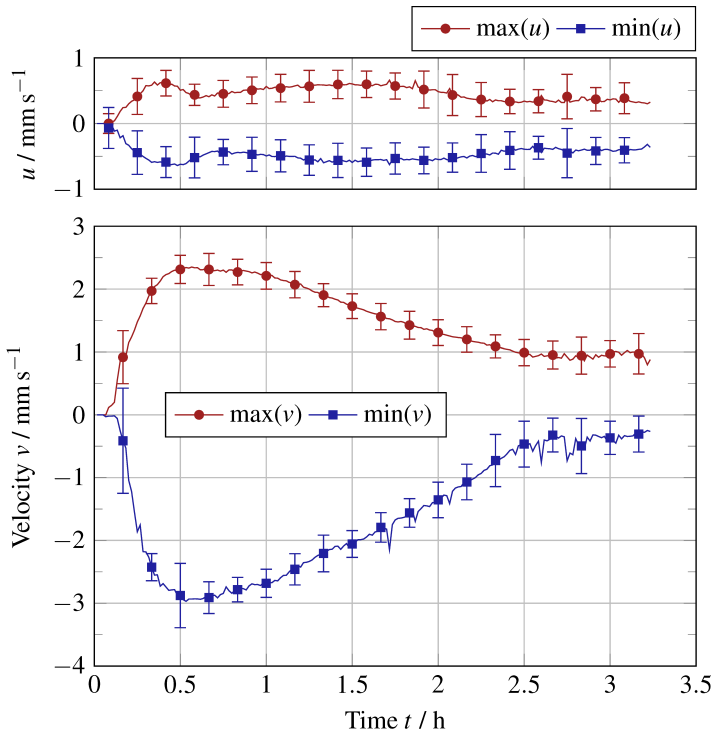


Figure 2.13: Maximum and minimum velocities in x - and y - direction over time of the experiment with $\Delta T = 10 \text{ K}$.

It is clearly seen that vertical velocities v in y -direction are significantly larger than horizontal velocities u in x -direction. This is expected, because the buoyancy force acts in y -direction at the walls and in negative y -direction at the phase boundary. Furthermore, the maximum velocity $\max(u)$ and the minimum velocity $\min(u)$ in x -direction are similar in magnitude. However, in the y -direction, the maximum velocity $\max(v)$ is about 20% lower in magnitude than the minimum velocity $\min(v)$.

PCM Temperatures

The temperatures inside the PCM $T_{\text{PCM},1}$, $T_{\text{PCM},2}$ and $T_{\text{PCM},3}$ at the three distinct measurement positions, see Figure 2.2, are plotted in Figure 2.14.

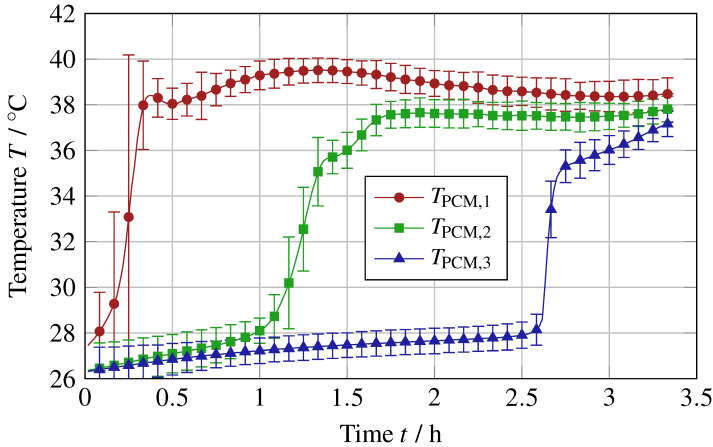


Figure 2.14: Temperatures in the PCM over time of the experiment with $\Delta T = 10$ K at three distinct measurement positions.

Error bars show the sum of the systematic error and the statistical confidence interval from four repeated measurements at selected times, as calculated in section 2.4.2. The error is larger at high temperature gradients due to larger deviations of repeated measurements. The time when the melting front passed the thermocouple, which led to a rapid increase in temperature, could not exactly be reproduced. The predominant remaining time, however, errors were small.

The temperature $T_{\text{PCM},1}$ slightly exceeded the wall temperature $T_w = 38^\circ\text{C}$, which was due to the non-uniformity of the heating plates seen in Figure 2.10. Apart from that, the temperatures show the typical progression expected from a phase change process.

2.5 Conclusions

A novel validation test case for a LHS system with symmetric heating from two opposite vertical side walls was defined. An experimental test bench was built and measurement techniques for phase state, velocities and temperatures were implemented.

Three main challenges of such an experiment were identified. The first was that the heating plates may not conduct heat well enough and, due to the thermal stratification in the PCM, establish a temperature variation over the height. The significance of this problem still has to be investigated in further studies. Since the temperatures were provided at three positions over the height and with time, this boundary condition may be easily implemented in a simulation. The second challenge was a symmetric heating from both sides. A larger flow velocity magnitude in one of the two wall boundary layers was found. Although both plates were PID-controlled to the same temperature, measurement uncertainties could allow slightly different temperatures. The conclusion is that already a small temperature difference may lead to a visible asymmetry in the flow field. Nevertheless, the phase front remained symmetric and therefore another conclusion is that the flow field asymmetry had only a minor impact on the melting process. The third challenge was the heat flow over the remaining ideally adiabatic boundaries, which could affect the melting process. The heat flow rates over the boundaries were minimized with an active quasi-adiabatic control approach of trace heaters in a surrounding air chamber. The remaining total heat loss was estimated to be 3.4% and the heat gain 1.9% relative to the heat transferred by the heating plates. In conclusion, there was only a minor effect of heat transfer through the boundaries in this experiment.

The main results are measurements of the phase state and velocities in the liquid phase of the PCM with high spatial and temporal resolution. The optical measurement techniques of shadowgraphy and PIV produced highly resolved data on the phase state and velocity in a two-dimensional vertical plane. With an automated measurement technique, approximately 200 measurement sets were

taken in every experiment to obtain a temporal resolution of the whole melting process. Each measurement set included a shadowgraph image and a series of 40 lightsheet images over 10 s to obtain transient and averaged velocity data. An error analysis was performed including estimated systematic errors and statistical measurement errors calculated from four repeated experiments. The resulting error bars of liquid phase fraction, velocities and temperatures were sufficiently low and confirmed accurate results. These comprehensive data are suitable for validation of numerical models for phase change processes.

Chapter 3

Numerical modeling and validation

This chapter is about numerical modeling and model validation based on the experiment introduced in chapter 2. Two different modeling approaches, a detailed and a simplified one, implemented within the same solver framework ANSYS Fluent, are presented. As a first step, a comparison of the models with each other is shown. In a second step, a comparison of simulation results to the validation experiment is presented. But first of all, the state of the art on the numerical models is discussed.

3.1 State of research and objectives

Numerical models for solid liquid phase change with natural convection have been researched for more than thirty years with one of the first works being by Voller et al. [42]. Most of the existing models were collected in the reviews by Salcudean and Abdullah [43], Samarskii et al. [13], Voller [15], Hu and Argyropoulos [14], Dutil et al. [16] and Dhaidan et al. [17]. The models were roughly divided in deforming grid and fixed grid methods and a comparison of these approaches was done by Lacroix and Voller [44], and Viswanath and Jaluria [45]. The variables were either formulated in primitive variables, such as pressure and velocity, or in a stream function and vorticity approach [13]. In the fixed grid methods with primitive variables, the enthalpy-porosity technique by Voller and Prakash [46], Brent et al. [47] or Voller and Swaminathan [48] has often been used for phase change and the incompressible Navier-Stokes equations have been solved with a projection method to decouple the computation of pressure and velocity. Semi-implicit projection methods such as the SIMPLE

algorithm by Patankar and Spalding [49] have been used by most researchers, but also explicit projection methods [50] were applied by Galione et al. [51] and Kozak and Ziskind [52]. Mostly, the Boussinesq approximation has been applied, which sets a constant density in all terms of the governing equations but the buoyancy term in the momentum equations, where the dependency of density with temperature is linearized. A variable PCM density was implemented in conjunction with an air phase and the volume of fluid (VOF) method [53] to model volume expansion [54–56]. However, the impact of variable material properties and volume expansion on melting governed by natural convection in latent heat storage is not known, since the results of a detailed VOF approach and a simplified Boussinesq approximation have not yet been compared.

The weak natural convection during solidification was also approximately modeled with a heat conduction model with enhanced thermal conductivity (ETC) approach by Farid and Husian [57]. Several solutions from different heat conduction phase change models with enhanced thermal conductivity were compared to each other and to experimental data by Pointner et al. [58], where good agreement was found. However, during melting and when natural convection is strong, the phase change process becomes highly two-dimensional and the standard enhanced thermal conductivity methods are not valid. In this case, only the aforementioned natural convection models including fluid flow are accurate enough.

Despite the impressive amount and level of sophistication of available numerical models, their verification and validation are still remaining issues. Different methods have been producing deviating results [59] and the agreement of numerical results with experiments has often not been satisfactory in the past, as stated by Kadri et al. [18]. To give an example on the issue of verification: Bertrand et al. [60] and Gobin and Le Quéré [61] performed a thorough comparison of multiple well-designed models on a numerical benchmark test case. Although results indicated the same trends, the phase boundary differed up to $\pm 20\%$ in one of the test cases. To give another example on the issue of validation: Campbell and Koster [28] repeated the most popular validation test case, which was performed by Gau and Viskanta [25], with an improved experimental setup. Although the phase front shapes of the simulation and experiment were similar in the final steady state, deviations were found during the temporal evolution.

Conclusively, verification and validation have been a challenging task. The problem is that there is a general lack of experiments suitable for validation of

melting governed by natural convection [18]. The novel validation experiment presented in the last chapter contributes to increasing the amount of available experiments and the resolution of measurements. The remaining task is the comparison and validation of numerical models with these experimental data.

3.2 Numerical modeling

Two different numerical models with varying degree of detail and different simplifications were developed. The models were based on the commercial software package ANSYS Fluent, where the Navier-Stokes equations including the energy equation and a source term enthalpy method were solved on a fixed finite volume grid in two dimensions [62, 63]. A first detailed model (V-2D) used variable material properties and the volume of fluid (VOF) method to model volume expansion of the PCM into an additional air phase. A second simplified model (B-2D) used the Boussinesq approximation and constant material properties and thereby neglected volume expansion.

3.2.1 Model simplifications

The following simplifications were used by both models: 1) the flow in the liquid phase of the PCM was incompressible and Newtonian, 2) the sharp interface between the solid and liquid phase of the pure PCM or eutectic mixture of multiple PCMs could be represented by a narrow so called mushy region, where the material was neither solid nor liquid but a mixture of both phases, 3) the solid phase did not move – no sinking of the solid phase or close contact melting occurred, 4) natural convection in the PCM was laminar and 5) radiation and viscous dissipation were negligible.

There are further simplifications that were different for the two models. The detailed model (V-2D) introduced an interface between the PCM and an air phase to allow for volume expansion. However, it was assumed that 6) the effect of surface tension on the interface between liquid PCM and air was negligible. The simplified model (B-2D) used a constant density and the Boussinesq approximation in the buoyancy term and therefore assumed that 7) this approximation was valid and density change (or volume expansion) of the PCM during melting was negligible. Furthermore, this model assumed that 8) constant thermophysical properties of the PCM were sufficiently accurate.

3.2.2 Modeling of material properties

The density, specific heat capacity, thermal conductivity and dynamic viscosity of the PCM n-octadecane are already given in Table 2.2. The different modeling of these material properties in the detailed model (V-2D) and in the simplified model (B-2D) is compared in Table 3.1. These material properties are also visualized over temperature in Figure 3.1. The variable properties used by the detailed model (V-2D) are shown with solid lines and the constant properties used by the simplified model (B-2D) are represented with dashed lines.

Table 3.1: Modeling of material properties in the detailed model (V-2D) and in the simplified model (B-2D).

Property	V-2D	B-2D
Density ρ	$\rho(f_l, T)$	$\bar{\rho}$
Spec. heat cap. c_p	$c_p(T)$	\bar{c}_p
Therm. cond. k	$k(f_l, T)$	k_l
Dyn. viscosity μ	$\mu(T)$	$\mu(T_m + \frac{\Delta T}{2})$

In the detailed model (V-2D) the density was constant in the solid state and during phase change it linearly varied with the liquid phase fraction between the solid and liquid state:

$$\rho(f_l, T) = f_l \rho_l + (1 - f_l) \rho_s. \quad (3.1)$$

The specific heat capacity, however, could not be specified depending on the liquid phase fraction in ANSYS Fluent; it had to depend on temperature. Even with the appropriate user defined function (UDF) macro this was not possible. So, a small temperature range was introduced in the phase change region between the solidus temperature $T_s = T_m - 0.1$ K and the liquidus temperature $T_l = T_m + 0.1$ K, in which the specific heat capacity changed linearly:

$$c_p(T) = c_{p,s} + \frac{c_{p,l} - c_{p,s}}{T_l - T_s} (T - T_s). \quad (3.2)$$

The thermal conductivity was constant in the solid state and during phase change it depended on the liquid phase fraction

$$k(f_l, T) = f_l k_l + (1 - f_l) k_s. \quad (3.3)$$

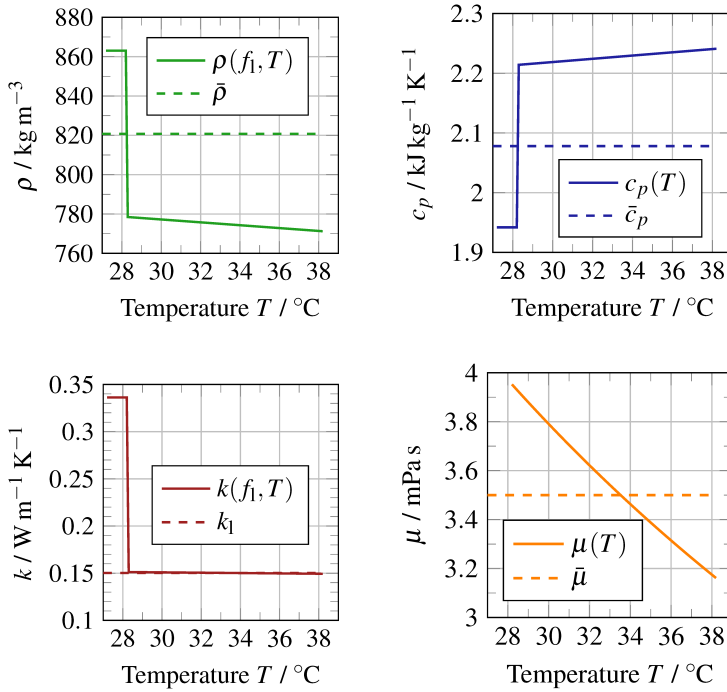


Figure 3.1: The density ρ , specific heat capacity c_p , thermal conductivity k and dynamic viscosity μ of n-octadecane over temperature with solid lines for variable properties used in the detailed model (V-2D) and dashed lines for constant properties used in the simplified model (B-2D).

In the liquid state, all properties ρ , c_p , k depended on temperature. The dynamic viscosity μ is only defined in the liquid state and also depended on temperature.

With the Boussinesq approximation in the simplified model (B-2D), the density was assumed constant in all terms but the linearized Buoyancy term in the momentum equation. As constant mean density $\bar{\rho}$, the mean value of the liquid and the solid state near the melting point was chosen. From a fluid dynamics viewpoint, the density in the liquid state would have been the optimal choice, because the melting process is dominated by natural convection in the liquid phase. However, the amount of sensible and latent energy stored in the initial solid state would have been much lower than in reality. With a mean density $\bar{\rho}$ and a mean PCM volume, the amount of stored energy was correct in a mean sense. For the same reason, a mean specific heat capacity c_p was selected. For the thermal conductivity k , the value in the liquid state was chosen, because temperature gradients and heat conduction mostly occurred in the liquid phase while the solid phase was nearly isothermal throughout the melting process. The dynamic viscosity was set to a constant value evaluated at the mean liquid temperature $T_m + \frac{\Delta T}{2}$.

3.2.3 Governing equations

For the two different models, different sets of governing equations were needed. The detailed model (V-2D) maintained a variable density and used the VOF method and an additional air phase for volume expansion while the simplified model (B-2D) assumed a constant density and included buoyancy with the Boussinesq approximation.

Detailed VOF model with air phase (V-2D)

The conservation equations of mass, momentum and energy are solved with one set of equations for the two phases of PCM and air with the volume of fluid method: The continuity equation is thereby solved only for the secondary phase, which is the PCM:

$$\frac{1}{\bar{\rho}} \left[\frac{\partial}{\partial t} (\alpha_{\text{PCM}} \rho) + \nabla (\alpha_{\text{PCM}} \rho \mathbf{u}) = \dot{m}_{\text{air} \rightarrow \text{PCM}} - \dot{m}_{\text{PCM} \rightarrow \text{air}} \right], \quad (3.4)$$

where α_{PCM} is the volume fraction of the PCM, ρ is the density and $\mathbf{u} = (u, v, w)^\top$ is the flow velocity in x , y and z -direction, respectively. The volume fraction of

the primary phase, which is air, is determined with the following constraint:

$$\alpha_{\text{PCM}} + \alpha_{\text{air}} = 1. \quad (3.5)$$

The momentum equation with buoyancy term \mathbf{F}_b and a momentum source term \mathbf{S}_u is

$$\frac{\partial}{\partial t}(\rho \mathbf{u}) + \nabla \cdot (\rho \mathbf{u} \mathbf{u}^\top) = \nabla \cdot \boldsymbol{\tau} - \nabla p + \mathbf{F}_b + \mathbf{S}_u, \quad (3.6)$$

where p is the pressure. The stress tensor $\boldsymbol{\tau}$ is given as

$$\boldsymbol{\tau} = \mu \left[(\nabla \mathbf{u} + \nabla \mathbf{u}^\top) - \frac{2}{3} \nabla \cdot \mathbf{u} \mathbf{I} \right], \quad (3.7)$$

where \mathbf{I} is a unit tensor. The buoyancy term is

$$\mathbf{F}_b = \rho g \hat{\mathbf{e}}_y, \quad (3.8)$$

where g is the gravity constant and $\hat{\mathbf{e}}_y$ is a unit vector in y -direction.

The energy equation for the specific enthalpy h with an enthalpy source term S_h is

$$\frac{\partial}{\partial t}(\rho h) + \nabla \cdot (\rho \mathbf{u} h) - \nabla \cdot (k \nabla T) = S_h. \quad (3.9)$$

Simplified Boussinesq model (B-2D)

The conservation equations of mass, momentum and energy are solved without volume expansion with the Boussinesq approximation: With constant density, the continuity equation reduces to

$$\nabla \cdot \mathbf{u} = 0. \quad (3.10)$$

The momentum equation with buoyancy term \mathbf{F}_b and momentum source term \mathbf{S}_u is

$$\bar{\rho} \frac{\partial \mathbf{u}}{\partial t} + \bar{\rho} (\mathbf{u} \cdot \nabla) \mathbf{u} = \mu \nabla^2 \mathbf{u} - \nabla p + \mathbf{F}_b + \mathbf{S}_u, \quad (3.11)$$

where $\bar{\rho}$ is the constant mean density defined in section 3.2.2. With the Boussinesq approximation, the Buoyancy term is

$$\mathbf{F}_b = g \bar{\rho} \beta (T - T_m) \hat{\mathbf{e}}_y. \quad (3.12)$$

The buoyancy depends on the thermal expansion coefficient β and a temperature difference to a reference temperature, at which the constant density was specified. In this case this is the melting temperature T_m .

The energy equation for the specific enthalpy h with an enthalpy source term S_h is

$$\bar{\rho} \frac{\partial h}{\partial t} + \bar{\rho} \nabla \cdot (\mathbf{u} h) - \nabla \cdot (k \nabla T) = S_h. \quad (3.13)$$

Enthalpy-Porosity method (V-2D, B-2D)

The energy equation, either Equation 3.9 or Equation 3.13, is transformed with the enthalpy-porosity method [46–48]. In the following, the more general Equation 3.9 is used. The central idea of the method is to write the enthalpy h as the sum of the sensible enthalpy h_{sens} and the latent enthalpy h_{lat} :

$$h = h_{\text{sens}} + h_{\text{lat}}. \quad (3.14)$$

The sensible enthalpy is

$$h_{\text{sens}}(T) = \int_{T_{\text{ref}}}^T c_p dT' \quad (3.15)$$

and the latent enthalpy is the product of the latent heat of fusion L and the liquid phase fraction f_1 :

$$h_{\text{lat}} = Lf_1. \quad (3.16)$$

The liquid phase fraction is in general defined by the temperature T in relation to the solidus temperature T_s and the liquidus temperature T_l :

$$f_1 = \begin{cases} 0, & T \leq T_s \\ 0 \dots 1, & T_s < T < T_l \\ 1, & T \geq T_l \end{cases}. \quad (3.17)$$

In the so called mushy region, $0 < f_1 < 1$, the material is neither solid or liquid, but in a state of melting or solidification. In this region, a relationship between liquid phase fraction and temperature has to be defined.

ANSYS Fluent offers two variations of the enthalpy-porosity technique: the melting point model [46] and the melting range model [48]. The melting point model is activated in the software, when the solidus and liquidus temperature are specified as the same value, which is the melting temperature T_m , and the melting range model is applied when a higher liquidus than solidus temperature is specified [63]. The melting range model could be also applied for a material with a melting point, when a small melting range is selected. Both models were tested and the melting point model was preferred, because it showed more plausible results and better agreement with experiments. In the melting point model [46], a linear relationship over a small temperature range of 2ζ between $T_s = T_m - \zeta$ and $T_l = T_m + \zeta$ is introduced and the liquid phase fraction is then defined as:

$$f_1 = \begin{cases} 0, & T \leq T_m - \zeta \\ \frac{T - (T_m - \zeta)}{2\zeta}, & T_m - \zeta < T < T_m + \zeta \\ 1, & T \geq T_m + \zeta \end{cases}. \quad (3.18)$$

After introducing Equation 3.14 in Equation 3.9, dropping the subscript sens, and defining the energy equation source term as

$$S_h = L\left(\frac{\partial}{\partial t}(\rho f_1) + \nabla \cdot (\rho \mathbf{u} f_1)\right), \quad (3.19)$$

the original form of the energy Equation 3.9 is obtained with the latent enthalpy being expressed in the source term:

$$\frac{\partial}{\partial t}(\rho h) + \nabla \cdot (\rho \mathbf{u} h) - \nabla \cdot (k \nabla T) = L\left(\frac{\partial}{\partial t}(\rho f_1) + \nabla \cdot (\rho \mathbf{u} f_1)\right). \quad (3.20)$$

To modify the velocities in the mushy region and in the solid [46] a source term is introduced into the momentum Equations 3.6 or 3.11,

$$\mathbf{S}_u = -B(f_1) \mathbf{u}, \quad (3.21)$$

where a parameter $B(f_1)$, which depends on the liquid phase fraction, is multiplied with the velocity vector. This parameter has to be zero in the liquid phase to allow for free motion. When it takes large values in the solid phase, the velocities are forced to near zero values in the linear system of equations of an implicit method [47]. While different functions fulfill this requirement, most often the Carman-Kozeny equation, which was derived from the D'Arcy law for fluid flow in porous media [64], is used in a modified form [63]:

$$B(f_1) = C \frac{(1 - f_1)^2}{(f_1^3 + q)}. \quad (3.22)$$

The original Carman-Kozeny equation would yield infinity if the liquid phase fraction approached zero. To limit $B(f_1)$ to numerically applicable finite values, a constant value q is additionally added in the denominator. In ANSYS Fluent, the value is fixed to $q = 1 \cdot 10^{-3}$. The parameter C is called the mushy region or mushy zone constant and is a model constant, which replaces the physical properties in the Carman-Kozeny equation. It has to be adjusted to the problem, because it influences the morphology of the mushy region [46]. Investigations on the influence of the value C were described by Shmueli et al. [55]. In this study, a standard value of $C = 1 \cdot 10^6$ was used. It was found that, using a melting point material, the solution is rather insensitive to this parameter compared to a melting range material. With a melting point material, the mushy zone is expected to be narrow, approximately as wide as a computational cell, and to exist only due to the discretization error.

3.2.4 2D domains, initial and boundary conditions (V-2D, B-2D)

The domain contained either a zone for the mixture of PCM and air in the case of the detailed model (V-2D) or a zone of pure PCM in the case of the simplified model (B-2D). Additionally, a small part of heater material with 1 mm thickness and the bottom part of the acrylic glass enclosure with 2 mm wall thickness were included in the domain. The domain only extended to half of the enclosure and the symmetry to the mid-plane was used. After comparing a simulation with full enclosure width to another simulation with half width and symmetry condition, the flow and melting was found to be indistinguishable. Although the V-2D and B-2D models were created as similar as possible, there were differences in the domain and the initial and boundary conditions. Both 2D models are shown in Figure 3.2.

The domain of the detailed model (V-2D) was slightly larger to accommodate an additional air phase on top of the PCM that allowed volume expansion of the PCM during melting. The air was assumed incompressible with constant properties. A pressure outlet allowed for the air to flow out of the domain. This boundary condition additionally needed the specification of a backflow temperature $T_{\text{bf}} = T_w$, and a backflow volume fraction for the PCM phase $\alpha_{\text{PCM,bf}} = 0$. With setting the backflow temperature higher than the PCM temperature, heat was not transferred out of the domain by convection; only a negligible conduction heat flow might have occurred into the domain. Setting the backflow volume fraction correctly was important, so that only air and not PCM could flow into the system. The initial conditions had to be patched in ANSYS Fluent, i.e. firstly the domain was initialized with setting u_0, v_0, p_0, T_0 and $\alpha_{\text{air},0} = 0$. Then only the air region was patched with setting $\alpha_{\text{air},0} = 1$.

The simplified model (B-2D) did not include an air phase for volume expansion. The height of the domain was set to the average between the liquid and the solid state and therefore was smaller than in the V-2D model. Instead, the top boundary was modeled with a symmetry boundary condition, i.e. all gradients and the velocity component in y -direction were zero. The domain was initialized with setting u_0, v_0, p_0 and T_0 .

For both these 2D models, all outer sides except the steel heater wall and the pressure outlet were adiabatic and thus heat exchange with the environment was neglected.

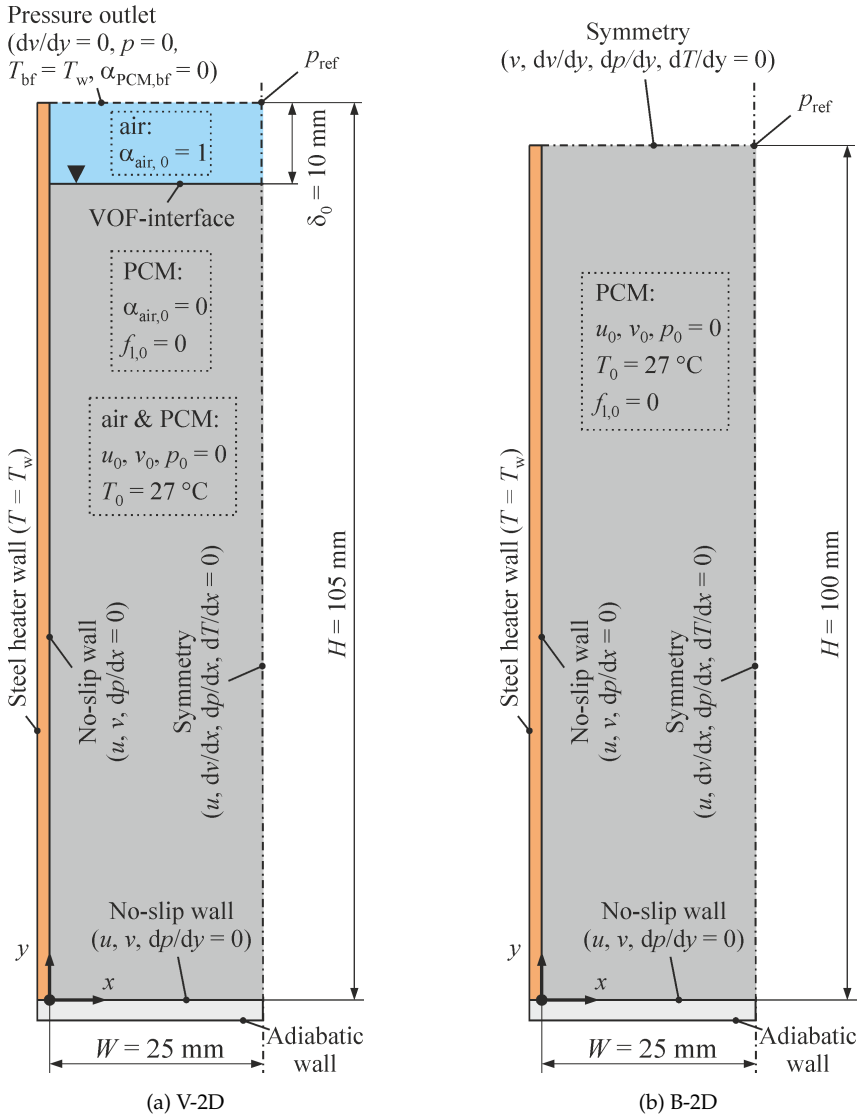


Figure 3.2: Domain and initial and boundary conditions of the detailed (V-2D) and the simplified model (B-2D).

3.2.5 3D Boussinesq model with boundary effects (B-3D)

The simplified model (B-2D) was extended to a 3D model with boundary effects (B-3D). The 3D domain had the same dimensions in the x - y -plane as the 2D domain. A second symmetry plane was used in z -direction and thus the depth was the half depth of the symmetric PCM region with $D/2 = 25$ mm. An additional acrylic glass window with a thickness of 2 mm enclosed the PCM at the back side. The domain of the B-3D model is illustrated in Figure 3.3.

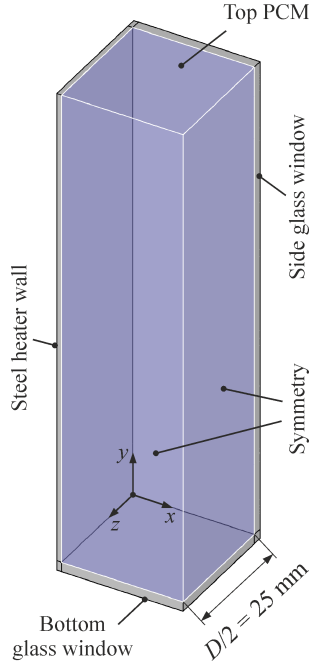


Figure 3.3: Domain of 3D Boussinesq model including viscous boundary layer effects and thermal boundary conditions.

In this 3D model, other than in the 2D models, viscous boundary layer effects of the front and back walls were included. Additionally, thermal boundary conditions were imposed with measured data from the validation experiment described in chapter 2. While a simulation cannot model all physical effects, an experiment is not able to perfectly reproduce the ideally stated physical problem with isothermal walls and adiabatic boundaries defined in section 2.2.1. With im-

posing the inevitable boundary effects of the experiment, see section 2.4.3, onto the simulation, a comparison of the simulation with the experiment free of the influence of boundary effects was possible. The thermal boundary conditions are summarized in Table 3.2.

Table 3.2: Thermal boundary conditions in the 3D model (B-3D).

Boundary	Thermal boundary condition
Steel heater wall	$T_w(t, y) = T_{w,exp}(t, y)$
Top PCM	$\dot{Q}_{top}(t) = \dot{Q}_{conv+rad}(T_{top,exp}(t))$
Bottom glass window	$T_{bottom}(t) = T_{bottom,exp}(t)$
Side glass window	$T_{side}(t, y) = T_{side,exp}(t, y)$

Firstly, two temperatures, which were experimentally measured at the heater wall $T_{w,top}$ and $T_{w,bottom}$, were interpolated over time t and height y to the simulation time and boundary mesh and then used as temperature boundary condition at the steel heater wall. Secondly, a heat flow through the top of the PCM was modeled with a mixed boundary condition in ANSYS Fluent. With this boundary condition, a heat flow by heat radiation and by natural convection in the adjacent air gap over the PCM was modeled. In the experiment, this air gap was enclosed on top with another acrylic glass plate on which the temperature $T_{air,above}$ was measured. This temperature was interpolated to the simulation time from the experimental data and set as free stream boundary temperature and external radiation temperature. The external emissivity for the radiation part was set to a value of 0.9. The heat transfer coefficient for the convective part was calculated with an approximate enhanced thermal conductivity model for natural convection in an air enclosure [41]. Thirdly, heat flow through the side and bottom glass windows was modeled with heat conduction by temperature boundary conditions. In the experiment, the temperature at the outer side of the bottom window $T_{air,below}$ was measured, which was interpolated in time and set as boundary temperature in the simulation. At the side glass window, the two temperatures $T_{air,lower\ side}$ and $T_{air,upper\ side}$ were measured at the bottom and top of the outer side of the window. These temperatures were first interpolated in time and then over the height y onto the boundary mesh of the simulation. These transient boundary conditions were calculated in MATLAB, which was coupled to ANSYS Fluent, as already described by Vogel et al. [21]. The described 3D model was a detailed

reproduction of the experiment and was mainly used to validate the model with the experiment.

3.2.6 Discretization

The governing equations were discretized with a pressure-based finite volume method [65] and implicit time integration in ANSYS Fluent 16 [62]. The segregated solver was used with the PISO method for pressure-velocity-coupling [65]. The second order derivatives in the diffusive terms were approximated by second order central differences, the first order derivatives in the convective terms with a second order upwind scheme [62]. The interpolation of pressure values at the cell faces was done with the PRESTO! scheme [65]. For the VOF method in the detailed model (V-2D), the explicit scheme was used with a Courant number of 0.25. The implicit body force formulation and the sharp interface modeling were selected. The volume fraction was calculated with the geometric reconstruction scheme [62]. The resulting linear systems were solved with an iterative method with algebraic multigrid acceleration [65].

The rectangular geometries were discretized with ANSYS meshing [62] on a structured quad mesh in 2D or a structured hex mesh in 3D. A cell size of 0.25 mm was found to be optimal in a mesh dependency study. Therefore, this size was used throughout the 2D meshes, which resulted in meshes with about 40 000 control volumes. However, for the 3D case, the cell sizes were increased to decrease the computational effort. In the x -direction, the cell size remained 0.25 mm to resolve the boundary layers. In the y - and z -direction the cell size was increased to a range of 0.25 . . . 1 mm and a cell size distribution with a finer mesh towards the boundaries was introduced. The 3D mesh was then built of about 140 000 control volumes.

For the simplified model without volume expansion (B-2D), a time step of $\Delta t = 0.1$ s was a good tradeoff between fast convergence and low computation time. The maximum Courant Number was slightly above one. The implicit scheme theoretically allowed larger Courant numbers, but the convergence was found to become inefficiently slow. A smaller time step was needed for convergence of the detailed model with VOF method (V-2D). The best results were found with the variable time stepping method [62] and a time step corresponding to a Courant Number of 0.25, which was the same as specified for the explicit scheme in the

VOF model. With this method the time step was of the order of $1 \cdot 10^{-4}$ s at the beginning and increased up to $1 \cdot 10^{-2}$ s at later times.

Iterations continued until a convergence criterion was met. Solution convergence was found to be restricted by the mass continuity, for which the scaled absolute residual threshold was set to a value of $1 \cdot 10^{-3}$. Between 30 and 150 iterations were needed to reach this criterion. The residuals of the momentum equations and the energy equation fell below $1 \cdot 10^{-8}$ and $1 \cdot 10^{-15}$, respectively.

3.3 Results and discussion

Firstly the two 2D models were compared with each other to find out if the simplified model is accurate enough and the Boussinesq approximation is a valid simplification. Secondly, the 3D model with adjusted boundary conditions (B-3D) was compared to the experiment for model validation.

The simulation data are stored on one of two hard drives associated to this thesis. The raw data are stored in the folder `\DATA_A\ANSYS\Versuch\FLUENT\` and the evaluated data are stored in `\DATA_A\Evaluation\simulation\`.

3.3.1 Comparison of the 2D models V-2D and B-2D

The melting process was qualitatively analyzed by evaluating the 2D fields of phase state and velocity. Then, a quantitative evaluation was done: the liquid phase fraction and heat flow rate, the velocity extrema occurring in the liquid phase and temperatures at three positions were evaluated over time.

2D fields of phase state and velocity

The fields of phase state and velocity by natural convection in the liquid phase are illustrated in Figure 3.4 at time $t = 3600$ s and in Figure 3.5 at time $t = 7200$ s. The solid phase of the PCM is drawn in black such as the solid side and bottom walls. In the liquid phase, filled contours show the velocity magnitude and vectors show the velocity direction as well as the magnitude. The interface between the PCM and the air phase in the detailed model (V-2D) is represented by a white line, while, in the simplified model (B-2D), the top side is a fixed slip wall.

The velocity magnitudes and the boundary layers are qualitatively similar in both models. However, the resulting solid phase shape appears to be smaller and wider in the V-2D model compared to the taller and narrower solid phase in

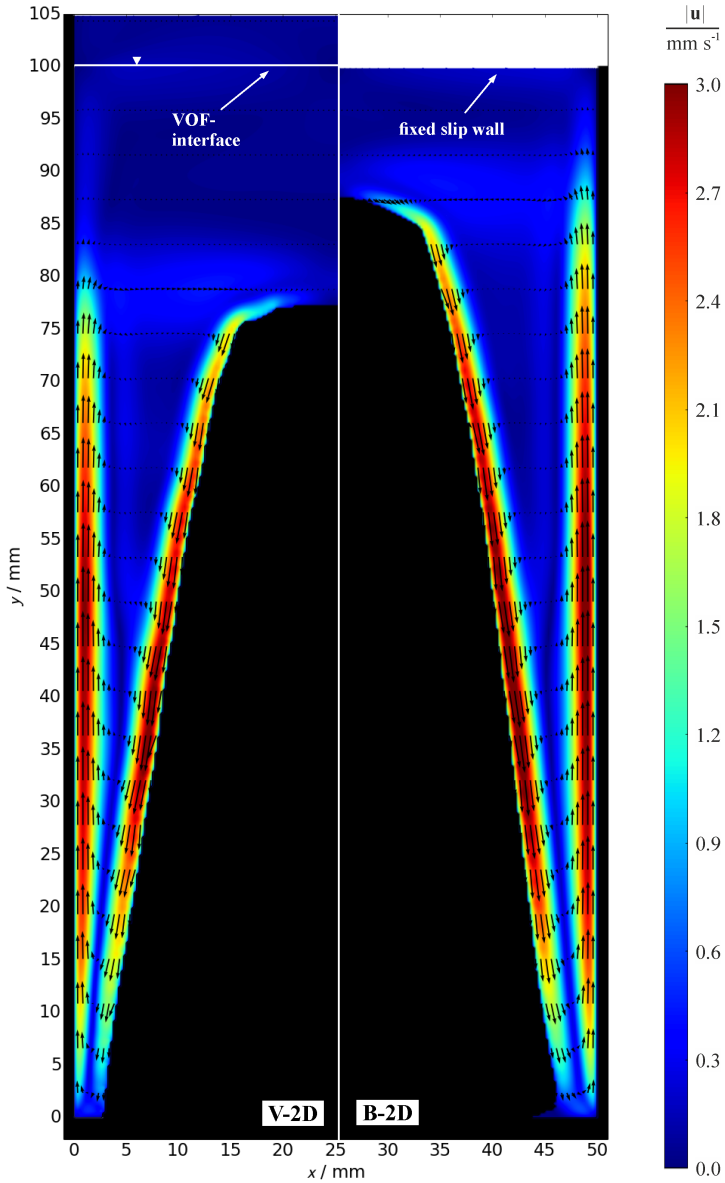


Figure 3.4: Comparison of 2D fields of phase state and velocity for the detailed (V-2D) and the simplified model (B-2D) at time $t = 3600$ s.

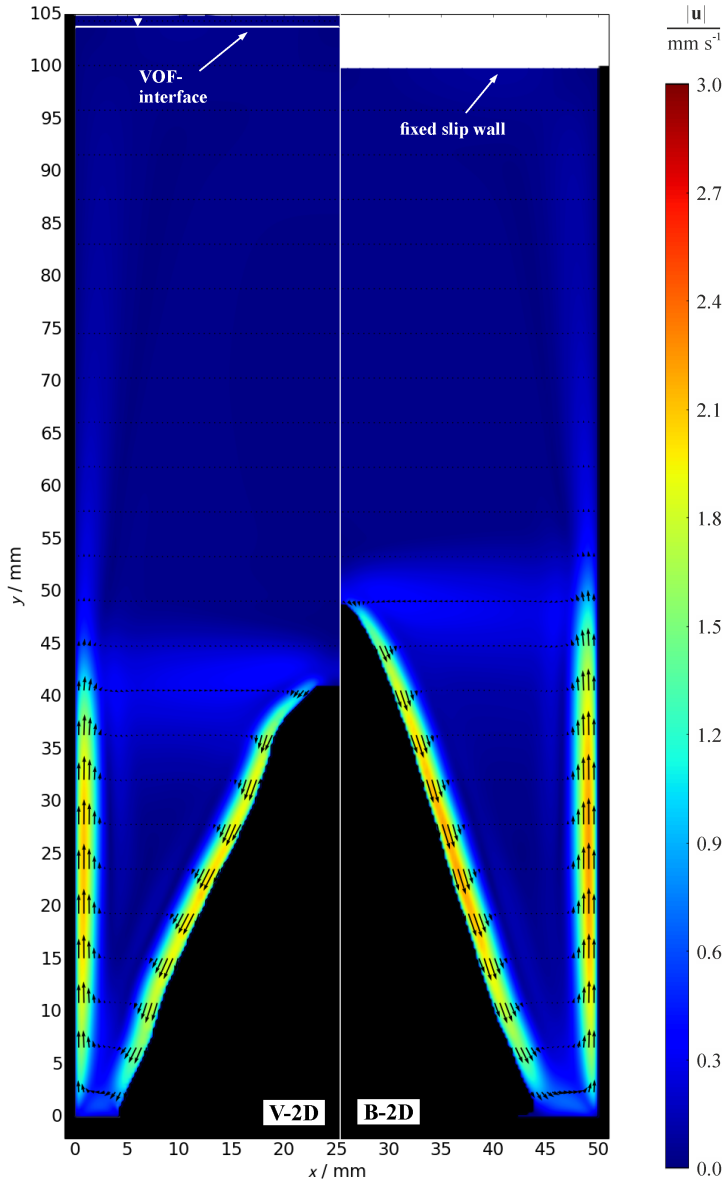


Figure 3.5: Comparison of 2D fields of phase state and velocity for the detailed (V-2D) and the simplified model (B-2D) at time $t = 7200$ s.

the B-2D model. This indicates a faster melting at the top and slower melting at the bottom in the V-2D model relative to the B-2D model. This difference may be either due to the different choice in material properties or due to the different boundary condition at the top, namely the VOF-interface or the fixed slip wall. A pre-study already showed that the influence of variable heat capacity, thermal conductivity and viscosity is rather small. The volume expansion and the moving interface in the VOF model may be the main reason for the observed differences. An obvious reason is that the solid phase had an initial height of only $H_s = 95$ mm in the V-2D model instead of $H = 100$ mm in the B-2D model, which made a difference from the beginning. The volume expansion up to a final height of $H_1 = 105$ mm in the V-2D model could have also increased convection at the top and inhibited convection at the bottom, due to an additional upwards flow which increased the upward flow at the heated walls and decreased the downward flow at the solid phase. The result is probably a stronger convection at the top than at the bottom, which leads to the difference in the phase front shapes.

Liquid phase fraction and heat flow rate

A quantitative analysis of the liquid phase fraction and the heat flow rate helps to analyze the overall melting process. Figure 3.6 shows both quantities plotted over time for the VOF model (V-2D) and the Boussinesq model (B-2D).

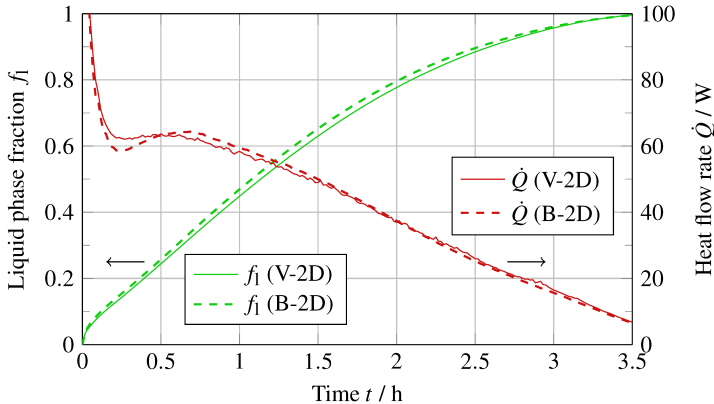


Figure 3.6: Comparison of the liquid phase fraction of the PCM and the heat flow rate into the PCM plotted over time for the V-2D and the B-2D models.

The resulting curves of both models are qualitatively similar and there are only small deviations. The quantitative difference in liquid phase fraction has a mean value of 1.4% and a maximum value of 2.2%. The heat flow rates deviate by 3.1% in the mean with a maximum difference of 10.1% that occurs only over a small period of time. Although the shape of the solid phase was observed to be slightly different in the last section, the integral liquid phase fraction is nearly identical in both models. Conclusively, despite the differences in the models and observed qualitative differences, the overall melting process is similar.

Velocity extrema

The velocities are also analyzed over time. However, it is not straight forward to find a scalar velocity value that is representative for the melting process. Taking the velocity at a certain fixed point or even multiple points, the choice of position of this point would be critical for the results. Either the same velocity would be obtained for a long period of time or the velocity could be zero the majority of the time. The mean value of the velocity magnitude is also not meaningful, because the velocities outside of the narrow boundary layers are close to zero, which would lead to a small mean value. The solution was to calculate the velocity extrema separately for the x - and y -direction and for many evaluation time steps. The result is shown in Figure 3.7.

The velocities v in y -direction are very similar to each other, while the velocities u in x -direction show a qualitative difference at least at the beginning of the melting process. The mean deviation of velocities u in x -direction are 20% and the mean deviation of velocities v in y -direction are 8.2%. At the beginning of melting in the VOF model, the velocities $\max(u)$ in positive x -direction decrease earlier and the velocities $\min(u)$ in negative x -direction remain higher. The differences in u are probably due to the different boundary condition at the top. Overall, the differences in the velocity extrema are not substantial and probably negligible.

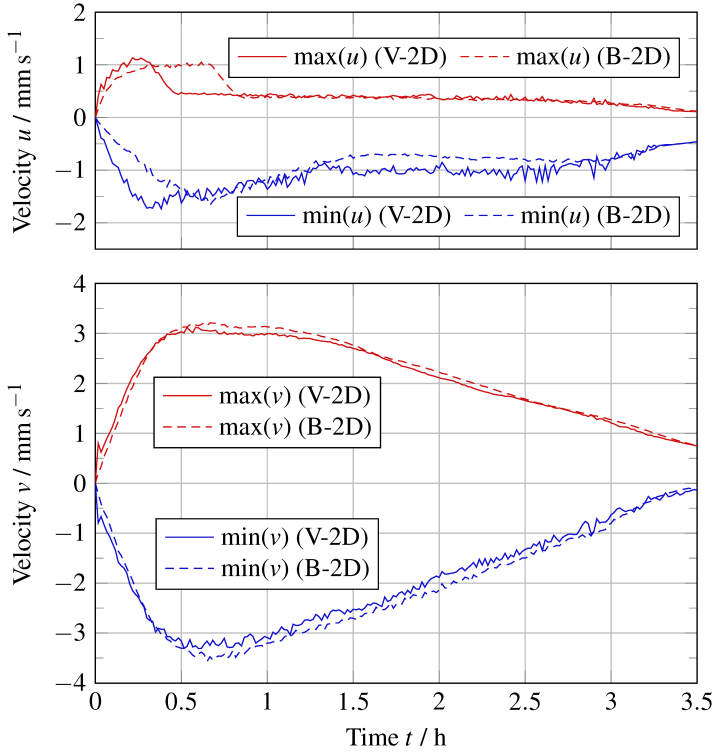


Figure 3.7: Comparison of velocity extrema in x- and y-direction plotted over time for the V-2D and B-2D models.

Temperatures

The temperatures were evaluated at the three distinct positions $T_{PCM,1}$, $T_{PCM,2}$ and $T_{PCM,3}$ shown in Figure 2.2 and given in Table 2.4. The simulated results for the detailed V-2D and the simplified B-2D model are plotted over time in Figure 3.8.

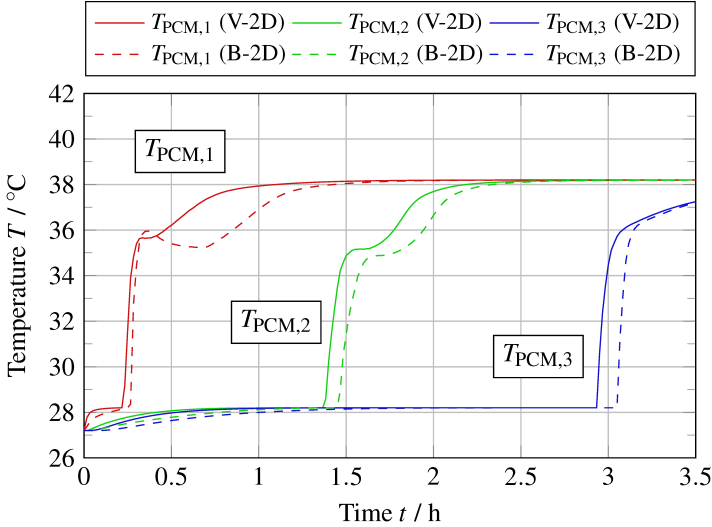


Figure 3.8: Comparison of temperatures at three positions over time for the V-2D and the B-2D models.

The curves for temperature $T_{PCM,1}$ have a qualitative difference at the time right after the melting front passed the temperature probe position after $t = 0.5$ h. However, the curves for temperatures $T_{PCM,2}$ and $T_{PCM,3}$ are similar and only shifted in time. The mean difference over the melting process is 1.1% for $T_{PCM,1}$, 1.2% for $T_{PCM,2}$ and 1.0% for $T_{PCM,3}$. The differences in temperature are also mostly negligible.

3.3.2 Comparison of the 3D Boussinesq model (B-3D) with the experiment

The comparison of the two different models in 2D showed only minor differences. In conclusion, the Boussinesq approximation, the neglected volume ex-

pansion and the assumption of constant material properties are valid for this test case. Hence, the simpler Boussinesq model was preferred to simulate the 3D case. The 3D case additionally included viscous boundary layer effects at the front and back enclosure walls. Also, the thermal boundaries were adjusted at all sides to data from the experiment to include the small but remaining heat flows over the boundaries. This way, the simulation model could be precisely compared to the experiment. As in the section before, the primary quantities of interest are the phase state, the velocity and the temperature. In a first step, the 2D fields of phase state and velocities in the liquid phase in the mid-plane ($z = 25$ mm) of the enclosure are evaluated in the simulation and compared to results from the experiment given in section 2.4.1. In a second step, the quantitative values over time of liquid phase fraction, velocity extrema and temperatures in the PCM are evaluated from simulated data and compared with results from the experiment provided in section 2.4.4.

2D fields of phase state and velocity in the mid-plane

As in the last section, the fields of phase state and velocities by natural convection in the liquid phase were evaluated, but this time data from the B-3D model were compared to the validation experiment. The results are illustrated in Figure 3.9 for the time $t = 3600$ s. The solid phase of the PCM is drawn in black as are the solid walls. In the liquid phase, filled contours show the velocity magnitude and vectors show the velocity direction as well as the magnitude. In the simulation model B-3D shown on the left side, the velocity is evaluated in a plane in the middle of the enclosure ($z = 25$ mm). The data looks slightly disturbed at the phase front, which is mostly due to a coarser grid in the 3D case compared to the 2D case and the interpolation from control volume centered values onto the faces of the mid-plane. The experimental data was obtained with the shadowgraph technique to obtain the phase state, see section 2.3.1, and the Particle Image Velocimetry technique to measure velocities in a plane in the middle of the enclosure ($z = 25$ mm), see section 2.3.2.

The solid phase has a smaller and narrower appearance in the simulation compared to the experiment. While the velocity magnitudes are similar at the phase boundary of the PCM, the simulated velocities exceed the measured velocities at the heated wall. Since the flow is laminar, see subsection 2.2.4, turbulence should not be the reason for deviations. A detailed 3D model with VOF method including volume expansion and variable material properties would probably lead to

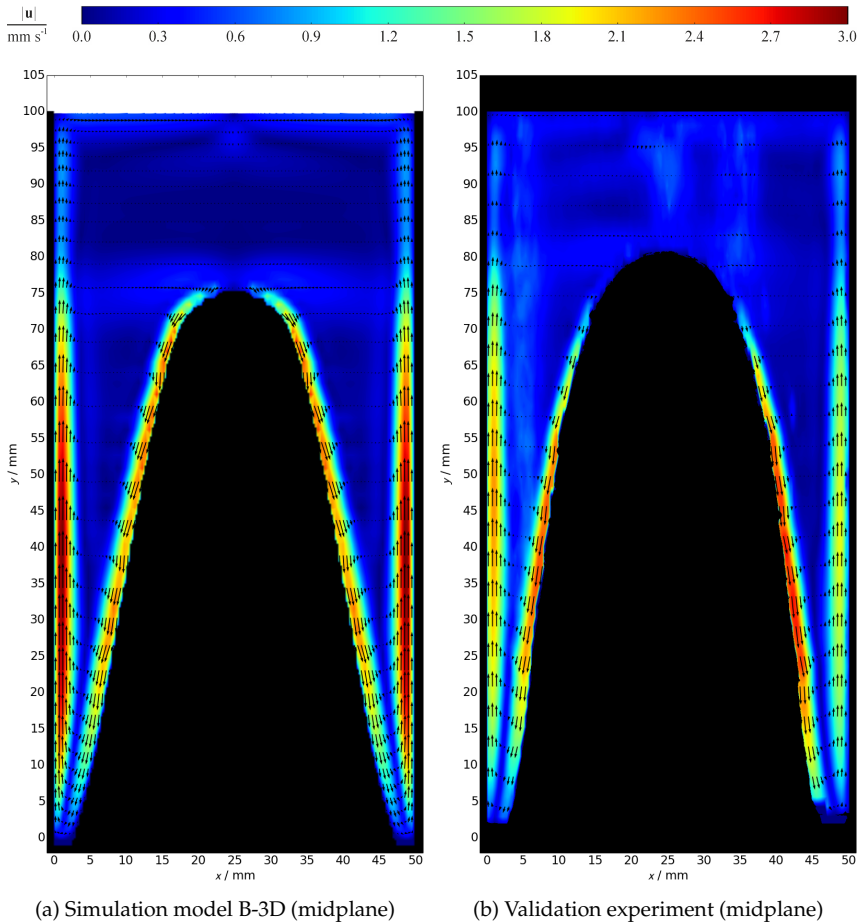


Figure 3.9: Comparison of simulation results with the B-3D model with results from the validation experiment at time $t = 3600$ s.

a better qualitative agreement than the simplified Boussinesq model (B-3D) used here, but the computational effort would be significantly higher. And there are certain other features in the experiment, which would still not be modeled in the simulation, e.g. gas bubbles rising from the solid phase. Conclusively, regarding the simplifications in this model, which was used due to its favorable computational effort, the simulation qualitatively agrees with the experiment. The quantitative evaluation follows in the next sections.

Liquid phase fraction

The liquid phase fraction was evaluated in the simulation with the B-3D model and compared to the experimentally measured data from section 2.4.4. The results are shown in Figure 3.10. The error bars include systematic and statistic measurement uncertainties calculated in section 2.4.2.

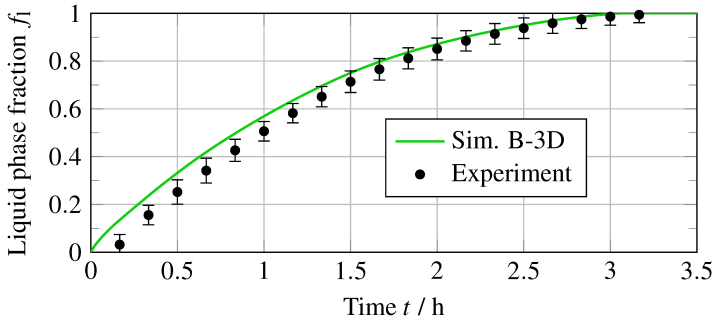


Figure 3.10: Comparison of the liquid phase fraction over time for the simulation B-3D and for the measured data from the validation experiment.

A maximum deviation of the simulation from the experiment of 10 % is found at the beginning of the melting process. The mean deviation is 4 %. Conclusively, the melting process is found to be similar in the simulation and the experiment.

Velocity extrema

The velocities from the simulations with the B-3D model were also compared to experimental data from section 2.4.4. The velocity extrema were again calculated in both axis directions in the mid-plane of the enclosure. The results are shown

in Figure 3.11. The error bars include systematic and statistic measurement uncertainties from section 2.4.2.

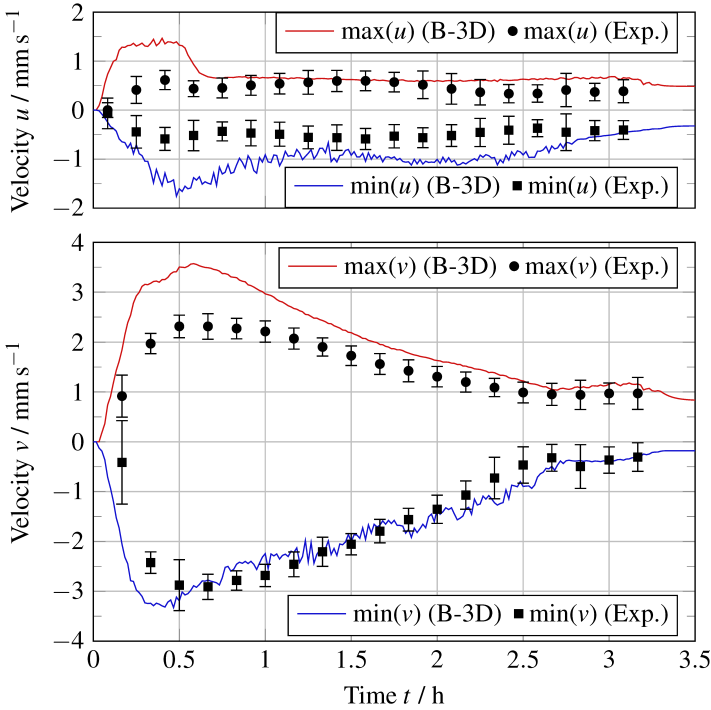


Figure 3.11: Comparison of u - and v - velocity extrema over time from the simulation model B-3D and from PIV-measurements in the experiment.

The maximum velocity magnitudes are mostly higher in the simulation compared to the experiment. The simulated velocities u are slightly higher in both negative (left) and positive (right) x -direction. The simulated velocities v are significantly higher in the positive (upward) y -direction but similar in the negative (downward) y -direction. The mean deviation is about 60 % for u and 20 % for v .

Temperatures

Finally, temperatures evaluated in the 3D simulation were compared to temperatures measured with thermocouples in the experiment, which is described in

section 2.4.4. The results are shown in Figure 3.12. The temperature probe positions are shown in Figure 2.2 and their coordinates are given in Table 2.4. The error bars include systematic and statistic measurement uncertainties calculated in section 2.4.2.

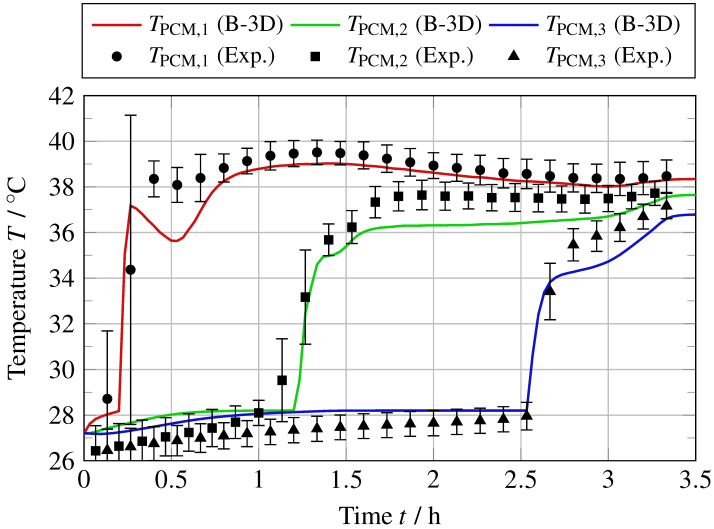


Figure 3.12: Comparison of temperatures at three positions over time from the evaluation probes in the simulation model B-3D and from the thermocouple measurements in the experiment.

The error bars are quite large at steep gradients, because these cannot be exactly reproduced in repeated measurements and the statistic errors were calculated separately for every time step. The simulated temperature curves are similar to the experimentally measured data. However, the temperatures in the experiment are slightly lower initially and then slightly higher at the end of melting in the vicinity of the probe. The instants of melting are captured well. The mean deviations over the melting process are 1.8 % for $T_{PCM,1}$ and 2.8 % for both $T_{PCM,2}$ and $T_{PCM,3}$.

3.4 Conclusions

The comparison of the detailed modeling approach with variable material properties and the VOF-method (V-2D) to the simplified approach with constant material properties and the Boussinesq approximation (B-2D) revealed differences only upon closer inspection. Deviations are seen mostly in the velocities and temperatures. However, the liquid phase fraction and heat flow rate, which indicate the overall charging state and power of a storage system, are very similar. And these are the more important properties in the design of a storage system. In conclusion, while the simplified B-2D is not able to reproduce the melting process in every detail, it is sufficiently accurate to be used in the design process of latent heat storage systems. This may be however different for higher driving temperature differences or increased subcooling, where the variable material properties have a greater impact.

The comparison of the simplified model in three dimensions with boundary effects (B-3D) to the validation experiment showed that the simulated phase state and velocities are qualitatively similar to the validation experiment. Only the simulated mean velocity extrema are 60 % higher for the velocity u in x -direction and 20 % higher for the velocity v in y -direction compared to the experiment and it is not yet understood what exactly is the reason for this. However, the liquid phase fraction only deviates by a mean value of 4 % and temperatures by a mean value of 2.8 % in the worst case. These results indicate that the simplified model (B-3D) is accurate enough to reproduce the experimentally measured melting process and that it is qualified for further studies to analyze the impact of natural convection in LHS systems.

Chapter 4

Heat transfer enhancement due to natural convection

In chapter 3, numerical models for melting governed by natural convection were compared and validated with the experiment described in chapter 2. An important result was that the simplified model with constant material properties and Boussinesq approximation is accurate enough to study the overall state of charge and charging power of a LHS system. In this chapter, the simplified numerical model is used for an investigation on the heat transfer enhancement due to natural convection in enclosures with different dimensions of a LHS system. Additionally, the influence of the driving temperature difference is analyzed using data from the validation experiment. The main result is a correlation for the liquid phase fraction evolution over scaled time in dimensionless form.

4.1 State of research and objectives

In the following, the state of research specifically on dimensional analyses on melting in rectangular enclosures is given. Bareiss and Beer [31] experimentally studied a rectangular enclosure with different heights heated on one side and cooled on the other side. Nusselt correlations as well as analytic solutions for the melting process were found. Okada [66] studied the heat transfer during melting and gave a correlation for the Nusselt number over dimensionless time. Gadgil and Gobin [67] numerically studied melting in enclosures with different aspect ratios. Bénard, Gobin and Martinez [24] experimentally and numerically studied the melting process and also provided an analytic solution of the liquid

phase fraction evolution over time. Gau and Viskanta [25] not only performed one of the most popular melting experiments, but also presented correlations of the liquid phase fraction and the Nusselt number in dimensionless form. Wolff and Viskanta [27] studied melting in a rectangular enclosure and gave a correlation for the liquid phase fraction over time in dimensionless form. Jany and Bejan [19] enhanced the scaling theory of natural convection melting in a rectangular enclosure and gave correlations for the Nusselt number and melting front. Another thorough investigation concerning an electric storage heater with a PCM contained in rectangular enclosures between flat plates was done by Farid and Husian [57]. With an experimental storage unit, they derived a correlation for an enhanced thermal conductivity to be used in one-dimensional numerical models. An experimental investigation of melting was performed by Wang, Amiri and Vafai [68], who presented correlations for the liquid phase fraction and the Nusselt number. Shatikian, Ziskind and Letan [54, 69] conducted investigations of a PCM-based heat sink with internal fins and different enclosure dimensions, in which they scaled the results with the relevant dimensionless groups. The Nusselt number was calculated locally over the height of the enclosure by evaluating horizontal slices by Shokouhmand and Kamkari [32]. A parameter study on melting in a rectangular enclosure with a free-moving ceiling was performed by Ho et al. [70], where also Nusselt numbers were calculated.

The main findings are summarized as follows: Melting is mostly by heat conduction at the beginning, but natural convection predominates at later times with higher melting rates at the top than at the bottom, which leads to a curved phase front shape [23]. The transition point between conduction and convection [31] and the variation of heat transfer over the height [23] can be determined in dimensionless form. Dimensional analysis of the melting process [24] reveals the four dimensionless groups Rayleigh number Ra , Prandtl number Pr , Stefan number Ste and aspect ratio A . The melting rate depends on the Rayleigh number, the aspect ratio and the dimensionless time, which is the product of Fourier number Fo and Stefan number Ste . It is found that the melting rate decreases with the aspect ratio [25]. Natural convection is quasi-steady and not strongly influenced by the movement of the interface, because the flow velocities are much larger than the velocity of the interface movement [26]. The Nusselt number has a local maximum around the top of the solid PCM [32].

The mentioned research provides many insights into the melting process with natural convection. However, the results are not directly applicable to flat plate

LHS systems, due to several reasons: 1) the systems have a heated wall on one side and a cooled or insulated wall on the other side, but melting in LHS systems usually occurs symmetrically between two heated walls, 2) the aspect ratio range does not cover the typically tall enclosures of flat plate LHS systems and, 3) the parameter variation is not sufficient to derive general correlations. In summary, there is no comprehensive data for flat plate LHS systems. It is therefore difficult to predict how natural convection will influence the heat transfer rate in a LHS system.

To contribute to the stated research demand, two different analyses are presented in the following sections. Firstly, the numerical model from chapter 3 is used for a parameter study of a wide range of dimensions of rectangular enclosures to derive a scaling procedure for the problem. And secondly, data from the validation experiment, see chapter 2, is evaluated to show that the scaling procedure is valid and to extend the study on different driving temperature differences. From these two analyses, a correlation for the liquid phase fraction over time is derived in dimensionless form.

4.2 Numerical parameter study on enclosure dimensions

For this numerical parameter study, the numerical model with constant material properties and Boussinesq approximation described in section 3.2 was used. A parameter study was conducted to find the influence of enclosure dimensions on heat transfer during melting governed by natural convection that occurred while charging the storage. Discharging was not investigated, because of the minor impact of natural convection in solidification.

The simulation data are stored on one of two different hard drives that are associated to this thesis. The raw data are stored in the folder `\DATA_A\ANSYS\Parameterstudie\FLUENT\`. The evaluated data are stored in the folder `\DATA_A\Evaluation\study\`.

In the next sections, material properties, the geometry and the parameter variation are given and the phase front shapes of different cases are compared. Then a scaling of the melting process by dimensional analysis is presented, which, finally, enables an investigation of the impact of natural convection on heat transfer.

4.2.1 Material properties

The basis of this study was the high temperature flat plate latent heat storage system described by Vogel et al. [21], where the eutectic mixture of sodium nitrate and potassium nitrate ($\text{KNO}_3\text{-NaNO}_3$) was used. This material has been characterized by Bauer et al. [71]. The eutectic mixture was obtained with 54 wt.% KNO_3 and 46 wt.% NaNO_3 . The melting temperature measured for the used technical grade quality was $T_m = 219.5^\circ\text{C}$ and the latent heat was $L = 108\text{ kJ/kg}$. The containment material was carbon steel 1.0425. The material properties used in the simulations are given in Table 4.1. Constant properties were used at a temperature about the melting point in the liquid state.

Table 4.1: Thermophysical material properties of the nitrate salt $\text{KNO}_3\text{-NaNO}_3$ used as PCM and the steel 1.0425 used for the containment.

Property	Unit	$\text{KNO}_3\text{-NaNO}_3$	Steel 1.0425
ρ_l	kg/m^3	1959	7800
$c_{p,l}$	$\text{J}/(\text{kg K})$	1492	540
k_l	$\text{W}/(\text{m K})$	0.46	51
μ_l	Pa s	$5.8 \cdot 10^{-3}$	-
β_l	$1/\text{K}$	$3.5 \cdot 10^{-4}$	-
T_m	$^\circ\text{C}$	219.5	-
L	kJ/kg	108	-

4.2.2 Geometry and parameter variation

To investigate the impact of enclosure dimensions on the melting process, a parameter study with different widths and heights was conducted. For this purpose, a simple storage model was defined, as shown in Figure 4.1.

The domain and boundary conditions were the same as for the model of the experimental storage unit, described in section 3.2.4. However, the influence of a heat conducting bottom plate was neglected and, instead, an adiabatic, no-slip wall boundary condition was set. The boundary temperature was set to a constant value $T_w = 232^\circ\text{C}$, which was $\Delta T = 12.5\text{ K}$ above the melting temperature of the PCM. The initial temperature of the whole domain was $T_0 = 217^\circ\text{C}$. The

4.2 Numerical parameter study on enclosure dimensions

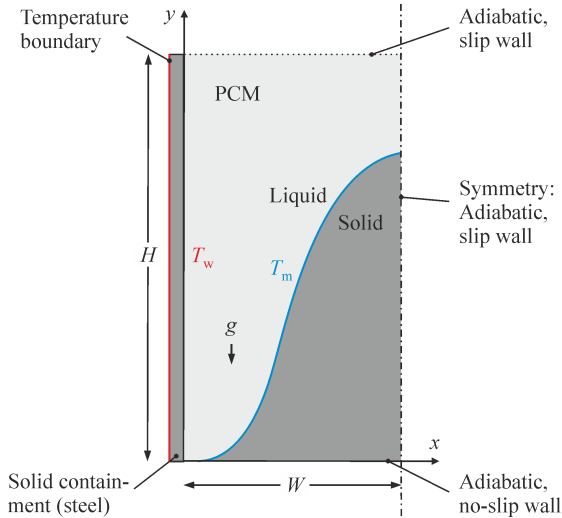


Figure 4.1: Simulation domain for the parameter study investigating different widths and heights.

geometry was defined parametrically to easily vary the height and width of the enclosure.

The dimensions of the rectangular enclosures and the resulting aspect ratios and Rayleigh numbers are given in Table 4.2. The Stefan and Prandtl numbers are constant for all cases with values of $Ste = 0.17$ and $Pr = 18.6$. For a definition of the dimensionless groups, see section 2.2.1.

It is noteworthy that these numbers were calculated with the enclosure height H and width W , but natural convection depends only on the liquid part of the PCM inside the enclosure, which continually increases during melting. Hence, a transient Rayleigh number and a transient aspect ratio for only the liquid part could be defined. However, it was found to be sufficient to use the enclosure dimensions, which describe the maximum effect of natural convection.

To find out if the flow is laminar or turbulent, Equation 2.3 for the onset of turbulence depending on the Rayleigh number Ra_H can be used. Most cases are in the laminar range. However, the test cases W25H500 and W25H1000 have a Rayleigh number slightly above the transition criterion for turbulence, so in these test cases turbulent flow might have been occurred.

Table 4.2: Names, dimensions and dimensionless numbers of all investigated test cases of the parameter study.

Case name	W/mm	H/mm	$A = H/W$	Ra_H	Ra_H/A^4
W25H12.5	25	12.5	0.5	$1.9 \cdot 10^5$	$3.0 \cdot 10^6$
W25H25	25	25	1	$1.5 \cdot 10^6$	$1.5 \cdot 10^6$
W25H50	25	50	2	$1.2 \cdot 10^7$	$7.5 \cdot 10^5$
W25H100	25	100	4	$9.6 \cdot 10^7$	$3.8 \cdot 10^5$
W25H200	25	200	8	$7.7 \cdot 10^8$	$1.9 \cdot 10^5$
W25H500	25	500	20	$1.2 \cdot 10^{10}$	$7.5 \cdot 10^4$
W25H1000	25	1000	40	$9.6 \cdot 10^{10}$	$3.8 \cdot 10^4$
W10H200	10	200	20	$7.7 \cdot 10^8$	$4.8 \cdot 10^3$
W05H200	5	200	40	$7.7 \cdot 10^8$	300

The onset of natural convection depends on the fraction Ra_H/A^4 , see Equation 2.2. From the values given in Table 4.2, only W05H200 is probably heat conduction dominated and all other test cases are expected to be dominated by natural convection.

4.2.3 Comparison of the phase front shape

The phase front is visualized for several different test cases for comparison in Figure 4.2. For every test case, nine contours show the developing phase front at a time step that corresponds to liquid phase fractions $f_l = 0.1$ to 0.9 in steps of 0.1 . The relationship of the liquid phase fraction and the instant of time is different for each case, so the figures do not give an impression on the temporal evolution, but rather on the different shapes of the phase front at similar liquid phase fractions.

To investigate the influence of the enclosure width, three different widths of $W = 5$ mm, 10 mm and 25 mm with a fixed height of $H = 200$ mm are compared to each other in Figure 4.2 (a), (b) and (c). In the case W05H200 with the smallest width $W = 5$ mm, melting occurs mostly in a horizontal direction; the phase front is nearly vertical for the most part. Melting is dominated by heat conduction. However, for the test cases with greater widths and smaller aspect ratios, W10H200 and W25H200, the phase front is increasingly inclined at higher liquid

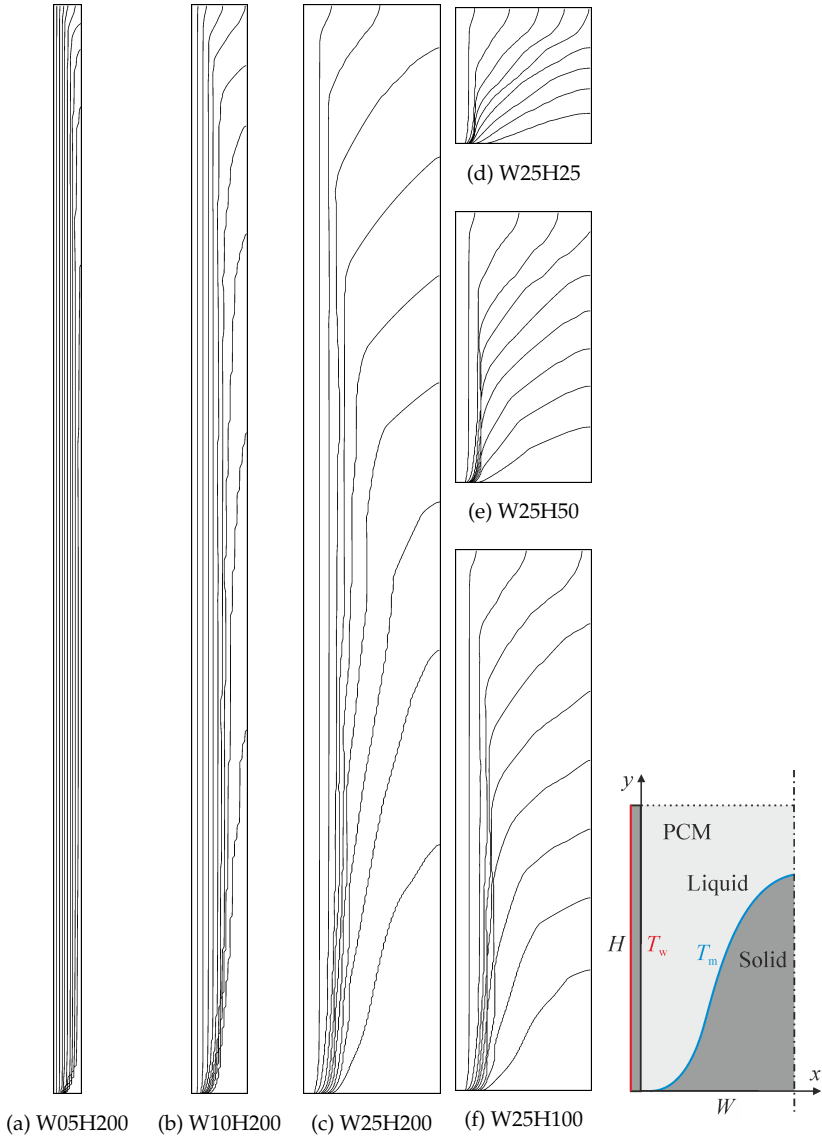


Figure 4.2: Nine phase front contours correspond to liquid phase fractions of $f_l = 0.1, 0.2, \dots, 0.9$ for six different test cases.

phase fractions due to natural convection. The heat transfer with natural convection leads to an advective transport of heated fluid to the top, which leads to a temperature gradient from bottom to top. Hence, melting is enhanced at the top and diminished at the bottom. Natural convection strength not only increases with higher Rayleigh number Ra_H but also increases with lower aspect ratio A of the test case.

To assess the influence of the enclosure height, four different heights $H = 200$ mm, 100 mm, 50 mm and 25 mm with a fixed width of $W = 25$ mm are compared with each other in Figure 4.2 (c), (d), (e) and (f). A strong influence of natural convection is obvious in all cases, with the phase front becoming strongly inclined with increasing liquid phase fractions. It is observed that in the case with a small height W25H25 and an aspect ratio of $A = 1$, melting occurs at a similar rate in the horizontal as well as the vertical direction. However, for the cases with larger height, W25H50, W25H100, and W25H200, melting increasingly occurs vertically from top to bottom. As soon as the phase front reaches the middle plane, which is the right side of the figures, melting occurs mostly from top to bottom up to high liquid phase fractions of more than $f_l = 0.9$. In these cases the Rayleigh number Ra_H increases with the height, but the aspect ratio A increases as well. As natural convection depends on the factor Ra_H/A^4 , natural convection strength is the highest with smallest aspect ratio, which corresponds to the smallest height in this comparison.

4.2.4 Liquid phase fractions over time

The evaluation of liquid phase fractions over time for all parameter variations is shown in Figure 4.3. The melting process is slower with greater widths and with greater heights. Increasing the width increases the resistance to heat transfer by diffusion. Natural convection becomes relevant after a critical width of the liquid phase and becomes stronger with greater widths due to smaller aspect ratios, see Equation 2.2. But the heat transfer enhancement by natural convection does not compensate the higher heat resistance of a larger distance between the heated wall and the phase front, which leads to slower melting with greater widths. Varying the height and thereby increasing the aspect ratio leads to similar findings. While flow velocities due to natural convection increase with the height, the heat transfer decreases due to a longer heat transfer path. This theory is supported by Schinkel et al. [72] who found that most of the heat is transferred

at the lower part of the heated wall during heat transfer by natural convection in an air cavity. Moreover, it is obvious from the melting shapes that heat is transferred mostly at the upper part of the phase front. Hence, for larger heights (or aspect ratios), the distance from the heat source (lower heated wall) to the heat sink (upper phase front) increases.

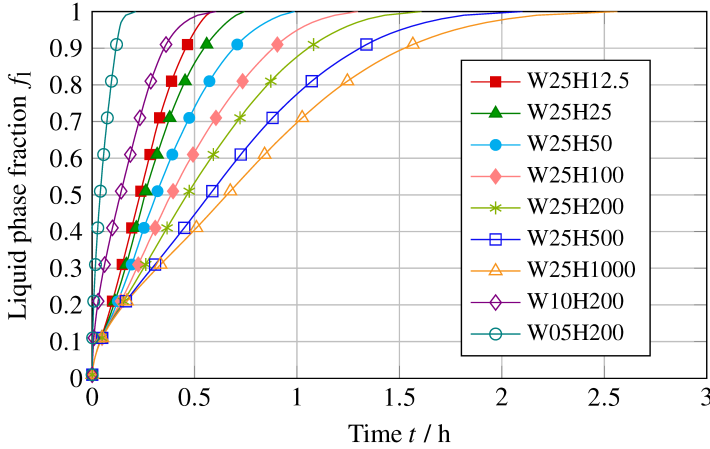


Figure 4.3: Liquid phase fraction plotted over time for all test cases.

4.2.5 Scaling of the melting process

The liquid phase fractions over time were scaled with the relevant dimensionless groups $Fo_H(t)$, Ra_H , and A in a similar approach as by Shatikian, Ziskind and Lethan [54, 69]. However, the Stefan number Ste was disregarded, because it is constant in this investigation due to a constant driving temperature difference ΔT . Instead, the aspect ratio A was included. A good scaling was obtained by trial and error with exponents of 1 for Fo , $1/6$ for Ra_H and $5/4$ for A . The result is shown in Figure 4.4.

After scaling, the curves mostly coincide. An outlier is the case W05H200, which is the only one dominated by heat conduction. Therefore, the scaling overestimates the impact of natural convection in this case.

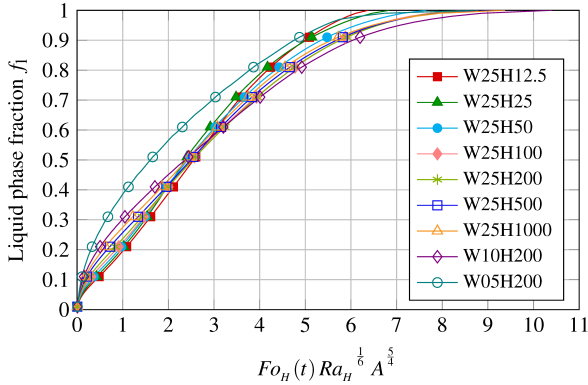


Figure 4.4: Scaled liquid phase fraction plotted over the relevant dimensionless groups for all test cases.

4.2.6 The impact of natural convection on heat transfer

To analyze the impact of natural convection, a convective enhancement factor was defined as the ratio of the actual heat flux to a hypothetical heat flux by heat conduction only:

$$\varepsilon(f_1) = \frac{\dot{Q}(f_1)}{\dot{Q}_{\text{cond}}(f_1)}. \quad (4.1)$$

To calculate this parameter, the heat transfer rates of two different simulations, one with natural convection (\dot{Q}) and one with only heat conduction (\dot{Q}_{cond}), were evaluated. In the simulation of heat conduction only Equation 3.13 for energy conservation was solved without the flow Equations 3.9 and 3.10. Since the time scale and the phase front shapes are different in each simulation, they were both evaluated at times with equal liquid phase fractions f_1 . The resulting convective enhancement factors are plotted over the liquid phase fraction in Figure 4.5 for all parameter variations.

For the case with the smallest width $W = 5$ mm and intermediate height $H = 200$ mm, a small value of the convective enhancement factor $\varepsilon \approx 1$ is found, which underlines the expectation in this case that heat transfer is mostly by heat conduction. With increasing width, but constant height, the heat transfer enhancement by convection increases significantly up to a maximum value of $\varepsilon = 4$ for a width of $W = 25$ mm. With increasing height at constant width, the heat transfer enhancement decreases slightly to $\varepsilon = 3$ for a height of $H = 1000$ mm. With de-

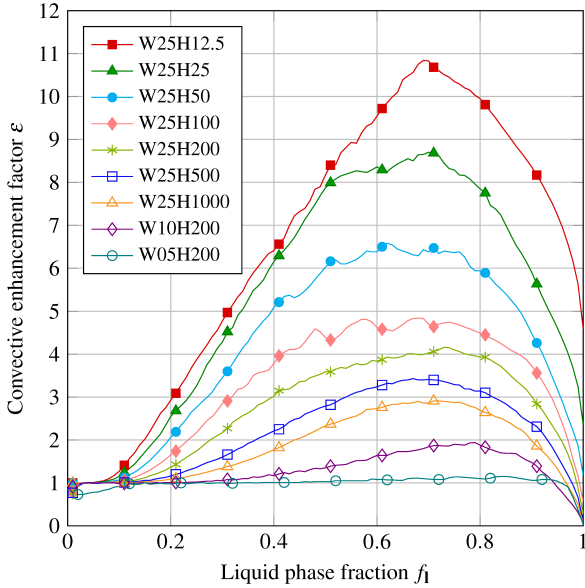


Figure 4.5: Convective enhancement factor plotted over liquid phase fraction for all test cases.

ing height, it increases up to a maximum value of $\varepsilon = 11$ for the smallest height of $H = 12.5$ mm. However, this trend is expected to reverse at even smaller heights. When the height is decreased to a size of the order of the boundary layer thickness at the wall, fluid flow will stagnate and the convective enhancement factor will eventually decrease back to $\varepsilon = 1$.

To quantify the convective enhancement factor, its mean value $\bar{\varepsilon}$ is calculated for each case and plotted over the relevant dimensionless groups Ra_H and A in Figure 4.6. The mean convective enhancement factor $\bar{\varepsilon}$ is an estimation of the impact of natural convection on the whole charging process. For example, in the case W25H200, heat transfer by natural convection is about three times higher as it would be by only heat conduction.

Since the data points suggest a linear relationship, a linear fit function was computed. It is bounded by the minimum value of the convective enhancement factor, $\bar{\varepsilon} = 1$, where the heat flow rate by natural convection equals that of heat conduction. Hence, the influence of natural convection vanishes at this point.

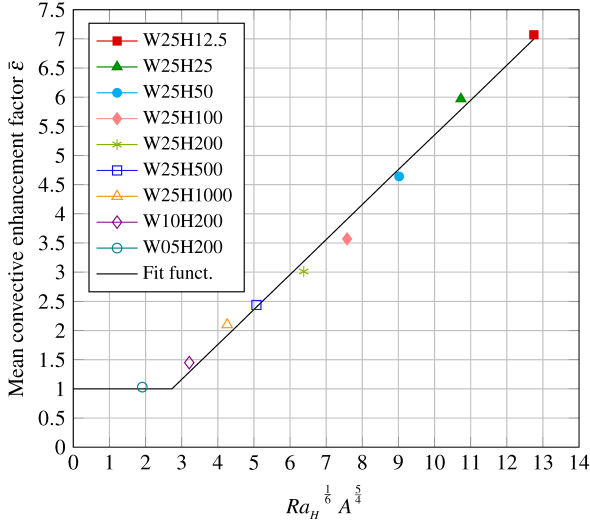


Figure 4.6: Mean convective enhancement factor plotted over the relevant dimensionless groups for all test cases.

The value $\bar{\epsilon} = 1$ is reached by the linear fit at a value of $Ra_H^{1/6} A^{5/4} = 2.73$, which leads to the following criterion for the occurrence of natural convection:

$$Ra_H^{1/6} A^{5/4} \geq 2.73 \quad (4.2)$$

With this, the linear fit is completely described by the function

$$\bar{\epsilon} = \begin{cases} 1, & Ra_H^{1/6} A^{5/4} < 2.73 \\ 0.57Ra_H^{1/6} A^{5/4} - 0.38, & Ra_H^{1/6} A^{5/4} \geq 2.73. \end{cases} \quad (4.3)$$

This function predicts both the occurrence and strength of natural convection during the melting process while charging a flat plate LHS.

However, natural convection will not affect the melting process from the beginning, but rather start at a distinct point. This is defined as the critical liquid phase fraction $f_{l,crit}$. An expression for the onset of natural convection was given by Equation 2.2,

$$\frac{Ra_{Hl}}{A_1^4} \geq 500, \quad (4.4)$$

where the index l is introduced to indicate that this equation is applied to a liquid region that gradually changes during the melting process. From this equation, a critical liquid phase fraction for the onset of natural convection while melting may be approximately derived: a rectangular region with the full height of the enclosure is assumed for the liquid region, $H_l = H$, as it would be the case in the melting process with only heat conduction. The width of the liquid is then the product of the enclosure width and the liquid phase fraction $W_l = f_l W$. With this assumption, the relation in Equation 4.4 is expressed in terms of the enclosure dimensions and rearranged to obtain the critical liquid phase fraction:

$$f_{l,crit} = A \sqrt[4]{\frac{500}{Ra_H}}. \quad (4.5)$$

Because of the assumption on the shape of the liquid region and the fact that Equation 4.5 is based on the correlation by Batchelor [35], which was actually derived from an experiment of an air cavity between a heated and a cooled plate, the validity for the present case may be limited. However, a similar equation can be derived from the simulation data obtained in this study.

The critical liquid phase fraction can be obtained from the convective enhancement factor ε , see Figure 4.5: The critical value is defined at that liquid phase fraction, where the convective enhancement factor ε first exceeds an arbitrarily defined value of 1.15. The resulting critical liquid phase fraction for all test cases is plotted in Figure 4.7 with logarithmic axes.

By adjusting the constant in Equation 4.5, a linear fit function,

$$f_{l,crit} = A \sqrt[4]{\frac{150}{Ra_H}}. \quad (4.6)$$

is found to fit the data well. This function for the critical liquid phase fraction is also plotted in Figure 4.7.

With the presented analysis, the influence of natural convection during charging can be predicted and included in the design process of a flat plate LHS: The occurrence and heat transfer enhancement of natural convection is characterized by the mean convective enhancement factor in Equation 4.3. For those cases, where natural convection occurs, the critical liquid phase fraction for the onset of natural convection during the melting process is given by Equation 4.6.

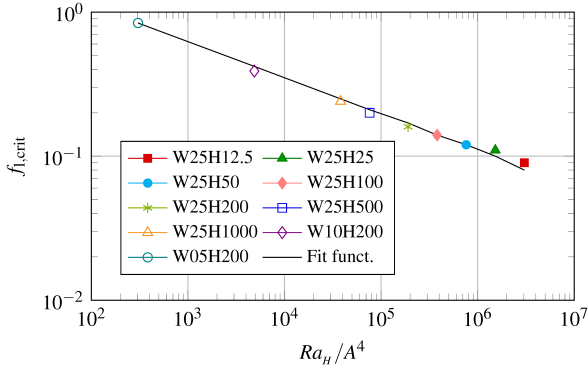


Figure 4.7: Critical liquid phase fractions for the onset of natural convection plotted over the fraction of Ra_H and A^4 for all test cases.

4.3 Experimental parameter study on driving temperature differences

In this section, the parameter study is extended by analyzing the three experiments with driving temperature differences $\Delta T = 5\text{ K}, 10\text{ K}$ and 20 K shown in Figure 2.12. The dimensionless numbers $Fo_H(t)$, Ste , Ra_H and A given in Table 2.3 were used. The exponents of $Fo_H(t)$, Ra_H and A were retained from the previous section, but additionally the Ste number was used to scale the influence of varying driving temperature difference. An optimization of the exponent of Ste revealed that the best results are obtained with an exponent of 1. An additional scaling constant with a value of 0.78 set the maximum of the scaled time to 1. The resulting scaled time is:

$$\tilde{t} = 0.78 Fo_H(t) Ste Ra_H^{\frac{1}{6}} A^{\frac{5}{4}}. \quad (4.7)$$

The next aim was to find a function that fits the data of liquid phase fraction over scaled time. The error function in the form $b_1 \cdot \text{erf}(b_2 \cdot \tilde{t})$ has proven to be suitable and it was adjusted to fit the scaled liquid phase fraction curves. A regression analysis was performed and an optimum was found that minimized the sum of all least square residuals to a value of 0.06 with parameters $b_1 = 1.04$ and $b_2 = 1.57 \approx \pi/2$. This led to a curve-fit function for the liquid phase

fraction over scaled time \tilde{t} :

$$f_1(\tilde{t}) = 1.04 \cdot \operatorname{erf}\left(\frac{\pi}{2} \cdot \tilde{t}\right). \quad (4.8)$$

The three liquid phase fraction curves over scaled time \tilde{t} and the curve-fit function Equation 4.8 are plotted in Figure 4.8. The liquid phase fraction curves coincide due to the scaling and the curve-fit represents the data well.

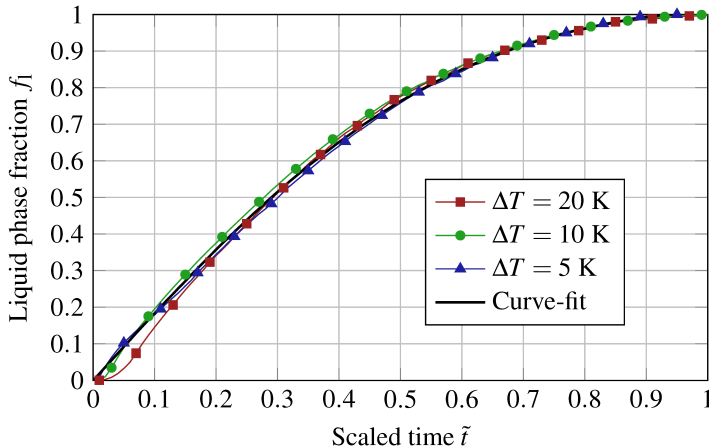


Figure 4.8: Liquid phase fractions of three different experimental test runs with varying temperature difference ΔT and the least squares curve-fit correlation from Equation 4.8 plotted over scaled time \tilde{t} .

In the previous section, a scaling for various enclosure dimensions was done. In this section, the analysis was extended to different driving temperature differences. Combining the two studies, the presented scaling Equation 4.7 and the curve-fit correlation Equation 4.8 span a large parameter range including enclosure heights $H = 25$ mm to 1000 mm, enclosure half widths $W = 5$ mm to 25 mm, aspect ratios $A = 0.5$ to 40 and driving temperature differences $\Delta T = 5$ K to 20 K. A restriction of this correlation is, however, the convection regime bounded by Equation 4.4. The validity might also be limited to the laminar regime bounded by Equation 2.3.

4.4 Conclusions

A numerical parameter study was performed to determine the influence of enclosure dimensions on melting with natural convection. Nine different test cases with various widths and heights were analyzed. The study included a large range of aspect ratios and Rayleigh numbers. With dimensional analysis, the results were scaled by the relevant dimensionless groups.

The influence of natural convection on the heat transfer rate was assessed with the introduced convective enhancement factor, which is defined as the ratio of actual heat flux to a hypothetical heat flux by heat conduction. Evaluated for the parameter study, it clearly indicates the impact of enclosure dimensions on melting with natural convection. By curve-fitting, a correlation function for the mean convective enhancement factor and the critical liquid phase fraction for the onset of natural convection were found.

The parameter study and the scaling analysis were extended by analyzing experimental test runs with different driving temperature differences. A correlation function for the liquid phase fraction in dimensionless form was found by curve-fitting. The presented scaling and the curve-fit correlation span a large parameter range including enclosure heights $H = 25$ mm to 1000 mm, enclosure half widths $W = 5$ mm to 25 mm, aspect ratios $A = 0.5$ to 40 and driving temperature differences $\Delta T = 5$ K to 20 K. This correlation can be used to predict similar melting processes in the given parameter range.

The presented results enable the design of a flat plate LHTES considering the effect of natural convection without exhaustive, expensive and time-consuming numerical analyses. Hence, the design process of these systems is facilitated. A specific result is that heat transfer enhancement due to natural convection increases with a smaller aspect ratio of storage material enclosures. Hence, the vertical segmentation of tall enclosures into smaller ones should be considered to enhance heat transfer during charging.

Chapter 5

Summary and outlook

In this last chapter, the content and results of this thesis are first summarized and then an outlook is given on research topics that have already been started or that may be a reasonable extension to this work in the future.

5.1 Summary

The general aims of this thesis were to validate numerical models for melting governed by natural convection and to find the influence of natural convection on the melting process in LHS systems using numerical and experimental data.

A novel experimental test bench was developed specifically for the validation of numerical models. A low-temperature material n-octadecane was used for accurate measurements with low thermal boundary effects. The PCM was contained in a rectangular enclosure heated by two opposite vertical sides with transparent front, back and top windows to allow access to optical measurement techniques. The phase state was measured with a shadowgraph technique and the velocities in the liquid phase due to natural convection were measured with a PIV technique. These optical measurement techniques allowed a high spatial resolution of data. Temperatures were recorded at distinct positions with thermocouples. Three different driving temperature differences between the heated plates and the melting temperature at the phase front were tested to obtain data with a range of Stefan and Rayleigh numbers for later parameter analysis. The experiments were repeated four times and an analysis of systematic and statistical errors was performed. All the data was measured at least every minute over the three hour lasting melting process to obtain transient data. The result is a

highly resolved data set of the phase state and flow during the melting process that enables thorough validation analyses.

In the next step, two different numerical models for solid-liquid phase change with natural convection were developed with the software ANSYS Fluent: the first one was a detailed model with variable material properties using the VOF method to allow volume expansion in an air layer on top of the PCM. The second one was a simplified model with constant material properties using the Boussinesq approximation to include buoyancy. A comparison of the two models simulating the ideal test case of the validation experiment showed that there are differences in the melting process at closer look, but that there were only marginal differences in the resulting liquid phase fractions and heat transfer rates. In conclusion, the simplified model with constant material properties and Boussinesq approximation is accurate enough to simulate such a melting process. This model was then used to simulate the validation experiment with a 3D domain including flow and thermal boundary effects. A detailed comparison to the experiment showed that the flow is qualitatively similar, but deviations were found in the velocity extrema. Horizontal flow velocities were 60 % larger in the simulation compared to the experiment. Vertical flow velocities were also 20 % larger in the simulations. The most deviations were in the upward flow boundary layer at the heated plates while the downward flow boundary layer at the solid phase showed a much better agreement. The liquid phase fractions agreed to 4 % and temperatures agreed to 2.8 % in the worst case. Consequently, the simulation model reproduces the validation experiment and qualifies for further studies to analyze the impact of natural convection on melting in LHS systems.

Finally, the impact of natural convection on melting in rectangular enclosures was investigated. Firstly, a numerical parameter study on different enclosure dimensions was performed. The results were scaled with the Fourier and Rayleigh numbers and the aspect ratio to be presented in dimensionless form. The influence of natural convection on the heat transfer rate was assessed with the introduced convective enhancement factor, which was defined as the ratio of actual heat flux by natural convection to a hypothetical heat flux by conduction only. By curve-fitting, a correlation function for the mean convective enhancement factor and the critical liquid phase fraction for natural convection onset were found. The study was extended with data from the validation experiment on different driving temperature differences and the Stefan number was included in the scaling to assess this effect. A correlation function for the liquid phase fraction in

dimensionless form was found by curve-fitting. The presented scaling and the curve-fit correlation span a large parameter range including enclosure heights $H = 25 \text{ mm}$ to 1000 mm , enclosure half widths $W = 5 \text{ mm}$ to 25 mm , aspect ratios $A = 0.5$ to 40 and driving temperature differences $\Delta T = 5 \text{ K}$ to 20 K . This correlation can be used to predict similar melting processes in the given parameter range. The presented results facilitate the design process of flat plate LHS systems by considering the effect of natural convection without exhaustive, expensive and time-consuming numerical analyses.

5.2 Outlook

As an outlook, four further research topics are presented that are related to this thesis. The first is about temperature measurements with higher resolution in validation experiments and the second is about high temperature experiments. The third topic is about using more efficient simulation methods that allow highly resolved 3D domains. The fourth research topic is the application of the findings of this thesis in storage system scale models, where the effect of natural convection is only approximated by an enhanced thermal conductivity model. The last topic is about detailed analyses on melting governed by natural convection, but in the more complex geometries of finned shell and tube systems.

5.2.1 Temperature measurement with high spatial resolution

The validation experiment developed in this thesis produced accurate benchmark results. The phase state and velocities in the liquid phase were measured with high temporal and spatial resolution. However, temperatures were only measured at three distinct points. A desired addition to the validation experiment would be the measurement of temperatures with high spatial resolution, i.e. the measurement of a 2D field of temperature. This would be possible with either thermochromic liquid crystals (TLCs) that have been already used to study natural convection [73] or with LED- or laser induced fluorescence (LIF), e.g. with thermographic phosphor particles [74]. Although these measurement techniques are quite sophisticated, they could be implemented in the same test bench, utilize the existing periphery for optical measurements and measured in conjunction with PIV.

5.2.2 High temperature experiments with nitrate salts

Although the test bench presented in this thesis was built for temperatures up to $T = 250\text{ }^{\circ}\text{C}$, only low-temperature experiments were performed with the organic material n-octadecane. The reasons were that heat losses are better controllable at lower temperatures, which led to more accurate results, and the handling of the PCM was easier and safer. However, in high temperature LHS mostly inorganic nitrate salts are used as storage materials. The temperature range of these materials is about $T_m = 120\text{ }^{\circ}\text{C}$ to $340\text{ }^{\circ}\text{C}$. To further investigate melting of these materials, high temperature experiments could be performed with the presented test bench.

5.2.3 Efficient simulation of highly resolved 3D domains

The ANSYS Fluent models used in this thesis delivered accurate results. However, the semi-implicit method (SIMPLE) used to solve the incompressible Navier-Stokes equations together with the enthalpy-porosity model for phase change proved to be inefficient. The equation system seemed to be stiff and the time steps were restricted to unusually small values. These findings lead to the idea of using more efficient algorithms. For rectangular geometries, structured meshes are much more efficient, because the resulting diagonal sparse linear equation systems are faster to solve. When the time steps are restricted by the stiffness of the problem, an explicit time stepping method may be another option to increase the efficiency and drastically decrease computation time or increase resolution.

During a research stay of this author at the University of Michigan, a highly efficient simulation code developed for magnetohydrodynamics by Zikanov et al. [75] and Krasnov et al. [76] could already be tested for phase change problems. The code uses an explicit second order time integration and second order spatial discretization on a structured mesh. Hence, an explicit version of the enthalpy porosity method [51] was implemented in the code. For verification, simulations of the 2D validation test case of Gau and Viskanta [25] were performed and compared to results by Hannoun and Alexiades [59] and to results from an ANSYS Fluent simulation. The method was found to be efficient and first results were promising. However, the implementation of the enthalpy porosity method needs further testing and validation.

5.2.4 Modeling of natural convection with enhanced thermal conductivity for large scale models

As the modeling of natural convection dominated melting requires significant computational effort and is not feasible for the scale of a whole storage system, simplified models for the effect of natural convection are advised for the design of LHS systems. A first step are the analytical correlation functions presented in this thesis that can be used to estimate similar processes. However, to simulate e.g. a flat plate latent heat storage system with its 2D or 3D domain and detailed boundary conditions, the solution of discretized partial differential equations is inevitable. But, with a sophisticated enhanced thermal conductivity model in the energy equation, the Navier-Stokes equations may not have to be solved.

Over the last years, the author of this thesis developed a simulation software in MATLAB named FASTER - Fast and Adjustable Simulation of Thermal Energy storage. The energy equation was implemented with a linearized source term enthalpy method for phase change, very similar as in the ANSYS Fluent model described in this thesis. The discretization was done in 1D, 2D or 3D on structured rectangular or cylindrical grids. The resulting diagonal sparse linear equation system is solved orders of magnitude faster than the non-diagonal equation systems resulting from unstructured meshes in ANSYS Fluent. Flow equations are not solved, but natural convection can be accounted for with a basic enhanced thermal conductivity (ETC) model. The FASTER software with ETC model has been used to simulate the flat plate latent heat storage illustrated in Figure 1.1. The domain for a discharging simulation with the FASTER ETC model is illustrated in Figure 5.1. Results of an early version of this model have already been verified with other similar models and validated with experimental data [20] in the work by Pointner et al. [58].

A verification study of the FASTER ETC model to results from the ANSYS Fluent CFD model by Vogel et al. [21] is shown in Figure 5.2, where the heat flow rate, the liquid phase fraction and the temperatures at three positions in the storage are compared. The ETC model worked well in the solidification case, where natural convection played a minor role. While the Fluent CFD model needed 6 d to simulate the process, the FASTER ETC model only needed 15 min on the same computer. The melting process could probably be simulated similarly. However, to achieve sufficient accuracy in the presence of strong natural convection, thermal stratification would have to be modeled with a height variation function for

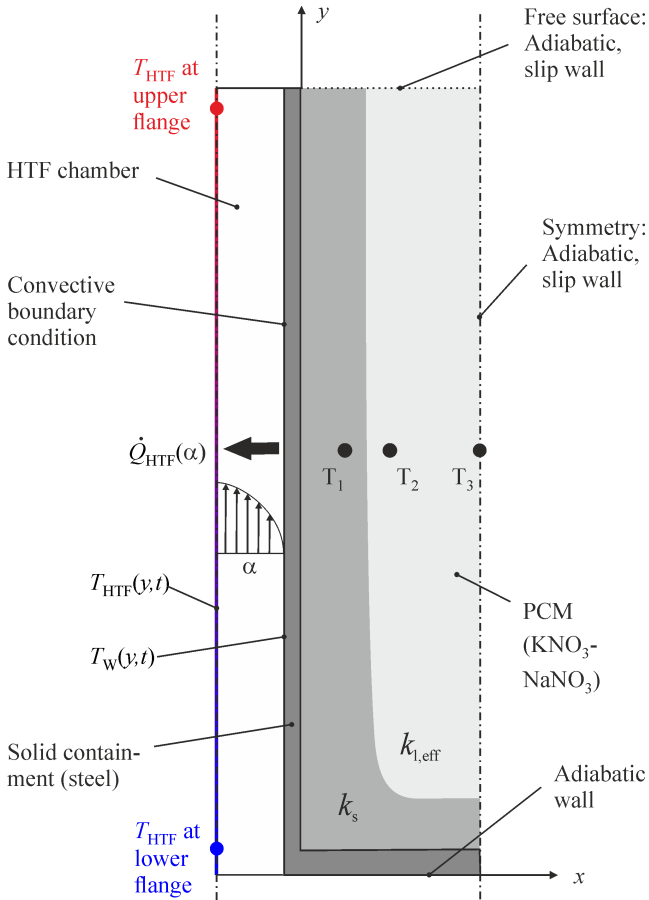


Figure 5.1: 2D simulation domain of discharging a flat plate LHS [21] including natural convection with the FASTER ETC model. The axis scales are not representative of the real storage system.

the enhanced thermal conductivity. Such a function was proposed by Benard et al. [24]. A similar function has already been implemented in FASTER and, while first tests have been promising, further improvements and validation tests are still needed. Another even more promising model by Vidalain et al. [77] could also be tried in the future. For validation of these models, the benchmark results presented in this thesis are predestined.

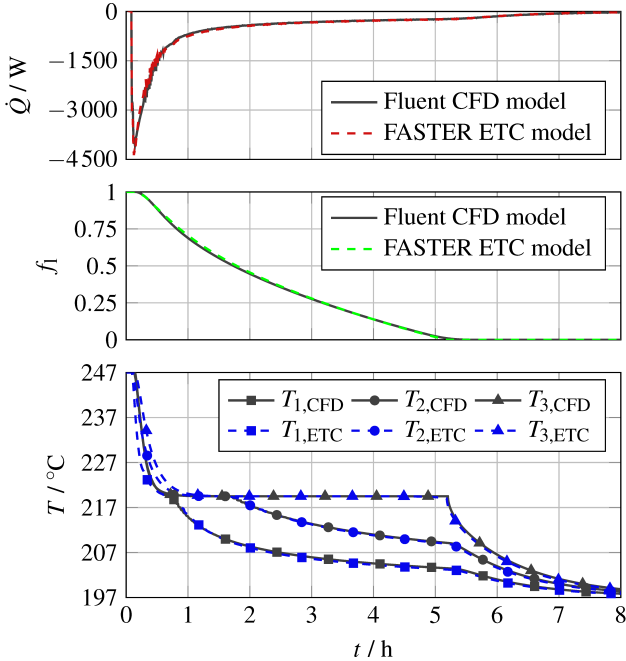


Figure 5.2: Comparison of the heat flow rate, the liquid phase fraction and the temperatures at three positions for simulations with the FASTER ETC and the Fluent CFD model.

5.2.5 Melting in finned shell and tube systems

In this thesis, the generic test case of a rectangular enclosure was regarded. This allowed very detailed experimental measurements and numerical simulation studies. However, LHS systems are usually built with heat exchangers, e.g.

aluminium fins, to increase the heat transfer between the HTF and the PCM, as for example in the work by Johnson et al. [7]. An example is the shell and tube system with axially extruded fins mounted on the tubes. For such a system, the same numerical models as described in this thesis can be used, only the simulation domain is more complicated. Due to its simplicity, better efficiency and sufficient accuracy, the Boussinesq model with constant material properties is recommended over the VOF model with variable properties. As shown in this thesis, the differences are negligible, when we are only interested in the heat transfer or melting rate.

For the design of a storage system during the TESIN project [8], various simulations on melting and solidification of PCMs in heat exchangers for shell and tube latent heat storage systems were performed. Most of these simulations were done with a heat conduction model to find the discharging characteristics for the design process. However, the author of this thesis also investigated melting governed by natural convection in 3D domains with small heights. A glimpse is given here: the simulation of a narrow section with height $H = 100$ mm of a shell and tube system with axially extruded fins is illustrated in Figure 5.3. The fin design was developed by Hübner et al. during the DSG-Store project [12]. Symmetries allow to discretize only a sixth of the shell and tube arrangement. The tube and fin are depicted in dark gray, the solid phase is shown in light gray, the liquid phase is transparently colored by temperature and flow velocities are visualized with black arrows. Strong flow currents are observed in the large gaps between the fin branches that clearly indicate melting governed by natural convection. Detailed evaluations of different fin geometries are planned in order to find the influence of natural convection on the melting process in finned shell and tube systems. The results will be submitted for publication, as soon as everything is finished.

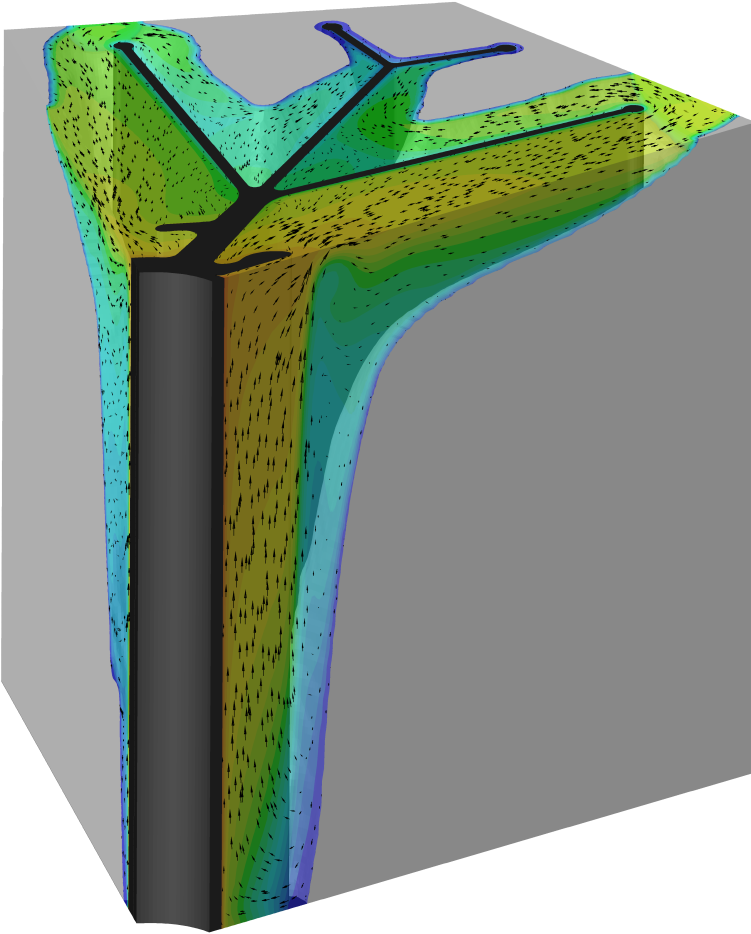


Figure 5.3: 3D Simulation of melting governed by natural convection in a section of a finned shell and tube geometry.

References

- [1] IPCC. *Climate Change 2014: Synthesis Report. Contribution of Working Groups I, II and III to the Fifth Assessment Report of the Intergovernmental Panel on Climate Change* [Core Writing Team, R.K. Pachauri and L.A. Meyer (eds.)] Geneva, Switzerland, 2014, pp. 1–151.
- [2] International Energy Agency (IEA). *Technology Roadmap: Energy storage*. Tech. rep. International Energy Agency, 2014.
- [3] Mehling, H. and Cabeza, L. F. *Heat and cold storage with PCM*. Berlin Heidelberg: Springer, 2008. DOI: 10.1007/978-3-540-68557-9.
- [4] Bauer, T., Steinmann, W.-D., Laing, D., and Tamme, R. “Thermal Energy Storage Materials and Systems”. In: *Annual Review of Heat Transfer*. 2012, pp. 131–177. DOI: 10.1615/AnnualRevHeatTransfer.2012004651.
- [5] Jegadheeswaran, S., Pohekar, S. D., and Kousksou, T. “Exergy based performance evaluation of latent heat thermal storage system: A review”. In: *Renewable and Sustainable Energy Reviews* 14.9 (2010), pp. 2580–2595. DOI: 10.1016/j.rser.2010.07.051.
- [6] Laing, D., Bahl, C., Bauer, T., Lehmann, D., and Steinmann, W. D. “Thermal energy storage for direct steam generation”. In: *Solar Energy* 85.4 (Apr. 2011), pp. 627–633. DOI: 10.1016/j.solener.2010.08.015.
- [7] Johnson, M., Vogel, J., Hempel, M., Dengel, A., Seitz, M., and Hachmann, B. “High temperature latent heat thermal energy storage integration in a co-gen plant”. In: *Energy Procedia* 73 (2015), pp. 281–288. DOI: 10.1016/j.egypro.2015.07.689.
- [8] Johnson, M., Vogel, J., Hempel, M., Hachmann, B., and Dengel, A. J. “Design of High Temperature Thermal Energy Storage for High Power Levels”. In: *Sustainable Cities and Society* 35 (2017), pp. 758–763. DOI: 10.1016/j.scs.2017.09.007.

REFERENCES

- [9] Thess, A. "Thermodynamic efficiency of pumped heat electricity storage". In: *Physical Review Letters* 111.11 (2013), pp. 1–5. DOI: 10.1103/PhysRevLett.111.110602.
- [10] Steinmann, W. D. "The CHEST (Compressed Heat Energy Storage) concept for facility scale thermo mechanical energy storage". In: *Energy* 69 (2014), pp. 543–552. DOI: 10.1016/j.energy.2014.03.049.
- [11] Laing, D., Bauer, T., Breidenbach, N., Hachmann, B., and Johnson, M. "Development of high temperature phase-change-material storages". In: *Applied Energy* 109 (2013), pp. 497–504. DOI: 10.1016/j.apenergy.2012.11.063.
- [12] Hübner, S., Eck, M., Stiller, C., and Seitz, M. "Techno-economic heat transfer optimization of large scale latent heat energy storage systems in solar thermal power plants". In: *Applied Thermal Engineering* 98 (Apr. 2016), pp. 483–491. DOI: 10.1016/j.applthermaleng.2015.11.026.
- [13] Samarskii, A. A., Vabishchevich, P. N., Iliev, O. P., and Churbanov, A. G. "Numerical simulation of convection/diffusion phase change problems—a review". In: *International Journal of Heat and Mass Transfer* 36.17 (1993), pp. 4095–4106. DOI: 10.1016/0017-9310(93)90071-D.
- [14] Hu, H. and Argyropoulos, S. a. "Mathematical modelling of solidification and melting: a review". In: *Modelling and Simulation in Materials Science and Engineering* 4.4 (1996), pp. 371–396. DOI: 10.1088/0965-0393/4/4/004.
- [15] Voller, V. "An Overview of Numerical Methods for Solving Phase Change Problems". In: *Advances in NUMERICAL HEAT TRANSFER: Volume 1*. Ed. by Minkowycz, W. and Sparrow, E. M. Taylor & Francis, 1997. Chap. 9, pp. 341–380.
- [16] Dutil, Y., Rousse, D. R., Salah, N. B., Lassue, S., and Zalewski, L. "A review on phase-change materials: Mathematical modeling and simulations". In: *Renewable and Sustainable Energy Reviews* 15.1 (2011), pp. 112–130. DOI: 10.1016/j.rser.2010.06.011.
- [17] Dhaidan, N. S. and Khodadadi, J. M. "Melting and convection of phase change materials in different shape containers: A review". In: *Renewable and Sustainable Energy Reviews* 43 (2015), pp. 449–477. DOI: 10.1016/j.rser.2014.11.017.

- [18] Kadri, S., Dhifaoui, B., Dutil, Y., Jabrallah, S. B., and Rousse, D. R. "Large-Scale Experimental Study of a Phase Change Material: Shape Identification for the Solid-Liquid Interface". In: *International Journal of Thermophysics* 36.10-11 (2015), pp. 2897–2915. DOI: 10.1007/s10765-015-1935-y.
- [19] Jany, P. and Bejan, A. "Scaling theory of melting with natural convection in an enclosure". In: *International Journal of Heat and Mass Transfer* 31.6 (June 1988), pp. 1221–1235. DOI: 10.1016/0017-9310(88)90065-8.
- [20] Johnson, M., Fiss, M., Klemm, T., and Eck, M. "Test and analysis of a flat plate latent heat storage design". In: *Energy Procedia*. Vol. 57. Elsevier B.V., 2013, pp. 662–671. DOI: 10.1016/j.egypro.2014.10.221.
- [21] Vogel, J., Felbinger, J., and Johnson, M. "Natural convection in high temperature flat plate latent heat thermal energy storage systems". In: *Applied Energy* 184 (2016), pp. 184–196. DOI: 10.1016/j.apenergy.2016.10.001.
- [22] Szekely, J. and Chhabra, P. S. "The effect of natural convection on the shape and movement of the melt-solid interface in the controlled solidification of lead". In: *Metallurgical and Materials Transactions* 1.5 (1970), pp. 1195–1203. DOI: 10.1007/BF02900231.
- [23] Hale, N. and Viskanta, R. "Photographic observation of the solid-liquid interface motion during melting of a solid heated from an isothermal vertical wall". In: *Letters in Heat and Mass Transfer* 5 (1978), pp. 329–337.
- [24] Benard, C., Gobin, D., and Martinez, F. "Melting in rectangular enclosures: experiments and numerical simulations". In: *Journal of heat transfer* 107 (1985). DOI: 10.1115/1.3247506.
- [25] Gau, C. and Viskanta, R. "Melting and Solidification of a Pure Metal on a Vertical Wall". In: *Journal of Heat Transfer* 108.1 (1986), p. 174. DOI: 10.1115/1.3246884.
- [26] Benard, C., Gobin, D., and Zanoli, A. "Moving boundary problem: heat conduction in the solid phase of a phase-change material during melting driven by natural convection in the liquid". In: *International Journal of Heat and Mass Transfer* 29.11 (1986), pp. 1669–1681. DOI: 10.1016/0017-9310(86)90108-0.
- [27] Wolff, F. and Viskanta, R. "Melting of a Pure Metal From a Vertical Wall". In: *Experimental Heat Transfer* 1.1 (1987), pp. 17–30. DOI: 10.1080/08916158708946328.

REFERENCES

- [28] Campbell, T. A. and Koster, J. N. "Visualization of liquid-solid interface morphologies in gallium subject to natural convection". In: *Journal of Crystal Growth* 140.3-4 (1994), pp. 414–425. DOI: 10.1016/0022-0248(94)90318-2.
- [29] Ben-David, O., Levy, A., Mikhailovich, B., and Azulay, A. "3D numerical and experimental study of gallium melting in a rectangular container". In: *International Journal of Heat and Mass Transfer* 67 (Dec. 2013), pp. 260–271. DOI: 10.1016/j.ijheatmasstransfer.2013.07.058.
- [30] Rösler, F. "Modellierung und Simulation der Phasenwechselvorgänge in makroverkapselten latenten thermischen Speichern". PhD thesis. Universität Bayreuth, 2014.
- [31] Bareiss, M. and Beer, H. "Experimental investigation of melting heat transfer with regard to different geometric arrangements". In: *International communications in heat and mass transfer* 11 (1984), pp. 323–333. DOI: 10.1016/0735-1933(84)90060-5.
- [32] Shokouhmand, H. and Kamkari, B. "Experimental investigation on melting heat transfer characteristics of lauric acid in a rectangular thermal storage unit". In: *Experimental Thermal and Fluid Science* 50 (Oct. 2013), pp. 201–212. DOI: 10.1016/j.expthermflusci.2013.06.010.
- [33] Van Buren, P. and Viskanta, R. "Interferometric measurement of heat transfer during melting from a vertical surface". In: *International Journal of Heat and Mass Transfer* 23 (1980), pp. 568–571.
- [34] Medrano, M., Yilmaz, M. O., Nogués, M., Martorell, I., Roca, J., and Cabeza, L. F. "Experimental evaluation of commercial heat exchangers for use as PCM thermal storage systems". In: *Applied Energy* 86.10 (2009), pp. 2047–2055. DOI: 10.1016/j.apenergy.2009.01.014.
- [35] Batchelor, G. K. "Heat transfer by free convection across a closed cavity between vertical boundaries at different temperatures". In: *Quarterly of Applied Mathematics* 12.3 (1954), pp. 209–233.
- [36] Elder, J. W. "Laminar free convection in a vertical slot". In: *Journal of Fluid Mechanics* 23 (1965), p. 77. DOI: 10.1017/S0022112065001246.

- [37] Galione, P., Lehmkuhl, O., Rigola, J., and Oliva, A. "Fixed-grid numerical modeling of melting and solidification using variable thermo-physical properties – Application to the melting of n-Octadecane inside a spherical capsule". In: *International Journal of Heat and Mass Transfer* 86 (2015), pp. 721–743. DOI: 10.1016/j.ijheatmasstransfer.2015.03.033.
- [38] Jasper, J. J. "The Surface Tension of Pure Liquid Compounds". In: *Journal of Physical and Chemical Reference Data* 1.4 (1972), pp. 841–1010. DOI: 10.1063/1.3253106.
- [39] Raffel, M., Willert, C. E., Wereley, S., and Kompenhans, J. *Particle Image Velocimetry: A Practical Guide*. Springer-Verlag Berlin Heidelberg, 2007, p. 448. DOI: 10.1007/978-3-540-72308-0.
- [40] Adrian, R. and Westerweel, J. *Particle Image Velocimetry*. Cambridge University Press, 2011.
- [41] *VDI Heat Atlas (VDI Wärmeatlas)*. Berlin, Heidelberg: Springer Vieweg, 2013. DOI: 10.1007/978-3-642-19981-3.
- [42] Voller, V. R., Cross, M., and Markatos, N. C. "An enthalpy method for convection/diffusion phase change". In: *International Journal for Numerical Methods in Engineering* 24.1 (1987), pp. 271–284. DOI: 10.1002/nme.1620240119.
- [43] Salcudean, M. and Abdullah, Z. "On the Numerical Modelling of Heat Transfer during Solidification Processes". In: *International journal for numerical methods in engineering* 25.June 1987 (1988), pp. 445–473.
- [44] Lacroix, M. and Voller, V. R. "Finite Difference solutions of solidification phase change problems: transformed versus fixed grids". In: *Numerical Heat Transfer, Part B: Fundamentals: An International Journal of Computation and Methodology* 17.1 (1990), pp. 25–41. DOI: 10.1080/10407799008961731.
- [45] Viswanath, R. and Jaluria, Y. "A comparison of different solution methodologies for melting and solidification problems in enclosures". In: *Numerical Heat Transfer, Part B Fundamentals* 24 (1993), pp. 77–105. DOI: 10.1080/10407799308955883.

REFERENCES

- [46] Voller, V. and Prakash, C. "A fixed grid numerical modelling methodology for convection-diffusion mushy region phase-change problems". In: *International Journal of Heat and Mass Transfer* 30.8 (1987), pp. 1709–1719. DOI: 10.1016/0017-9310(87)90317-6.
- [47] Brent, A. D., Voller, V. R., and Reid, K. J. "Enthalpy-Porosity Technique for Modeling Convection-Diffusion Phase Change: Application to the Melting of a Pure Metal". In: *Numerical Heat Transfer: An International Journal of Computation and Methodology* 13.3 (1988), pp. 297–318. DOI: 10.1080/10407788808913615.
- [48] Voller, V. R. and Swaminathan, C. R. "General Source-Based Method for Solidification Phase Change". In: *Numerical Heat Transfer, Part B: Fundamentals: An International Journal of Computation and Methodology* 19.2 (1991), pp. 175–189. DOI: 10.1080/10407799108944962.
- [49] Patankar, S. V. and Spalding, D. B. "A calculation procedure for heat, mass and momentum transfer in three-dimensional parabolic flows". In: *Int. J. Heat Mass Transfer* 15 (1972), pp. 1787–1806.
- [50] Chorin, A. J. "Numerical solution of the Navier-Stokes equations". In: *Mathematics of computation* 22.104 (1968), pp. 745–762. DOI: 10.2307/2004575.
- [51] Galione, P., Lehmkuhl, O., Rigola, J., and Oliva, A. "Fixed-grid modeling of solid-liquid phase change in unstructured meshes using explicit time schemes". In: *Numerical Heat Transfer, Part B: Fundamentals* 65.1 (2014), pp. 27–52. DOI: 10.1080/10407790.2013.836399.
- [52] Kozak, Y. and Ziskind, G. "Novel enthalpy method for modeling of PCM melting accompanied by sinking of the solid phase". In: *International Journal of Heat and Mass Transfer* 112 (2017), pp. 568–586. DOI: 10.1016/j.ijheatmasstransfer.2017.04.088.
- [53] Hirt, C. and Nichols, B. "Volume of fluid (VOF) method for the dynamics of free boundaries". In: *Journal of Computational Physics* 39.1 (Jan. 1981), pp. 201–225. DOI: 10.1016/0021-9991(81)90145-5.
- [54] Shatikian, V., Ziskind, G., and Letan, R. "Numerical investigation of a PCM-based heat sink with internal fins". In: *International Journal of Heat and Mass Transfer* 48.17 (Aug. 2005), pp. 3689–3706. DOI: 10.1016/j.ijheatmasstransfer.2004.10.042.

- [55] Shmueli, H., Ziskind, G., and Letan, R. "Melting in a vertical cylindrical tube: Numerical investigation and comparison with experiments". In: *International Journal of Heat and Mass Transfer* 53.19-20 (Sept. 2010), pp. 4082–4091. DOI: 10.1016/j.ijheatmasstransfer.2010.05.028.
- [56] Hosseinizadeh, S., Tan, F., and Moosania, S. "Experimental and numerical studies on performance of PCM-based heat sink with different configurations of internal fins". In: *Applied Thermal Engineering* 31.17-18 (Dec. 2011), pp. 3827–3838. DOI: 10.1016/j.applthermaleng.2011.07.031.
- [57] Farid, M. M. and Husian, R. M. "An electrical storage heater using the phase-change method of heat storage". In: *Energy Conversion and Management* 30.3 (1990), pp. 219–230. DOI: 10.1016/0196-8904(90)90003-H.
- [58] Pointner, H., de Gracia, A., Vogel, J., Tay, N., Liu, M., Johnson, M., and Cabeza, L. F. "Computational efficiency in numerical modeling of high temperature latent heat storage: Comparison of selected software tools based on experimental data". In: *Applied Energy* 161 (Jan. 2016), pp. 337–348.
- [59] Hannoun, N. and Alexiades, V. "Resolving the Controversy Over Tin and Gallium Melting in a Rectangular Cavity". In: *Numerical Heat Transfer, Part B: Fundamentals* 44.3 (2003), pp. 253–276. DOI: 10.1080/10407790390226974.
- [60] Bertrand, O. et al. "Melting driven by natural convection A comparison exercise: first results". In: *International Journal of Thermal Sciences* 38 (1999), pp. 5–26. DOI: 10.1016/S0035-3159(99)80013-0.
- [61] Gobin, D. and Quéré, P. L. "Melting from an isothermal vertical wall. Synthesis of a numerical comparison exercise". In: *Computer Assisted Methods in Engineering and Science* 7.3 (2000), pp. 289–288.
- [62] ANSYS Inc. *ANSYS 15 Fluent User's Guide*. 2015.
- [63] ANSYS Inc. *ANSYS 15 Fluent Theory Guide*. 2015.
- [64] Carman, P. "Fluid flow through granular beds". In: *Chemical Engineering Research and Design* 75 (1997), S32–S48. DOI: 10.1016/S0263-8762(97)80003-2.
- [65] Versteeg, H. K. and Malalasekera, W. *An introduction to computational fluid dynamics*. 2nd ed. Pearson Education, 2007.

REFERENCES

- [66] Okada, M. "Analysis of heat transfer during melting from a vertical wall". In: *International Journal of Heat and Mass Transfer* 27.11 (1984), pp. 2057–2066. DOI: 10.1016/0017-9310(84)90192-3.
- [67] Gadgil, A. and Gobin, D. "Analysis of Two-Dimensional Melting in Rectangular Enclosures in Presence of Convection". In: *Journal of Heat Transfer* 106.1 (1984), p. 20. DOI: 10.1115/1.3246636.
- [68] Wang, Y., Amiri, A., and Vafai, K. "An experimental investigation of the melting process in a rectangular enclosure". In: *International Journal of Heat and Mass Transfer* 42.19 (1999), pp. 3659–3672. DOI: 10.1016/S0017-9310(99)00024-1.
- [69] Shatikian, V., Ziskind, G., and Letan, R. "Numerical investigation of a PCM-based heat sink with internal fins: Constant heat flux". In: *International Journal of Heat and Mass Transfer* 51.5-6 (2008), pp. 1488–1493. DOI: 10.1016/j.ijheatmasstransfer.2007.11.036.
- [70] Ho, C., Liu, K., and Yan, W.-M. "Melting processes of phase change materials in an enclosure with a free-moving ceiling: An experimental and numerical study". In: *International Journal of Heat and Mass Transfer* 86 (2015), pp. 780–786. DOI: 10.1016/j.ijheatmasstransfer.2015.03.063.
- [71] Bauer, T., Laing, D., and Tamme, R. "Overview of PCMs for Concentrated Solar Power in the Temperature Range 200 to 350degC". In: *Advances in Science and Technology* 74 (Oct. 2010), pp. 272–277. DOI: 10.4028/www.scientific.net/AST.74.272.
- [72] Schinkel, W. M. M., Linthorst, S. J. M., and Hoogendoorn, C. J. "The Stratification in Natural Convection in Vertical Enclosures". In: *Journal of Heat Transfer* 105.2 (1983), p. 267. DOI: 10.1115/1.3245573.
- [73] Cuckovic-Dzodzo, D. "Laminar natural convection in a fully partitioned enclosure containing fluid with nonlinear thermophysical properties". In: *International Journal of Heat and Fluid Flow* 20 (1999), pp. 614–623. DOI: 10.1016/S0142-727X(99)00053-3.
- [74] Abram, C., Fond, B., Heyes, A. L., and Beyrau, F. "High-speed planar thermometry and velocimetry using thermographic phosphor particles". In: *Applied Physics B: Lasers and Optics* 111.2 (2013), pp. 155–160. DOI: 10.1007/s00340-013-5411-8.

- [75] Zikanov, O., Listratov, Y. I., and Sviridov, V. G. "Natural convection in horizontal pipe flow with a strong transverse magnetic field". In: *Journal of Fluid Mechanics* 720 (2013), pp. 486–516. DOI: 10.1017/jfm.2013.45.
- [76] Krasnov, D., Zikanov, O., and Boeck, T. "Comparative study of finite difference approaches in simulation of magnetohydrodynamic turbulence at low magnetic Reynolds number". In: *Computers and Fluids* 50.1 (2011), pp. 46–59. DOI: 10.1016/j.compfluid.2011.06.015.
- [77] Vidalain, G., Gosselin, L., and Lacroix, M. "An enhanced thermal conduction model for the prediction of convection dominated solid–liquid phase change". In: *International Journal of Heat and Mass Transfer* 52.7-8 (Mar. 2009), pp. 1753–1760. DOI: 10.1016/j.ijheatmasstransfer.2008.09.020.